Karlsruhe Institute of Technology

Instituto Tecnológico de Buenos Aires

Experimental investigation of air entrainment by a vertical jet plunging into a liquid pool

An der Fakultät für Maschinenbau des Karlsruher Instituts für Technologie eingereichte

Masterarbeit

zur Erlangung des akademischen Grades

Master of Science Maschinenbau

(M.Sc. Maschinenbau)

Vorgelegt von

Fabian Büttner

Betreut von:

Prof. Dr. Thomas Schulenberg
Dr. Stephan Gabriel
Dr. Dietmar Kuhn

Eidesstattliche Versicherung

Ich versichere, dass ich die vorliegende Arbeit selbständig und ohne Benutzung anderer als der angegebenen Hilfsmittel angefertigt habe. Alle Stellen, die wörtlich oder sinngemäß aus Veröffentlichungen oder anderen Quellen entnommen sind, sind als solche eindeutig kenntlich gemacht. Die Arbeit ist in gleicher oder ähnlicher Form noch nicht veröffentlicht und noch keiner Prüfungsbehörde vorgelegt worden.

Karlsruhe, den 28.05.2018

Abstract

“Experimental investigation of air entrainment by a vertical jet plunging into a liquid pool”

Two-phase flows that comprise a liquid and a gas appear in numerous applications of energy and process technology. The exact calculation of these flows by means of CFD-simulations poses problems until today. To cope with this problem, exact models that describe turbulence and phase interactions are required.

In the context of this work, extensive experiments were conducted by analysing a plunging jet. Such a jet carries ambient air towards the free surface and entrains – under given circumstances – a part of the gas under water. The obtained data poses a base for the validation of existing CFD-codes and for the development of new ones.
The aim of the work is the investigation of the liquid flow field that is induced by the jet inside the receiving pool and the simultaneous observation of the gaseous phase. The applied measurement techniques were Particle Image Velocimetry (PIV) for analysing the liquid flow field and shadowgraph imaging, which enables a study of the dispersed air bubbles. Furthermore, all boundary conditions that influence the experiment were recorded.

The experimental results that deal with the temporal behaviour show transient characteristics, concerning both the liquid flow field and entrained air bubbles. A time scale was found for which the time averaged flow field of the liquid phase can be claimed as statistical significant, as well as the amount of present air bubbles in the pool. Having repeated the experiment under identical boundary conditions, the reproducibility of the averaged liquid flow field could be proved. Although the total amount of detected bubbles in the comparative measurement exceeded the previous counts by multiples, both test series exhibit coinciding tendencies concerning the frequency of present bubble diameters.
The analysis of the averaged liquid flow field reveals a symmetry in radial direction around the jet axis. The computation of the spatial mean velocities and those of the velocity fluctuations give information about turbulence intensities, Reynolds-stresses and about the turbulent kinetic energy.
The investigation of the dispersed air bubbles indicates the bubble’s rising velocity in dependency of their diameter. An area was identified in which no descending bubbles were observed. On the symmetry axis of the jet, bubbles were found whose maximum magnitude of velocity exceed the local velocity of the averaged liquid flow field by far. Hence, the mean velocity field of the turbulent continuous phase is only limited usable to predict maximum magnitudes of bubble velocities.

Kurzfassung

„Experimentelle Untersuchung zur Blasenentstehung durch einen vertikalen, in ein Flüssigkeitsbad eintauchenden Freistrahl“

Zweiphasenströmungen aus einem Gas und einer Flüssigkeit treten in zahlreichen Anwendungen der Energie- und Verfahrenstechnik auf. Die exakte, prädiktive Berechnung dieser Strömungen mit CFD-Methoden stellt jedoch nach wie vor eine Herausforderung dar. Erforderlich sind valide Modelle für Turbulenz und Phasenwechselwirkung sowie entsprechende Schließungsgleichungen.

Als Basis für die Entwicklung neuer CFD-Modelle wurden im Rahmen der präsentierten Arbeit umfangreiche Experimente an einem in ein Becken eintauchenden Freistrahl durchgeführt. Solch ein Freistrahl führt Umgebungsluft in Richtung der freien Oberfläche und transportiert – unter gegebenen Bedingungen – einen Teil des Gases in das Wasser.
Ziel der vorliegenden Arbeit ist die Untersuchung des durch den Freistrahl induzierten Strömungsfeldes in der kontinuierlichen Flüssigphase simultan mit der Analyse der dispersen Gasphase. Als Messmethoden wurden dabei Particle Image Velocimetry (PIV) angewandt um das Strömungsfeld der flüssigen Phase zu analysieren, als auch das Verfahren des Shadowgraph Imaging, welches eine Beobachtung der dispers vorliegenden Luftblasen ermöglicht. Darüber hinaus wurden sämtliche Randbedingungen aufgezeichnet, welche Einfluss auf das Experiment haben.

Die Ergebnisse zum zeitlichen Verhalten des Versuchs zeigen eine transiente Charakteristik des induzierten flüssigen Strömungsfeldes, als auch ein stark unregelmäßiges Verhalten des Lufteinschlusses. Es konnte eine Zeitskala gefunden werden, in welcher das gemittelte Strömungsfeld der flüssigen Phase als statistisch signifikant zu bewerten ist, ebenso die Anzahl der im Becken vorhandenen Luftblasen. Durch ein wiederholtes Durchführen des Experiments bei gleichbleibenden Randbedingungen konnte die Reproduzierbarkeit des gemittelten flüssigen Strömungsfeldes sichergestellt werden. Obgleich die Anzahl der detektierten Blasen im Vergleichsexperiment um ein Vielfaches höher war, zeigen beide Messungen Übereinstimmung bezüglich der normierten Blasengrößenverteilung.
Die Analyse des gemittelten flüssigen Strömungsfeldes weist eine Symmetrie in radialer Richtung um die Achse des Freistrahls auf. Die Messung der mittleren Geschwindigkeit kombiniert mit der Messung der Geschwindigkeitsfluktuation gibt Aufschluss über den lokalen Turbulenzgrad, als auch über die Reynoldsspannungen und die turbulente kinetische Energie. Die Betrachtung der Luftblasen gibt Aufschluss über die Aufstiegsgeschwindigkeit in Abhängigkeit des Blasendurchmessers. Es wurde ein Bereich identifiziert, in welchem keine nach unten transportieren Blasen zu beobachten sind. Auf der Mittelachse des Freistrahls wurden maximale Blasengeschwindigkeiten beobachtet, welche die lokalen Geschwindigkeiten des gemittelten flüssigen Strömungsfeldes weit überschreiten. Somit stellt ein zeitliches Mittel des stark turbulenten Strömungsfeldes nur eine eingeschränkt nutzbare Möglichkeit dar, maximale Blasengeschwindigkeiten abzuschätzen.

Compendio

„Investigación experimental del transporte de aire por un chorro vertical incidente en un cuerpo de agua"

Los flujos bifásicos que comprenden un líquido y un gas aparecen en numerosas aplicaciones de procesos energéticos y químicos. El cálculo exacto de estos flujos por medio de simulaciones CFD representa problemas hasta el día de hoy. Para lidiar con este problema, se requieren modelos exactos que describan la turbulencia y las interacciones bifásicas.
En el marco de este trabajo, numerosos experimentos fueron realizados, en los cuales se analizó un chorro incidente en un cuerpo líquido. Este chorro lleva consigo aire del ambiente hacia la superficie sobre la cual incide, y -bajo ciertas condiciones- transporta parte de este aire dentro del agua. Los resultados de esta investigación sirven de base para el desarrollo de nuevos modelos CFD.

El objetivo de este trabajo es la descripción del campo de fluidos en el líquido, el cual es creado por el chorro, así como el análisis del gas. Como método de medición se usó el PIV (Particle Image Velocimetry) para el análisis del campo de velocidades en el líquido, y para observar el comportamiento de las burbujas de aire se usó el método de Shadowgraph Imaging. Adicionalmente se midieron distintos parametros externos que influyen los resultados del experimento.

Los resultados que describen el comportamiento temporal muestran fluctuaciones en el campo de velocidades del cuerpo líquido y en la cantidad de burbujas presentes. Se encontró una escala de tiempo, con la cual el campo de velocidades promedio es estadísticamente significativo, así como el número de burbujas captadas. A través de la repetición del experimento con las mismas condiciones de contorno pudo garantizarse la repetibilidad del campo de fluido medio. A pesar de que la cantidad de burbujas detectadas en el experimento de comparación era mucho mayor, ambas mediciones coinciden con la distribución porcentual del diámetro de las burbujas.
El análisis del campo de velocidades medio del agua muestra una simetría en la dirección radial. La medición de la velocidad media así como la medición de las fluctuaciones de la velocidad proveen información sobre el nivel de turbulencia local, al igual que sobre las tensiones de Reynolds y la energía cinética turbulenta. La observación de las burbujas permite conocer la velocidad de ascenso en función del diámetro. Se identificó un área, en el cual las burbujas no son transportadas hacia abajo. En el eje del chorro después de haber entrado en contacto con el agua se observaron velocidades de las burbujas, las cuales fueron mucho mayores que la velocidad local del chorro. Por este motivo, el promedio temporal del campo de fluido turbulento representa solamente una posibilidad limitada para estimar la velocidad máxima de las burbujas.

Table of contents

Nomenclature

Latin symbols

Symbol	*Description*	*Unit*
A	surface	m^2
$\boldsymbol{a}_i$	coefficients of estimated mapping function	$-$
B	mobility	$m/(Ns)$
c	speed of wave propagation	m/s
c_o	speed of light in vacuum	m/s
c_D	drag coefficient	$-$
cnt	count bubbles	$-$
D	detectability	$-$
d_B	diameter bubble	m
d_i	image distance	m
d_J	diameter jet	m
d_N	diameter nozzle	m
d_o	object distance	m
d_P	diameter particle	m
d_r	diameter reference point	m
E	energy	Nm
F	force	N
f	frequency	$1/s$
$\boldsymbol{F}(\boldsymbol{x})$	mapping function	$-$
F_B	buoyancy force	N
F_D	drag force	N
$\widehat{\boldsymbol{F}}(\boldsymbol{x})$	estimated mapping function	$-$
F_G	gravity force	N
F_n	form component of drag force	N
F_{Res}	resulting force	N
F_τ	friction component of drag force	N
Fr	Froude number	$-$
g	constant of gravity	m/s^2
H	distance of parallel plates	m
H_{FT}	water level feed tank	m
H_{RP}	water level receiving pool	m
i, j	indexes	$-$
$\boldsymbol{k}$	external impact on body	m/s^2
L	length	m
l_c	characteristic length	m
L_J	length jet	m
L_N	length nozzle	m

M	magnification constant	$-$
m_P	mass particle	kg
MA_N	moving average of N measurements	$-$
N	number of entities	$-$
n	refractive index	$-$
n_A	refractive index air	$-$
n_W	refractive index water	$-$
p	pressure	N/m^2
Q_L	volumetric flow rate liquid	l/s
r	radius	m
R	cross correlation value	$-$
Re	Reynolds number	$-$
s	strech	m
S	surface	m^2
S_N	standard deviation of N measurements	$-$
St	Stokes number	$-$
t	time	s
T	temperature	$°C$
Tu	turbulence intensity	$-$
U	velocity plate	m/s
U_0	velocity jet at impingement point	m/s
$\boldsymbol{u} = (u_x, u_y, u_z)$	fluid velocity vector	m/s
V	volume	m^3
v	velocity	m/s
v_c	characteristic velocity	m/s
v_J	velocity jet	m/s
v_N	velocity at nozzle outlet	m/s
v_T	terminal velocity	m/s
v_{TS}	terminal settling velocity	m/s
W	work	Nm
We	Weber-number	$-$
$\boldsymbol{x} = (x, y, z)$	cartesian coordinates on object plane	m
$\boldsymbol{X} = (X, Y, Z)$	cartesian coordinates on image plane	m

Greek symbols

Symbol	*Description*	*Unit*
γ	surface tension	N/m
ε	area-specific change of energy	N/m
θ_1	angle of incident light ray	°
θ_2	angle of emergent light ray	°
θ_c	critical angle	°

λ	wavelength light	m
μ	dynamic viscosity	$(Ns)/m^2$
μ_G	dynamic viscosity gas	$(Ns)/m^2$
μ_L	dynamic viscosity liquid	$(Ns)/m^2$
ν	kinematic viscosity	m^2/s
ρ	density	kg/m^3
ρ_F	density fluid	kg/m^3
ρ_G	density gas	kg/m^3
ρ_L	density liquid	kg/m^3
ρ_P	density particle	kg/m^3
τ_F	characteristic time scale flow	s
τ_P	response time particle	s
τ	shear stress	N/m^2
τ_R	Reynolds stress	N/m^2
ϕ	instantaneous quantity	$-$
$\bar{\phi}$	average of quantity	$-$
ϕ'	fluctuation of quantity	$-$
ϕ_{rms}	root-mean-square value of set of fluctuations	$-$

Abbreviations

Abbreviation	*Description*
CCD	Charged-Coupled-Device
CFD	Computational Fluid Dynamics
CMOS	Complementary-Metal-Oxide Semiconductor
IA	Interrogation Area
MA	Moving Average
Nd:YAG	Neodymium-doped Yttrium Aluminum Garnet
NSE	Navier-Stokes-Equation
PIV	Particle Image Velocimetry
PMMA	Polymethyl Methacrylate
PTV	Particle Tracking Velocimetry
RMS	Root Mean Square

1 Introduction

Flows that consist of a gas and a liquid are called two-phase flows. They appear in nature as well as in numerous technical applications. The interaction of the fluids and their often strongly differing properties create a complex flow situation which is challenging to describe mathematically in its entirety. Indeed, a prediction of the flow behaviour is of great interest to several fields of application, for example to the operation of geothermal power plants.
Transporting the geothermal water to the surface leads to a decreasing pressure of the liquid which causes a decreasing solubility of carbon dioxide. The result is a two-phase flow, in which the deposited carbon dioxide is present as gaseous bubbles. These bubbles are transported inside the tubes by the streaming water and by buoyancy; their presence has an influence on the liquid flow field on the one hand, and represents a risk for the proper operational reliability of the pump and other mechanical components on the other hand.

This work is written with the aim to acquire further knowledge about the phenomena that govern two-phase flows. Therefore, an experimental setup is installed that creates a liquid jet which impinges on a receiving pool that is filled with water. This plunging jet causes an entrainment of ambient air into the liquid pool.
Although the experimental scenario does not equal the exact application area of geothermal power plants, the experiment is rather a surrogate setup which enables the investigations of exact phenomena. By creating a plunging jet, a turbulent flow field is induced inside the receiving pool. The entrained air is present in the form of bubbles of different sizes. They are firstly transported downstream due to their momentum and rise to the surface again at another instant of time when the force of buoyancy is dominant. Thus, the generation of a plunging jet offers the opportunity to analyse and characterise not only the mechanisms of air entrainment, but also the interaction between the gaseous and liquid phase as well as the influence of the dispersed bubbles on the flow field and the other vice versa.

Appearing rather trivial at first glance, the mathematical description of the event of a plunging liquid jet exhibits very challenging problems. In the past, numerous scientists studied that particular phenomenon and its characteristics, but until now, it has not been understood in its entirety.

Besides the analysis of the flow fields, all the boundary conditions that have an influence on the experiment are recorded. In this manner, a set of data is created that poses a basis for model validation of CFD simulations and for generating new algorithms that are based on the results of this work, independent on the field of application.

The work is structured in the following way:

- The second chapter introduces elementary theories how to describe the dynamics of fluids mathematically. Based on the Navier-Stokes-Equations, the Reynolds-decomposition is presented in order to handle turbulent flows. In addition, for the purpose of being able to understand this work, subject-specific topics which concern jets and two-phase flows are explained.

- The third chapter deals with the fundamentals of the applied measurement techniques, which are Particle-Image-Velocimetry for investigating the continuous, liquid phase, and shadowgraph imaging that provides a possibility to observe the dispersed gaseous phase. The work describes the physics the techniques are based on and the methods that are used to obtain quantitative data.
- In chapter number four, the experimental setup is presented. This includes the construction that creates the plunging jet as well as the installed measurement equipment.
- In the fifth chapter, the measurement program is explained. It is divided into three parts: The first part gives an overview of the boundary conditions that are recorded in order to describe all variables that have an influence on the experiment. The second section describes the handling of the flow's temporal behaviour, the third one characterizes the evaluation of the averaged flow field.
- Chapter number six presents the results of those measurements
- The seventh chapter draws a conclusion of this work.
- In the appendix, detail drawings of the experimental construction are attached. In addition, a tabular listing of the experiment's boundary conditions and measuring results are presented.

2 Fundamentals of fluid dynamics

In 1687, Isaac Newton described the behaviour of solid bodies that are impacted by forces in his literary work “Principia”. The equations that concern the mechanics of solids had been extended and made applicable to fluids. The mathematicians and physicists Leonhard Euler and Daniel Bernoulli made some significant contributions by formulating their observations concerning fluid mechanics, but neither took friction into account.

“But there is a whole class of motions of which the common theory takes no cognizance whatever, namely, those which depend on the tangential action called into play by the sliding of one portion of a fluid along another, or of a fluid along the surface of a solid, or of a different fluid, that action in fact which performs the same part with fluids that friction does with solids” – G. G. Stokes [41].

These observations, made by George Gabriel Stokes and Claude Louis Marie Henri Navier in the first half of the 19th century, led to the Navier-Stokes equations (NSE). The equations, which form a system of nonlinear partial differential equations, describe the relation between a flow’s variables like pressure and velocity as a function of position and time [32], also taking the viscosity of the fluid into account. Equation *2.1* presents the NSE for incompressible, Newtonian fluids ($\mu \neq f(\tau)$) [33]:

$$\rho * \left(\frac{\partial u_i}{\partial t} + u_j * \frac{\partial u_i}{\partial x_j}\right) = k_i - \frac{\partial p}{\partial x_i} + \mu * \frac{\partial^2 u_i}{\partial {x_j}^2} \qquad 2.1$$

for i=1,2,3 and j=1,2,3. Subsequently, the velocity vector $\boldsymbol{u}$ of the fluid and the cartesian coordinates $\boldsymbol{x}$ are named as follows:

$$\boldsymbol{u} = \begin{pmatrix} u_1 \\ u_2 \\ u_3 \end{pmatrix} = \begin{pmatrix} u_x \\ u_y \\ u_z \end{pmatrix}$$

$$\boldsymbol{x} = \begin{pmatrix} x_1 \\ x_2 \\ x_3 \end{pmatrix} = \begin{pmatrix} x \\ y \\ z \end{pmatrix}$$

Inserting this convention into equation *2.1* yields the three-dimensional NSE:

$$\rho * \left(\frac{\partial u_x}{\partial t} + u_x * \frac{\partial u_x}{\partial x} + u_y * \frac{\partial u_x}{\partial y} + u_z * \frac{\partial u_x}{\partial z}\right) = k_x - \frac{\partial p}{\partial x} + \mu * \left(\frac{\partial^2 u_x}{\partial x^2} + \frac{\partial^2 u_x}{\partial y^2} + \frac{\partial^2 u_x}{\partial z^2}\right) \qquad 2.2$$

$$\rho * \left(\frac{\partial u_y}{\partial t} + u_x * \frac{\partial u_y}{\partial x} + u_y * \frac{\partial u_y}{\partial y} + u_z * \frac{\partial u_y}{\partial z}\right) = k_y - \frac{\partial p}{\partial y} + \mu * \left(\frac{\partial^2 u_y}{\partial x^2} + \frac{\partial^2 u_y}{\partial y^2} + \frac{\partial^2 u_y}{\partial z^2}\right) \qquad 2.3$$

$$\rho * \left(\frac{\partial u_z}{\partial t} + u_x * \frac{\partial u_z}{\partial x} + u_y * \frac{\partial u_z}{\partial y} + u_z * \frac{\partial u_z}{\partial z}\right) = k_z - \frac{\partial p}{\partial z} + \mu * \left(\frac{\partial^2 u_z}{\partial x^2} + \frac{\partial^2 u_z}{\partial y^2} + \frac{\partial^2 u_z}{\partial z^2}\right) \qquad 2.4$$

where p represents the pressure, ρ the density, μ the dynamic viscosity and k acting body forces, e.g. the force of gravity. Combined with the equation of continuity

$$\frac{\partial u_i}{\partial x_i} = 0 \qquad 2.5$$

and accordingly

$$\frac{\partial u_x}{\partial x} + \frac{\partial u_y}{\partial y} + \frac{\partial u_z}{\partial z} = 0 \qquad 2.6$$

the system is comprised of four differential equations (one NSE for each spatial direction plus the equation of continuity) and four unknown values (u_x, u_y, u_z, p).
In theory, the NSE are deterministic. Thus, combined with the boundary and initial conditions of the flow, the NSE provide a description of the present flow field as a function of time. But in fact, the analytical solution of the NSE is one of the most complex contemporary mathematical problems [12], that has until now only succeeded by making simplifying assumptions (e.g. neglecting inertia forces in the so-called *Stokes-Flow*).
The following paragraphs of this chapter describe mechanisms of fluid dynamics that are essential for understanding this work.

2.1 Turbulence

"*Generally speaking, turbulence can be expected in a fluid whenever there is a shearing flow and the inertial effects are much larger than viscous effects. The proper measure of this ratio is the "Reynolds Number". Furthermore, turbulence is always rotational; it can be described as a random field of vorticity." – S. Corrsin [7]*

To explain the definition of turbulence made by *S. Corrsin*, this paragraph gives an introduction into the phenomenon.
The NSE have been described as *deterministic.* In combination with boundary and initial conditions, the solution is (theoretically) known. Talking about turbulence, another criterion has to be mentioned that has an influence on the solution: stability. The exact solution of the system of differential equations is only possible when the boundary and initial conditions are known without any discrepancy, hence with an infinite accuracy. Of course, this is a mathematical ideal and not feasible in practice. In reality, the accuracy of the values is always finite. So, stability means that small disturbances in the boundary or initial conditions lead only to small variations of the solution [32]. Flows that comply with the requirement of stability are called *laminar flows.* Flows whose solution are susceptible to small variations in the initial or boundary conditions are described as *turbulent.*
So the difference between laminar and turbulent flows is their different behaviour concerning the presence of disturbances inside the flow. To judge if a flow remains stable under given circumstances or if disturbances will turn it into a turbulent, chaotic one, the use of the Reynolds number gives a possibility to make a rough estimate. Even though the stability of the flow is dependent on many influencing variables, *O. Reynolds* found that turbulence dies out for $Re < \sim 2000$ [12].
Although turbulence has not been understood in its entirety from both a physical and a mathematical view until today, there exist approved models and approaches that try to explain the phenomenon and handle it mathematically. However, due to the random nature of turbulence, a statistical approach is needed. Consequently, the instantaneous flow field cannot be represented thereby. But for most applications, statistical quantities such as average velocity and the standard deviation of the fluctuating flow variables are sufficient to characterize the flow.

An instantaneous quantity can be separated into an *average* plus a *fluctuation:*

$$\phi_i = \bar{\phi}_i + \phi_i' \qquad 2.7$$

where ϕ_i is the instantaneous quantity, $\bar{\phi}_i$ the average and ϕ_i' the fluctuation. As the data that is provided by measurements is not a continuous signal but an output at discrete, equi-spaced points, the mean value is not formed by integrating the signal over the time t, but by building the sum of all measurements and dividing it by the number of samples N [32]:

$$\bar{\phi}_i = \lim_{N\to\infty} \frac{1}{N}\sum_{i=1}^{N} \phi_i \qquad 2.8$$

Figure 2-1 illustrates the composition:

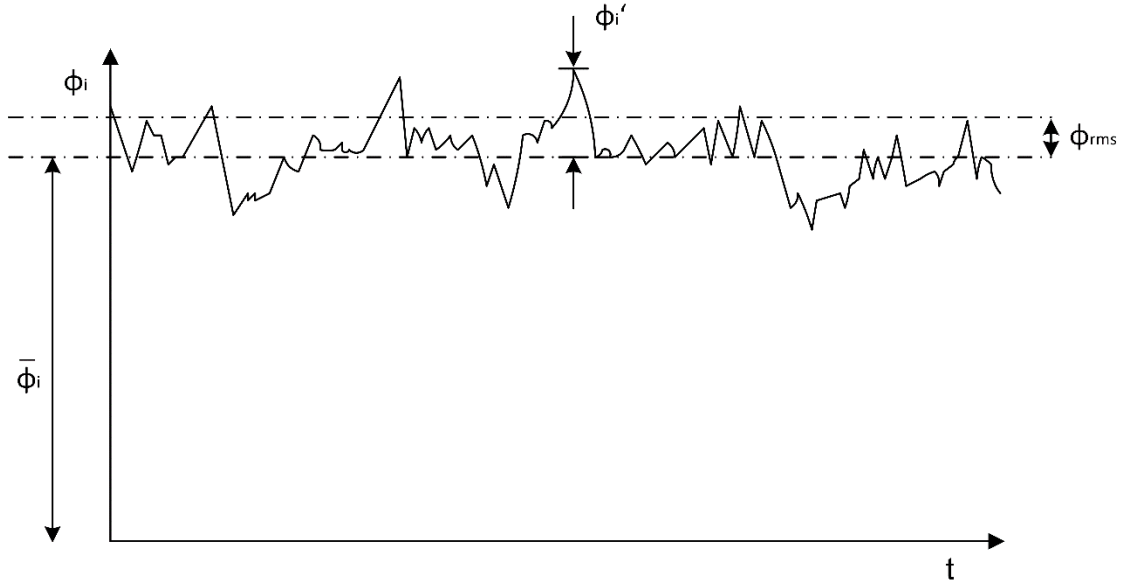

Figure 2-1: Decomposition of instantaneous value into average and fluctuation

The fluctuation ϕ' is calculated by subtracting the average from the instantaneous value:

$$\phi_i' = \phi_i - \bar{\phi}_i \qquad 2.9$$

The time average of the fluctuation value ϕ_i' is zero, but not the average of the multiplication of two or more fluctuations. Furthermore, the so-called *root-mean-square (rms)* value is often applied to characterise the average standard deviation of a set of fluctuations:

$$\overline{\phi_i'} = 0 \qquad 2.10$$

$$\overline{\phi_i'\phi_j'} \neq 0 \qquad 2.11$$

$$\phi_{rms} = \sqrt{\frac{\sum_{i=1}^{N}(\phi_i')^2}{N-1}} \qquad 2.12$$

This so-called *Reynolds-decomposition* can be done for velocities, for pressures, densities and temperatures. Evolving the NSE including the split of the values into average and

fluctuation, the so-called *Reynolds Averaged Navier-Stokes equations (RANS)* in x,y,z directions result:

$$\rho * \left(\frac{\partial \bar{u}_x}{\partial t} + \bar{u}_x * \frac{\partial \bar{u}_x}{\partial x} + \bar{u}_y * \frac{\partial \bar{u}_x}{\partial y} + \bar{u}_z * \frac{\partial \bar{u}_x}{\partial z}\right) = k_x - \frac{\partial \bar{p}}{\partial x} + \mu * \Delta \bar{u}_x - \rho * \left(\frac{\partial \overline{u_x{}' u_x{}'}}{\partial x} + \frac{\partial \overline{u_x{}' u_y{}'}}{\partial y} + \frac{\partial \overline{u_x{}' u_z{}'}}{\partial z}\right) \quad 2.13$$

$$\rho * \left(\frac{\partial \bar{u}_y}{\partial t} + \bar{u}_x * \frac{\partial \bar{u}_y}{\partial x} + \bar{u}_y * \frac{\partial \bar{u}_y}{\partial y} + \bar{u}_z * \frac{\partial \bar{u}_y}{\partial z}\right) = k_y - \frac{\partial \bar{p}}{\partial y} + \mu * \Delta \bar{u}_y - \rho * \left(\frac{\partial \overline{u_x{}' u_y{}'}}{\partial x} + \frac{\partial \overline{u_y{}' u_y{}'}}{\partial y} + \frac{\partial \overline{u_y{}' u_z{}'}}{\partial z}\right) \quad 2.14$$

$$\rho * \left(\frac{\partial \bar{u}_z}{\partial t} + \bar{u}_x * \frac{\partial \bar{u}_z}{\partial x} + \bar{u}_y * \frac{\partial \bar{u}_z}{\partial y} + \bar{u}_z * \frac{\partial \bar{u}_z}{\partial z}\right) = k_z - \frac{\partial \bar{p}}{\partial z} + \mu * \Delta \bar{u}_z - \rho * \left(\frac{\partial \overline{u_x{}' u_z{}'}}{\partial x} + \frac{\partial \overline{u_y{}' u_z{}'}}{\partial y} + \frac{\partial \overline{u_z{}' u_z{}'}}{\partial z}\right) \quad 2.15$$

Paying attention to the last two terms of the equations above and expressing those by means of the index notation yields

$$\frac{\partial}{\partial x_j}\left(\mu * \frac{\partial \overline{u_\iota}}{\partial x_j} - \rho * \overline{u_\iota{}' u_j{}'}\right) \quad 2.16$$

The expression in the brackets of eq. *2.16* corresponds to the total shear stress [12]:

$$\tau_{ij} = \mu * \frac{\partial \overline{u_\iota}}{\partial x_j} - \rho * \overline{u_\iota{}' u_j{}'} \quad 2.17$$

Comparing this equations to the NSE how they are formulated without taking turbulence into account (equations 2.2 – 2.4), it is conspicuous that besides the viscous term an additional term contributes to the total shear stress. The additional term that induces turbulent quantities is called *Reynolds stress* $\tau_{ij}{}^R = -\rho * \overline{u_\iota{}' u_j{}'}$ *[32].* Accurately, it has to be mentioned that the Reynolds stresses are no stresses in the literal sense of the word. They rather present the flux of momentum that is induced by turbulence. However, by pretending that $\tau_{ij}{}^R$ is a stress, the momentum flux due to turbulence can be taken into account [12].

2.2 Dimensionless numbers

For being able to apply theories and observations that have been made in experiments not only to one specific, but rather to a whole class of situations, dimensionless numbers are used. Several dimensionless numbers exist; this paragraph explains the ones that are important for the phenomena described in this work are explained in this paragraph.

Reynolds number

The Reynolds-number is the ratio of inertial forces to viscous forces within a fluid. It is often used to characterize the shift from laminar to turbulent flow.

$$Re = \frac{v_c * l_c}{\mu} \qquad 2.18$$

v_c is a characteristic velocity, l_c a characteristic length and μ the dynamic viscosity of the fluid.

Weber number

The Weber number is applied for describing the behaviour of two-phase flows. It is the ratio of inertial forces to surface forces:

$$We = \frac{\rho * {v_c}^2 * l_c}{\gamma} \qquad 2.19$$

where ρ is the density and γ the surface tension.

Froude number

The Froude number is defined as the ratio of flow inertia to the external field of forces (e.g. gravity force). It is an important number to describe wave propagation on free surfaces:

$$Fr = \frac{v_c}{\sqrt{g * l_c}} \qquad 2.20$$

Stokes number

The Stokes number is used to characterize the behaviour of particles suspended in a fluid flow.

It is the ratio of the characteristic time of a particle to the characteristic time of the flow

$$St = \frac{\tau_P}{\tau_F} = \frac{\tau_P v_c}{l_c} \qquad 2.21$$

2.3 Viscosity

In any given flow, there are not only normal forces due to pressure, but also tangential forces due to shear stresses. Describing a real flow by using the theory of ideal fluids and thus assuming incompressibility as well as neglecting the effects of viscosity may, in some cases, yield satisfactory results. But in many cases, estimating the behaviour of a flow without taking friction into account that has an influence on both the layers inside the fluid and the fluid's boundary with its adjacencies, shows very bad results [35]. To illustrate the huge difference between the models of ideal and real fluids, Figure 2-2 is used:

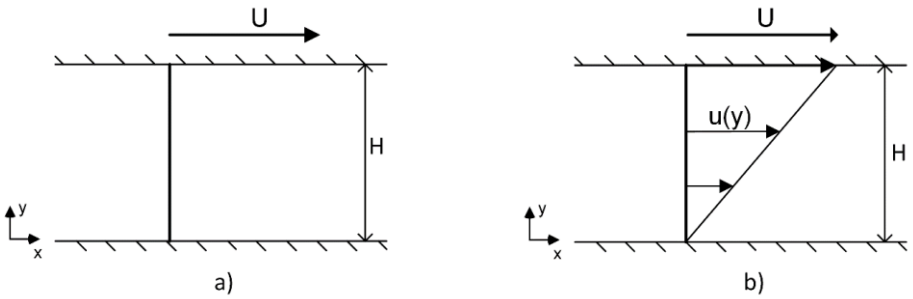

Figure 2-2: a) Ideal fluid, b) Real fluid

The figure shows two solid, infinite, horizontal plates with the constant distance *H*. The upper plate is moving in positive x-direction with the constant velocity U, whereas the lower plate is standing still. In between, there is a Newtonian fluid – in a) an ideal fluid with a viscosity $\mu = 0$, in b) a real, incompressible fluid with a viscosity $\mu > 0$.
It can be observed that the relative movement of the plates does not affect the ideal fluid. As there is no pressure gradient dp/dx, the fluid remains still: $u(y) = const. = 0$. However, the fluid that is shown in b) adheres to both plates (so-called no-slip condition), so that the velocity of the flow equals that on the plates: $u(0) = 0,\ u(H) = U$. A flow field is induced by the movement of the plates relative to each other. Equation *2.22* derives the linear correlation between flow velocity *u,* plate velocity *U* and *y*-position in the channel:

$$u(y) = \frac{y}{H} * U \qquad 2.22$$

Besides the motion of the fluid, a tangential force in x-direction must act on the upper plate to maintain the state of motion. Conducted experiments have shown that the force per unit surface area of the plate (shear stress τ) is proportional to U/H [39]. The constant of proportionality that correlates τ with U/H is the *dynamic viscosity μ.* By substituting U/H for du/dy, the elementary law of fluid friction results:

$$\tau = \mu * \frac{du}{dy} \qquad 2.23$$

The viscosity is a physical property of a fluid and is dependent on pressure and temperature.
By dividing the dynamic viscosity μ by the fluid's density ρ yields the *kinematic viscosity* ν*:*

$$\nu = \frac{\mu}{\rho} \qquad 2.24$$

2.4 Surface tension

At liquid-gas interfaces, a free surface exists. Free surfaces show the phenomenon of surface tension. Figure 2-3a) is well suited to understand the principle of surface tension:

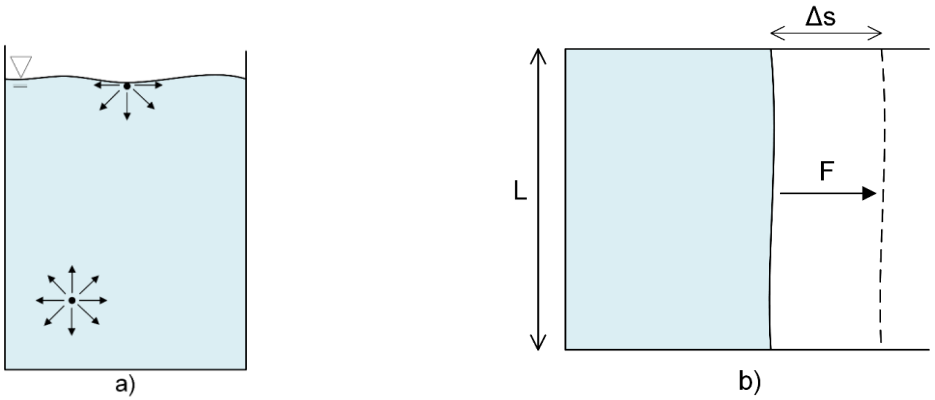

Figure 2-3: a) Model of molecules inside water, b) Stretching a liquid film

Inside the volume of the liquid, intermolecular forces cancel each other out. Gas molecules that are located at a free liquid surface don't exert intermolecular forces on the molecules of the liquid [48], thus the missing negative binding energy can be assumed as a positive energy added to the surface of the liquid. To reach a state of minimum energy, free surfaces are formed as small as possible. Containing a higher amount of energy, forces must perform positive work against surface forces to create a larger surface area, as presented in Figure 2-3b).

These forces are represented by the *surface tension* γ*,* which is a property of the fluid pairing and defined as the force per length of the boundary [48]:

$$\gamma = \frac{F}{L} \qquad 2.25$$

Figure 2-4 shows the surface tension of water in dependence of the temperature. The diagram is based on formula *2.26* [44]

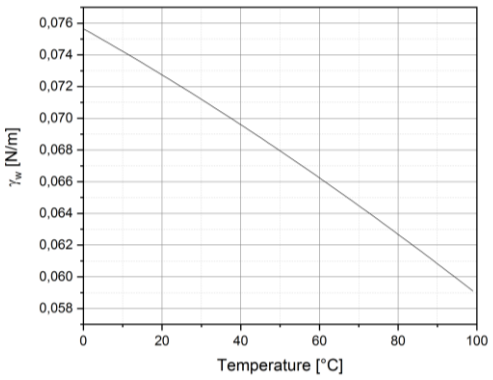

Figure 2-4: Surface tension of water

$$\gamma_W = B\left[\frac{T_c - T}{T}\right]^{1.256} + \left[1 - 0.625\left(\frac{T_c - T}{T}\right)\right] \qquad 2.26$$

with $B = 0.2358$ N/m and $T_c = 647.15$ K.

Furthermore, the surface tension equals the ratio of change of energy to the created surface:

$$\varepsilon = \frac{\Delta E}{\Delta A} \qquad 2.27$$

To prove this statement, the boundary with the length *L* is shifted by the distance Δs. The work $\Delta W = F * \Delta s = 2 * \gamma * L * \Delta s$ equals the change of energy $\Delta E = \varepsilon * \Delta A = 2 * \varepsilon * L * \Delta s$, and thus:

$$\gamma = \varepsilon \qquad 2.28$$

Using this relationship, it is quite easy to estimate the amount of energy that is needed to create a specific surface area. This applies to many technical fields, especially in domains where surfaces are continuously rebuilt, as it is the case with the atomization of liquids.
Talking about atomization, it gets quite clear that not planar, but spherical boundary surfaces are of great interest for many applications. An example are water droplets (liquid phase surrounded by gas) or bubbles (gas surrounded by liquid). In both cases, the surface tension contracts the surface to a minimum, until the equilibrium between the outward-acting internal pressure and the inward force caused by the surface tension is reached. The *Young-Laplace law [25]* describes the correlation between surface tension and pressure increase inside the droplet/bubble:

$$\Delta p = \gamma * \left(\frac{1}{r1} + \frac{1}{r2}\right) \qquad 2.29$$

where $r1$ and $r2$ are the principal radii of curvature. For spheres with $r1 = r2$, the equation simplifies to formula *2.30*:

$$\Delta p = \frac{2\gamma}{r} \qquad 2.30$$

2.5 Hydrostatics and buoyancy

Hydrostatics deal with liquids that not in motion. As there is no flow, neither shear forces nor forces of inertia act on the liquid. Thus, only body forces and contact forces act on the fluid, more precisely those that result from pressure and those that are caused by gravity[1]. Figure 2-5 shows the equilibrium of forces in y-direction:

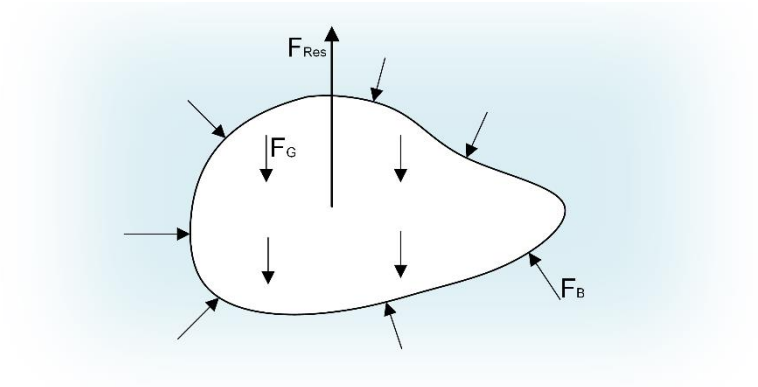

Figure 2-5: Body surrounded by fluid

A body with the density of mass ρ, the volume V and surface S is situated in a fluid with the density ρ_F. Gravity acts on both the body and the fluid. There is an additional force acting on the surface of the body, which is called buoyancy force F_B:

$$F_G = \int_V \rho g \; dV \tag{2.31}$$

$$F_B = -\oint_S p \; dS \tag{2.32}$$

or, by applying Gauss' theorem [25]:

$$F_B = -\int_V \rho_F \, g \, dV \tag{2.33}$$

Hence, the equilibrium of forces in y-direction yields the resulting force F_{Res}:

$$F_{Res} = F_G + F_B = V * g * (\rho_F - \rho) \tag{2.34}$$

In case of equality of both densities, the resulting force vanishes.

[1] Another body force that can act on a fluid at rest is magnetism, but in this work only the influence of gravity is relevant

2.6 Bubble dynamics

2.6.1 Terminal velocity of rising bubbles

For air bubbles dispersed in water, the buoyancy force is stronger and acts in the opposite direction as gravity. This leads to an upward movement of the bubbles. Figure 2-6 shows the equilibrium of forces in a straight-line, steady motion.

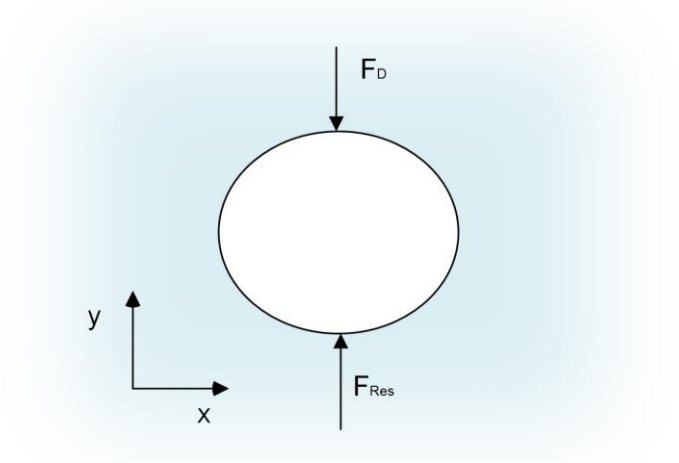

Figure 2-6: Resulting force and drag force acting on an air bubble

F_{Res} is derived in equation 2.34, F_D is the drag force that acts in the opposite direction to the movement. The equilibrium of forces yields equation *2.35*:

$$F_D = F_{Res} = F_G + F_B = V * g * (\rho_L - \rho_G) \qquad 2.35$$

where ρ_L is the mass density of the liquid and ρ_G that of the bubble. To calculate the drag force acting on the bubble, the NSE have to be simplified for solving for two different cases: It has to be distinguished between flow regimes where the viscosity of the fluid can be neglected (*Newton's law)* and flows where inertia forces are not taken into account *(Stokes' law).*

Newton's resistance law

Newton's law can be applied at Reynolds numbers greater than 1000. In this range of Reynolds numbers, inertial forces are much higher than forces due to viscosity. However, the drag force that results can be calculated by equation *2.36* [19]:

$$F_D = c_D * \frac{\pi}{8} * \rho_L * {d_B}^2 * v^2 \qquad 2.36$$

where c_D is a constant called *drag coefficient*.

Stokes' law

The other extreme, neglecting inertial forces compared to viscous forces, is described by Stokes' law and can be applied for Reynolds numbers below 1. As the Reynolds number describes the ratio of inertial forces to viscous forces, small Re can be found in laminar flow regimes, which are the result of either a low velocity, small specific length, high viscosity or a combination of them. Applying the simplifications to the NSE, the nonlinear

terms of the equation vanish, and the drag force that act in the opposite direction to particle motion is obtained [19]:

$$F_n = \pi \mu_L v d_B \qquad 2.37$$

$$F_\tau = 2\pi \mu_L v d_B \qquad 2.38$$

where F_n is the *form component*, and F_τ the *friction component* of the drag force. Combined, the total drag force results:

$$F_D = 3\pi \mu_L v d_B \qquad 2.39$$

Comparing the drag force given by Stokes' law to the one given by Newton's law yields:

$$F_D = 3\pi \mu_L v d_B = c_D \frac{\pi}{8} \rho_L {d_B}^2 v^2 \quad for\ Re < 1 \qquad 2.40$$

and, solving for the drag coefficient:

$$c_D = \frac{24 \mu_L}{\rho_L v d_B} = \frac{24}{Re} \qquad 2.41$$

Figure 2-7 shows the drag coefficient in dependence of the Reynolds number. For $Re < 1$, $c_D = 24/Re$. For $1000 < Re < 200000$, c_D remains quite constant at a value of approximately 0,4 [6]. In between these two regions there is a transitional regime.

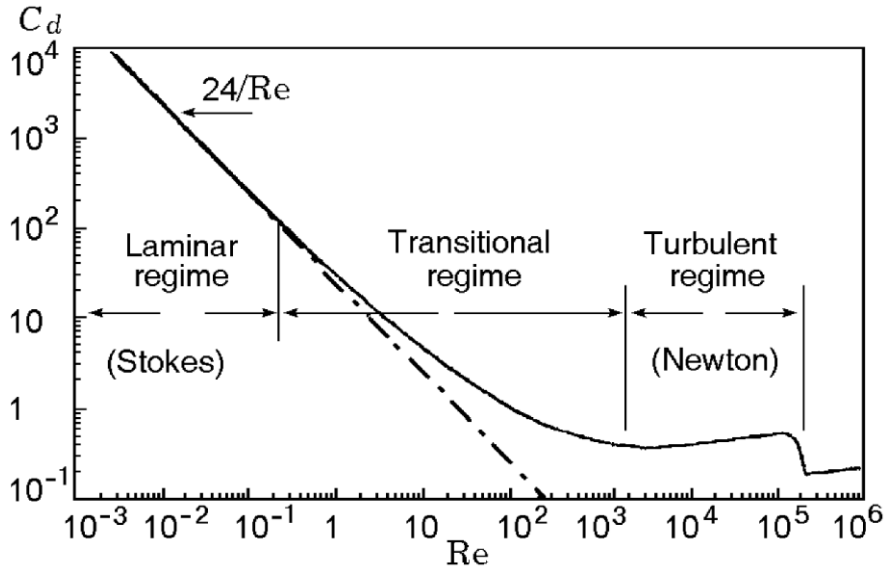

Figure 2-7: Drag coefficient as a function of Reynolds number for a sphere [4]

Thus, to calculate the terminal velocity for bubbles, a differentiation has to be made between small bubbles (high surface tension leads to approximately spherical shapes, low Re due to small diameter), big bubbles (not spherical and higher Re) and those that are of intermediate size.

For *small bubbles*, the terminal velocity v_T can be estimated by solving equation *2.36* by inserting equation *2.39*:

$$v_T = \frac{1}{18}\frac{g{d_B}^2(\rho_L - \rho_G)}{\mu_L} \qquad 2.42$$

For *larger bubbles*, [13] gives the following correlation:

$$v_T = 0.707 * \sqrt{g d_B} \qquad 2.43$$

2.6.2 Coalescence and break-up of bubbles

Individual air bubbles that are dispersed in a liquid can merge with other bubbles (coalescence) - or it is possible that they split and decay into smaller bubbles (break-up). The mechanisms that lead to these two phenomena are explained briefly.

Coalescence
The process that occurs can be divided in three main parts, see Figure 2-8.

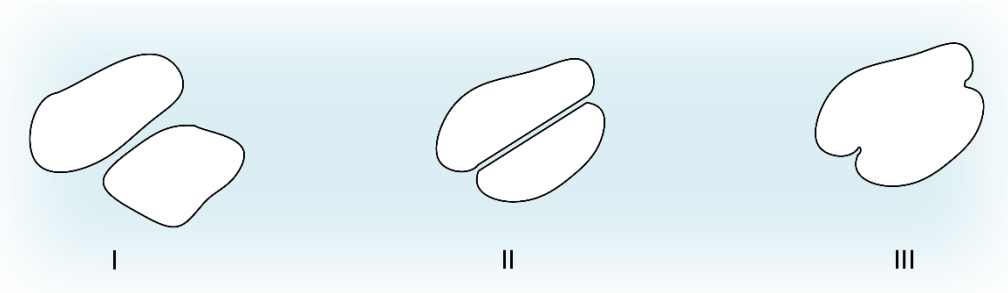

Figure 2-8: Bubble coalescence

Colliding bubbles, as seen in the first illustration, trap a small amount of liquid between them. They approach further and a liquid film is built between them. The liquid drains until a critical thickness is reached. Sketch III shows the rupture of the liquid film and the coalescence of the two individual bubbles.

The mechanisms that cause the collisions of bubbles can be turbulence, buoyancy or laminar shear [36]. The random motion of turbulence obviously leads to collision of bubbles that are moved by the flow. Bubbles of different sizes experience different forces of buoyancy, and therefore they have different rising velocities which enables the possibility of collisions.

Bubble break-up
Bubbles break up due to interactions with turbulent eddies. To be able to split bubbles, the eddies must be equal or slightly smaller than the bubbles. Large eddies simply transport the bubbles, whereas very small eddies don't provide sufficient energy to cause a bubble break-up.

2.7 Turbulent circular jets

The turbulent stream of a fluid through a nozzle into a surrounding, quiescent medium of the same kind is hereafter referred to as *turbulent jet.* The evolved flow field of a turbulent jet is illustrated by Figure 2-9:

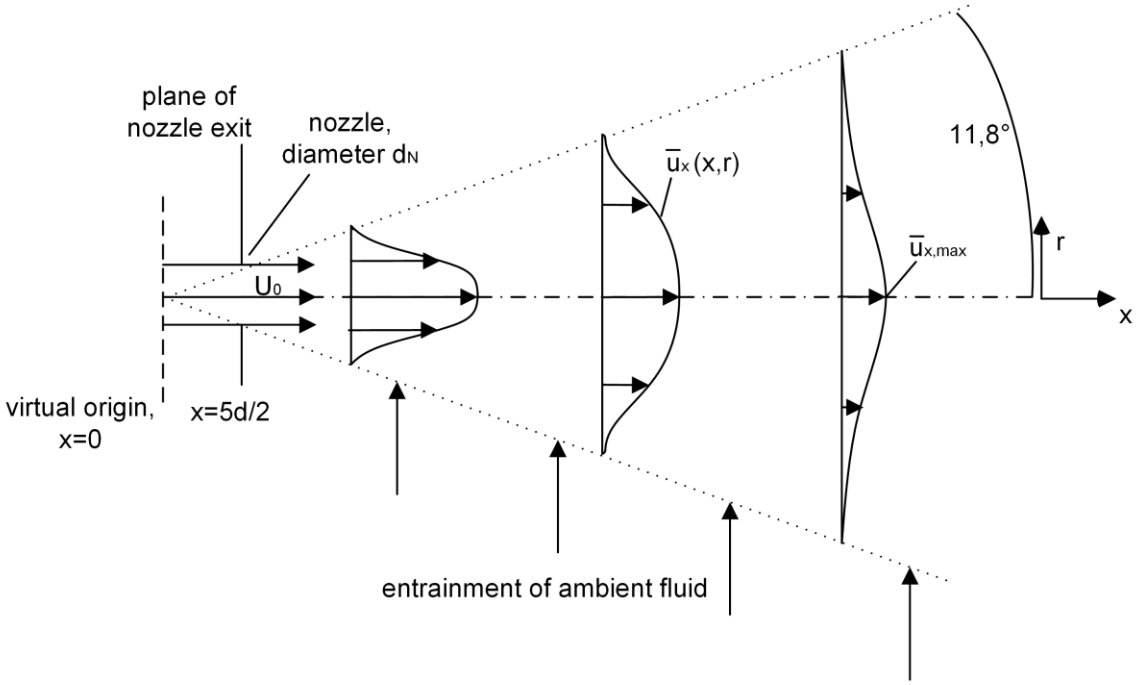

Figure 2-9: Schematic illustration of turbulent jet

The fluid flow is driven by the momentum of the source. After having left the nozzle outlet with the velocity U_0, the mass flow of the streaming fluid increases by entraining ambient fluid due to tangential forces caused by shear stresses [24]. Simultaneously, the velocity profile of the jet decreases with increasing x- and r-coordinates. The maximum velocity is found on the symmetry axis, which can be calculated using equation [10]:

$$\bar{u}_{x,max} = \frac{5 * d_N}{x} * U_0 \qquad 2.44$$

Furthermore, the opening angle of the cone-shaped velocity profile that evolves always has the same value of 11,8°, regardless of injection speed U_0, fluid or nozzle diameter [10], provided the injected and the quiescent fluid are the same.

2.8 Liquid jets

This paragraph gives a brief description of liquid jets emanating from a nozzle into an ambient, still gas.
Firstly, it has to be emphasized that these kind of liquid flows are inherently unstable [27]. Several mechanisms exist that lead to a breakup of the jet. It has been found that the reason is the growth of spatial disturbances inside the jet [45]. These depend on the Reynolds number Re, the Weber number We and the gas-to-liquid density ratio [26]. There have been a lot of studies in the past that give a very detailed insight into the behaviour of liquid jets, but regarding the aim of this work it is sufficient to mention some characteristics that are of interest for the conducted experiments. Figure 2-10 shows a sketch of a liquid jet:

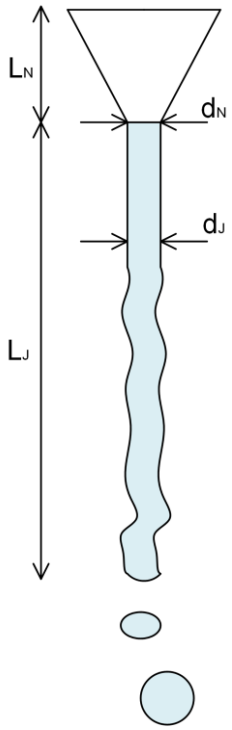

Figure 2-10: Sketch of a vertical, liquid jet

2.8.1 Diameter

To estimate the jet diameter d_J at a discrete length L_J after the nozzle, it has to be distinguished between two cases: a laminar and a turbulent jet.

For *laminar* vertical jets, gravity has a significant influence on the diameter and velocity of the jet. To calculate the jet diameter, an energy balance is used. By neglecting the jet's surface energy and the effects of the ambient gas, equation results [3]:

$$\frac{d_J}{d_r} = \left(\frac{\pi^2 g L_J d_r^4}{8 Q_L^2} + 1\right)^{-\frac{1}{4}} \qquad 2.45$$

Q_L describes the flow rate of the liquid and d_r the diameter of the jet at a reference point. d_r cannot be assumed to be equal to the nozzle diameter. Equation *2.45* is valid when the diameter d_r is taken at $L_J = 0.03$ m.

For *turbulent* jets there is no need to choose a reference point as basis for the calculations. The important diameter is rather that of the nozzle outlet, and thus the diameter can be calculated as [3] :

$$\frac{d_J}{d_N} = 0.125 * (We_N Re_{Length})^{\frac{1}{6}} \qquad 2.46$$

where $We_N = (v_N^2 d_N \rho_G)/\gamma$ and $Re_{Length} = (v_N L_J \rho_G)/\mu_L$. The equation is valid for $We_N Re_{Length} > 7 * 10^5$ and $L_N/d_N \geq 50$.

2.8.2 Velocity

The jet velocity can be calculated by assuming free fall of the liquid after leaving the nozzle [47]:

$$v_J = \sqrt{v_N^2 + 2gL_J} \qquad 2.47$$

2.8.3 Breakup mechanisms

The breakup of a liquid jet is the subject of a huge amount of literature. The release of the fluid into a still gas through a circular nozzle is the case that has been studied most. The mechanism that leads to the breakup is dependent on the forces that are dominant inside the flow. Hence, as different mechanisms appear for different flow regimes, it is reasonable to classify them into different groups, as shown in Figure 2-11:

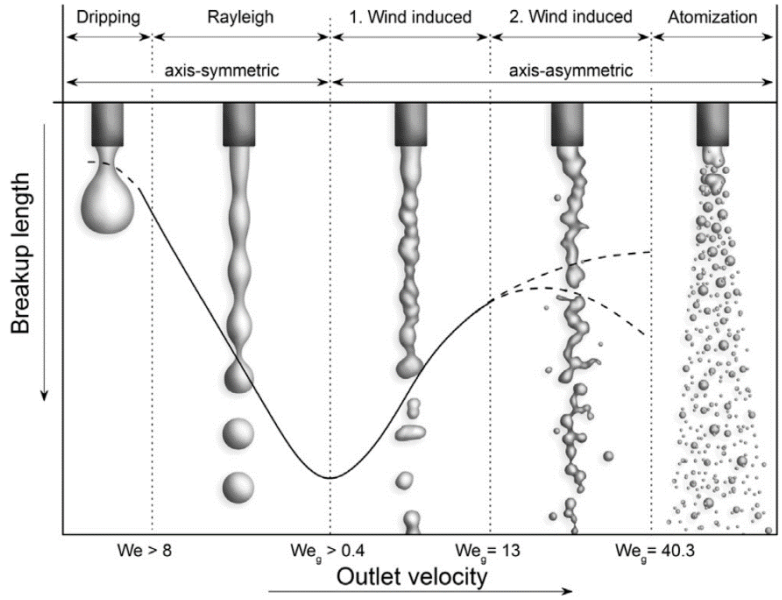

Figure 2-11: Different jet breakup mechanisms [5]

The graphic shows drafts of the appearance of the different types of jets. Furthermore, it shows the relationship between outlet velocity and breakup length in a qualitative way. In

regimes of low velocity, the Weber number of the liquid is used. But as the velocity increases and the interaction between liquid and gas becomes more and more significant, the Weber number of the gaseous phase $We_G = (\rho_G v_f^2 d_J)/\gamma$ is applied.

The first mechanism, dripping, has no relevance for this work. The second mechanism that is shown is the so called *Rayleigh breakup*. It is characterized by low jet velocities, and occurs downstream of the outlet at a distance which is several times the nozzle diameter. The diameters of the single drops are larger than the jet diameter. Increasing the outlet velocity, the *first wind induced* regime follows: The jet shows an uneven contour along its axis. The breakup occurs many nozzle diameters below the nozzle as well, and the diameter of the drops is of the same order of magnitude as the nozzle diameter. The *second wind induced* regime appears at high velocities. Here, the disintegration of the drops that are smaller than the nozzle diameter, occurs much closer to the outlet due to a harsh interaction of the liquid with the ambient gas [46]. The last regime is called *atomization.* The water column disintegrates instantly after exiting the nozzle.

2.9 Plunging jets

A liquid jet that is vertically ejected by a nozzle, traveling through an (initially) still gas and impinging on a receiving pool of the same liquid is, in this work, hereafter referred to as *plunging jet.* This plunging jet causes, in some cases, an entrainment of ambient air into the liquid pool. In other cases, the jet only induces a flow field inside the pool, without any air entrainment. In his work, E. van de Sande refers the first known publication about this phenomenon to *A.T. Mertens (1938),* who made use of the effect of air entrainment to run a chemical reactor [43]. Thereafter, many studies were conducted to understand the mechanisms and influencing factors that determine the physical appearances. In this paragraph, some of the agreeing theories about the fluid dynamics concerning plunging jets are introduced. In the following descriptions, the liquid and gaseous phases are water and air respectively, since the experiments of this work are executed with these substances.

In dependence of the state of the flow, different mechanisms of air entrainment occur. Although literature mentions many different criterions that define the governing mechanisms, the most applicable differentiation that must be made to identify the entrainment mechanism is whether the jet is a laminar or turbulent flow [3, 28, 30]. It has been found that both laminar and turbulent jets can entrain gas, but the mechanisms are quite different. Figure 2-12 illustrates the cases of a smooth, laminar jet (type 1); of a rough, turbulent jet (type 3), and a jet with transitional characteristics (type 2). The nomenclature of these three different mechanisms is not a recognized convention, it is rather an own naming to simplify matters in this work.

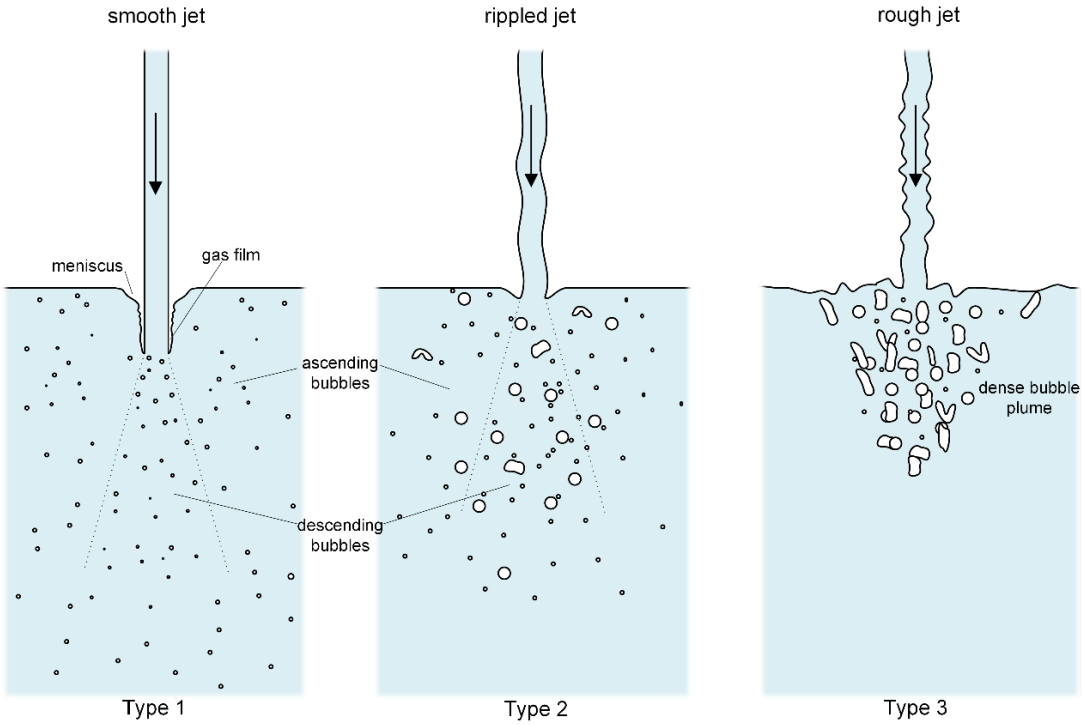

Figure 2-12: Gas entrainment mechanisms

Type 1

A laminar, smooth jet at a low velocity does not entrain gas at all. Just in case of exceeding a critical velocity, a reverse orientated meniscus is developed inside the receiving liquid [3]. Ambient air is transported inside the boundary layer of the jet and has at the liquid/gaseous interface the same velocity as the jet (no-slip condition). Upon impact of the jet on the surface, this air is transported under water. At the impingement point, a gas film develops. The film thickness is of the order of 1 to $5 * 10^{-5}\ m$ and, depending on the system, shows a length of 0 to $4.5\ 10^{-3}\ m$ [28]. The upper part of this gas film remains cylindrical, whereas the lower part oscillates constantly. The instability of the gas film leads to repeating breakups. The air that has been transported under water then forms small bubbles that disperse in the whole bath [20]. Due to the high amount of influences the state of flow as well as the physical properties of the fluids have, a clear criterion that determines the governing air entrainment mechanism could not be found so far. But in his experiments, *van de Sande* [43] never found a gas film around the jet for Reynolds numbers above 2000.

Type 3

The third type appears when the jet surface is rough. The meniscus that has been present at low Reynolds numbers disappears. Figure 2-13 illustrates the entrainment mechanism:

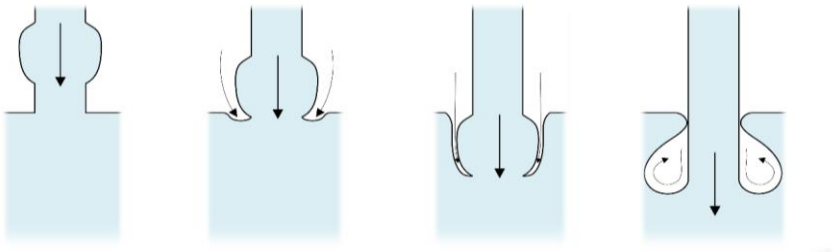

Figure 2-13: Gas entrainment mechanism of a rough jet

The rough jet transports disturbances on the jet surface downstream. When these irregularities hit the water surface, the surface is deformed. When the irregularity has passed the liquid/gaseous surface, a gap results, as the liquid is not fast enough to follow the roughness of the jet. The gap is filled with ambient air. A bubble results, that is much bigger than those that are created by type 1. *McKeogh and Ervine* [30] found that a turbulence intensity greater than $2\ \%$ causes this condition.

Type 2

The transition between type 1 and type 3 represents another type of entrainment mechanism. It occurs when the turbulence intensity in the nozzle is $1\% < Tu < 1.5\%$ [30]. Characteristic for this type of entrainment is an indentation of the water surface at the point where the jet hits the receiving pool. Furthermore, an intermittent vortex that causes an inward radial flow appears on the pool surface. The gas entrainment is carried out by the air that is encompassed within the rippled surface of the jet, as well as by the gas that is transported towards the water surface inside the boundary layer.

3 Fundamentals of applied measurement techniques

3.1 Particle Image Velocimetry (PIV)

Particle Image Velocimetry (PIV) is a technique to analyse the flow of gaseous and liquid fluids. The working principle is shown in Figure 3-1:

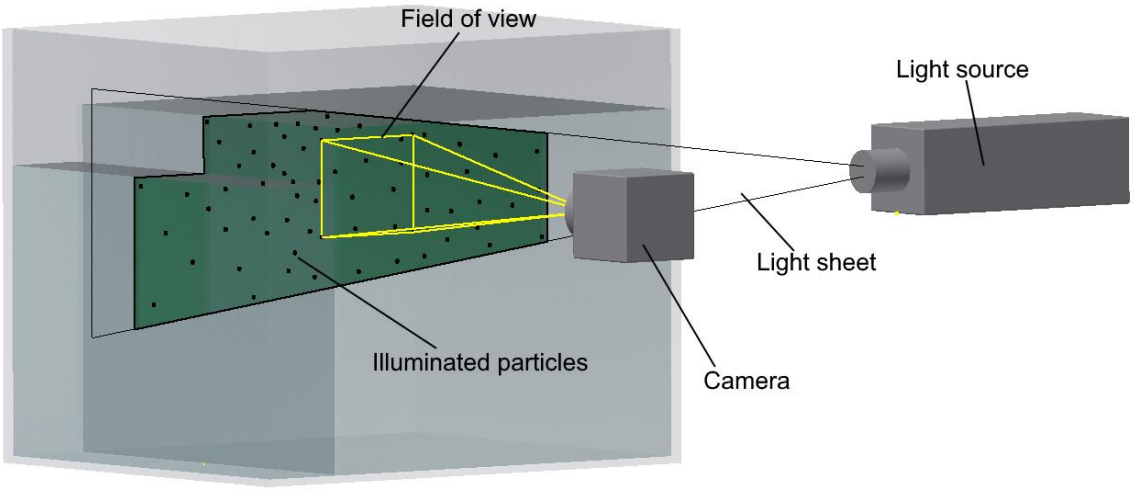

Figure 3-1: Working principle of a PIV setup

For being able to visualize a fluid's movement by PIV, small particles that follow the flow are injected. By illuminating a defined, thin plane within the section of measurement by means of a source of light, the movement of the light emitting particles can be observed, recorded by a camera and transferred to quantitative data by a computer.
To receive information about the field of velocity, the camera records several illuminations of the same section within a short and defined time interval. Equation *3.1* demonstrates the calculation of the velocity $\boldsymbol{u}$ by dividing the particle's displacement $\boldsymbol{x}_2 - \boldsymbol{x}_1$ by the time interval $t_2 - t_1$ [1]:

$$\boldsymbol{u} = \lim_{t_2 \to t_1} \frac{\boldsymbol{x}_2 - \boldsymbol{x}_1}{t_2 - t_1} = \lim_{\Delta t \to 0} \frac{\Delta \boldsymbol{x}}{\Delta t} \qquad 3.1$$

Although the necessity to construct the section of measurement optically accessible and the presence of the particles have an influence on the hydraulic conditions, the technique of PIV is assumed to be non-invasive [17]. PIV has the ability to record instantaneous phenomena and provides quantitative information about the entire flow field at a high sampling frequency. Therefore, PIV is a well suited and efficient process for investigating fast flow fields.

In the following paragraphs, the necessary components of a typical PIV setup are listed and explained. Furthermore, methods for imaging as well as algorithms for evaluating the recorded data are introduced.

3.1.1 Components of a PIV system

In this paragraph, the typical components of a PIV system are listed and explained.

3.1.1.1 Tracer particles

In fact, the measurement devices do not identify the flow itself, but the motion of the tracer particles that are carried along by the streaming fluid. To assign the particle's movement to the flow congruently, the top priority is to avoid considerable discrepancies between particle and fluid motion.
Therefore, it is important not to create buoyancy that does not equal to the magnitude of the force of gravity. This would lead to a motion that deviates from the flow due to a resulting force. Equation *3.2* shows the equilibrium of forces of a particle in a liquid at rest.

$$F_G - F_B = F_D \qquad 3.2$$

Inserting the constitutive parameters for the force of gravity F_G, the buoyancy force F_B and the drag force F_D, equation *3.3* results, which is valid for spherical particles with a diameter greater than $1\ \mu m$ moving in flows governed by Stokes' law:

$$\frac{(\rho_P - \rho_F)\pi d_P^3 g}{6} = 3\pi\mu v d_P \qquad 3.3$$

where ρ_P and ρ_F are the densities of the particle and the fluid, d_P is the particle's diameter and g the constant of gravitation.
Solving the equation for the velocity v, which is also called *terminal settling velocity* v_{TS} [14], gives

$$v_{TS} = \frac{(\rho_P - \rho_F)d_P^2 g}{18\mu} \quad for\ Re < 1\ and\ d_P > 1\ \mu m \qquad 3.4$$

Thus, terminal settling velocity disappears for $\rho_P = \rho_F$.

Besides the requirement of very small settling velocities, the ability to adapt quickly to a change of the flow is desired. Therefore, the *mechanical mobility* B which represents the ratio of the terminal velocity in any direction v_T to the resulting drag force F_D is introduced:

$$B = \frac{v_{TS}}{F_D} = \frac{1}{3\pi\mu d_P} \qquad 3.5$$

Equation *3.5* leads to the particle's *response time* τ_P by multiplying the mechanical mobility with the particle's mass m_P

$$\tau_P = m_P B = \frac{\rho_P d_P^2}{18\mu} \quad for\ Re < 1\ and\ d_P > 1\mu m \qquad 3.6$$

τ_P defines the particle's response time, which is the time the particle needs to achieve 63.21% of the flow velocity when released from rest [9].

Dividing τ_P by a characteristic time scale of the flow τ_F offers the opportunity to compare the particle's response time to the flow's ability to change its motion. The dimensionless ratio of τ_P to τ_F is called *Stokes number* St *[15]*

$$St = \frac{\tau_P}{\tau_F} = \frac{\tau_P v_c}{l_c} \qquad 3.7$$

where l_c is a characteristic length and v_c a characteristic velocity of the flow.This dimensionless number gives a comfortable opportunity for estimating the suitability of tracer particles for the existent flow, as it is known that the particles follow the fluid's streamlines perfectly for $St \ll 1$ [8, 19].

Besides the constraint to have a small diameter, the particle's light scattering behaviour has a significant influence on the quality of the picture that is taken. Especially for obtaining a high *signal-to-noise ratio*, a high image intensity, which is directly proportional to the scattered light power [38], is desired [31]. It can be observed that larger particle diameters cause a higher intensity of the scattered light [17, 31, 38]. Therefore, in the process of choosing the ideal tracer particles always exists an antagonism between a fast particle response time in the fluid (small diameter) and a high intensity of the scattered light (large diameter).

3.1.1.2 Illumination

To illuminate the particles, an intensive source of light is needed. To obtain a sharp-cut picture a very short length of exposure is required. On the other hand, a very intensive source of light is needed to increase the intensity of the scattered light. Therefore, lasers are well suited and widely applied as light source in a PIV setup. Not only the ability to create short light pulses, but the characteristic of the monochromatic light with a high energy density that avoids chromatic aberrations and ensures a homogenous illumination of the plane [38] is desirable.
Furthermore, optical devices to transform the laser beam into a thin light sheet are required. In general, this is realized by a combination of cylindrical lenses.

3.1.1.3 Camera

To capture the images, a camera and a system of lenses is required. Presently, there are two main technologies used in cameras for constructing the sensors that convert the incident light into digital data: *CCD (Charge-Coupled Device)* and *CMOS (Complementary Metal-Oxide Semiconductor)*. Both chips consist of picture elements (pixels) that register the amount of light that enters the camera. But the way where and how the pixels' electric charge is converted to voltage and thereby made interpretable for the processor is different.
With reference to Particle Image Velocimetry, the most important differences between the two sensor types concern the quality and the frequency of the pictures that are taken.
In a *CCD* sensor, the photogenerated charge is moved from pixel to pixel. In an output node, it is converted to voltage [29]. This analogue signal is amplified and converted to a digital signal outside the sensor.

Due to the fact that the conversion to voltage as well as the amplification of every pixel's output takes place in the same device, a very homogeneous signal with a low level of Fixed Pattern Noise can be achieved using a CCD sensor [29].
CMOS imagers convert charge to voltage inside each pixel. The chip includes amplifiers and converters that are needed to produce an image – every pixel produces its own voltage output, and the digital signal is created inside the chip. The parallel reading of the imaging information leads to a higher rate of taking pictures compared to a CCD chip.

3.1.2 Procedure

After having taken the pictures, the gained digital data must be interpreted and converted to a form that provides information about the physical experiment in an adequate quality. Thus, the pictures must be corrected for eliminating optical and perspective distortions as well as assigned to a physical scale. Afterwards, the pictures can be used to evaluate the flow speed and direction on the basis of the identified particle's displacement and the time interval between the exposures. Additionally, in the step of post-processing, the obtained data can be edited in retrospect to extract the essential information out of the data volume.

3.1.2.1 Calibration

For calibrating the setup, an object with marks that are known in its dimensions must be compared to the projected picture the camera chip captures. To calibrate a two-dimensional PIV setup, the calibration target is placed inside the camera's field of view and inside the light sheet, as seen in Figure 3-2.

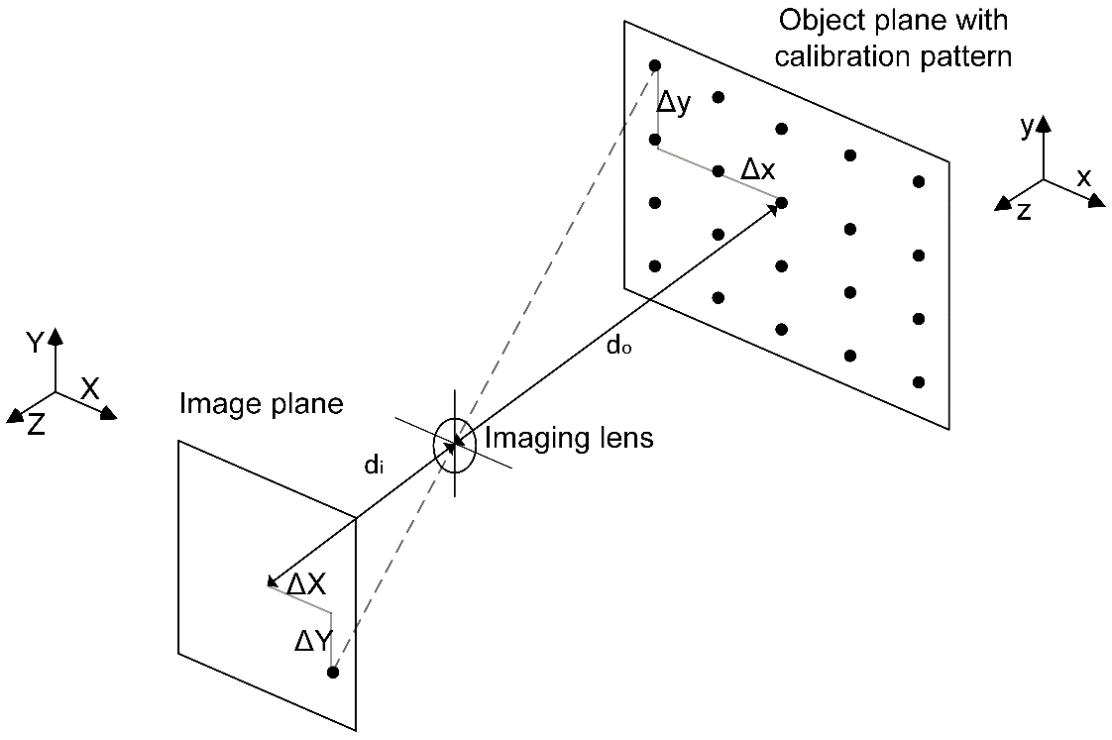

Figure 3-2: Transfer from object to image plane

Assuming a recording without any optical and perspective distortions, the mapping function that describes the correlation between physical dimensions on the planar object plane (x, y) and the dimensions on the image plane (X, Y) is just a constant value M that is derived from the *object distance* d_o and the *image distance* d_i:

$$M = -\frac{d_i}{d_o} \qquad 3.8$$

So, the correlation between the object's physical position and its projected position on the sensor is calculated by the following formula:

$$M * \boldsymbol{x} = M * \begin{pmatrix} x \\ y \end{pmatrix} = \begin{pmatrix} X \\ Y \end{pmatrix} = \boldsymbol{X} \qquad 3.9$$

But as soon as the camera sensor is placed in a position that is not exactly parallel to the light sheet, a perspective distortion appears. Furthermore, optical distortions caused by irregularities in the lenses occur often. For that reason, a scalar value that describes the correlation between object- and image plane is in the most cases not sufficient to calibrate a PIV setup. In the best case, a mapping function $\boldsymbol{F}(\boldsymbol{x})$ is found that determines how the positions on the object plane are related to those on the image plane:

$$\boldsymbol{X} = \boldsymbol{F}(\boldsymbol{x}) \qquad 3.10$$

But in reality, identifying a function $\boldsymbol{F}$ that yields zero error in the projected geometry is not possible. Instead of that, an estimate for the mapping function, $\widehat{\boldsymbol{F}}$, is derived. A multi-cubic polynomial is well suited and able to compensate the distortions sufficiently well in the most cases [40]:

$$\begin{aligned} \widehat{\boldsymbol{F}}(\boldsymbol{x}) = \; & \boldsymbol{a}_0 + \boldsymbol{a}_1 x + \boldsymbol{a}_2 y + \boldsymbol{a}_3 z + \boldsymbol{a}_4 x^2 + \boldsymbol{a}_5 xy + \boldsymbol{a}_6 y^2 + \boldsymbol{a}_7 xz + \boldsymbol{a}_8 yz + \boldsymbol{a}_9 z^2 \\ & + \boldsymbol{a}_{10} x^3 + \boldsymbol{a}_{11} x^2 y + \boldsymbol{a}_{12} xy^2 + \boldsymbol{a}_{13} y^3 + \boldsymbol{a}_{14} x^2 z + \boldsymbol{a}_{15} xyz + \boldsymbol{a}_{16} y^2 z \\ & + \boldsymbol{a}_{17} xy^2 + \boldsymbol{a}_{18} yz^2 \end{aligned} \qquad 3.11$$

The vectors $\boldsymbol{a}_i$ are the coefficients that have to be identified by calibration. In case of a two-dimensional PIV, $z = 0$.

3.1.2.2 Recording

To obtain information about the movement of the particles, the recording must either range over a time interval that is long enough to show the trajectory or take place at diverse discrete moments. Furthermore, the methods can be separated into two main branches: single frame techniques, which capture all the action on one single picture, and multi-frame techniques, that use not only one picture overall, but one picture per illumination [1].

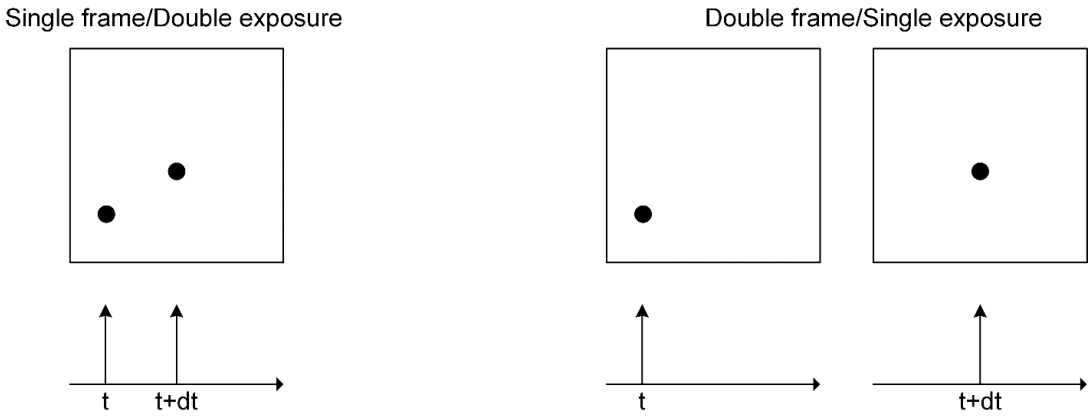

Figure 3-3: Recording techniques

Capturing the field of view at two moments of time in only one frame registers the flow velocity, but does not give information about the direction of the flow. For that reason, a lot of approaches like image shifting, pulse tagging, colour coding etc. have been developed to receive both dimensions out of the single frame [38].
The progressing development in photography and especially the concept of digital cameras enabled the method of single exposure in two or more fast consecutive frames. Since the particle's chronological position is clearly traceable from frame to frame, the pictures include the information about the velocity as well as about the direction of the particle without the necessity to implement further arrangements.

3.1.2.3 Image evaluation

Having captured the particles on the pictures, the information about the flow field must be extracted out of them. Initially, the interrogation was executed manually: The particle's spatial shift was observed by tracking a particle from frame to frame, and thereby the fluid's flow could be reconstructed [11]. Digital photography as well as the development of fast operating computers enabled an automation of the interrogation schemes. But due to the fact that particle tracking velocimetry (PTV) requires a very spare density of the dispersed tracer particles for being able to identify the same tracer in two or more consecutive frames, the density of information that is carried by the seeding is poor. Increasing the concentration disables the possibility to recognize a particle in sequenced recordings. Hence, the particle image velocimetry operates by deriving an average displacement of local groups of particles [21], called *interrogation areas (IA)* or *interrogation windows.*

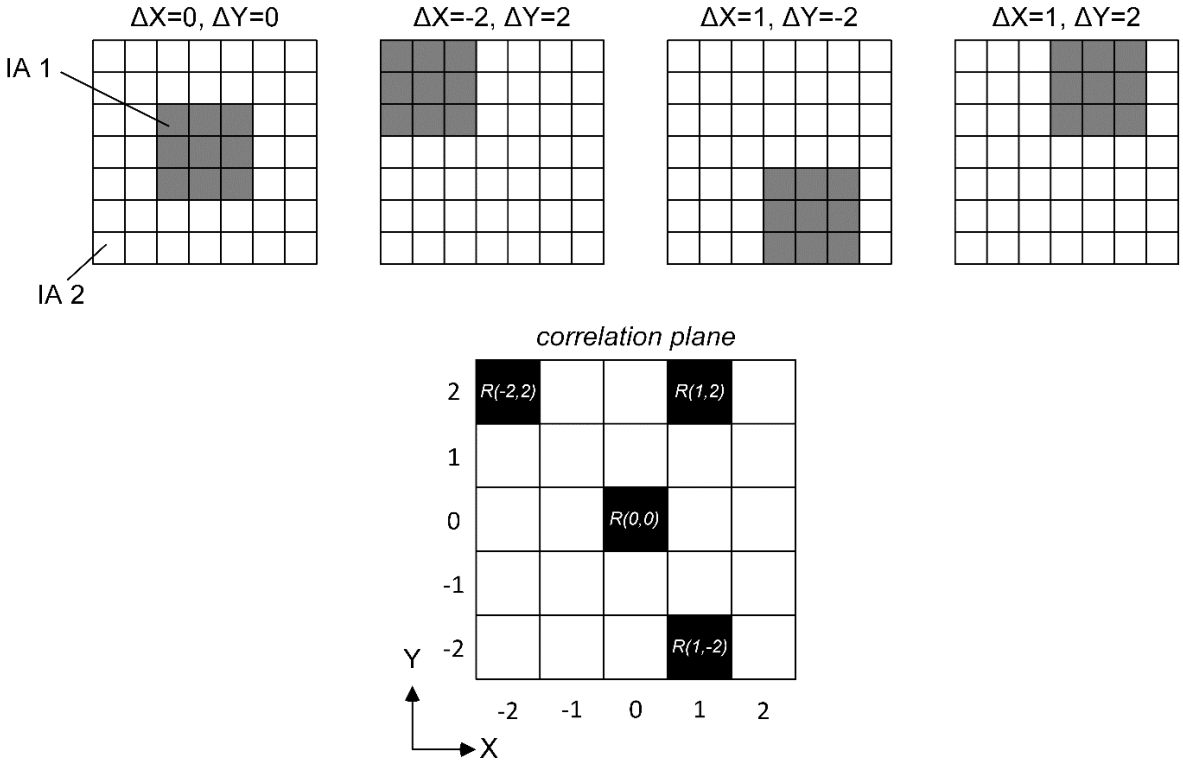

Figure 3-4: Principle of a correlation plane, built by direct cross-correlation

Figure 3-4 visualizes the principle of the *cross-correlation* interrogation scheme. IA 1 contains the information about the pixel's intensities at the time t_0, IA 2 those at the time $t_0 + dt$. To estimate the movement of the group of particles that takes places, IA 1 is shifted linearly in IA 2. For each shift, the sum of the products of all overlaid pixel intensities produces a cross-correlation value R. By shifting IA 1 in every possible position in IA 2 and noting every R in a separate cross-correlation plane, the maximum cross-correlation value can be interpreted as the most probable shift of the particles within the time span dt. So the PIV analysis of the experiment will return one vector per interrogation area. It is obvious that the smaller the interrogation areas, the more vectors are obtained in the field of view. On the other hand, a small interrogation area can lead to a decreasing accuracy. A suitable indicator for evaluating the validity of the found correlation peak is the *detectability* D, as the ratio of the maximum peak to the second tallest peak value [21]. The choice of the optimum interrogation area size depends on the camera and the application. In a series of experiments that ranged from areas of $12x12\ pixels^2$ up $to\ 128x128\ pixels^2$, [2] found that an area of $32x32\ pixels^2$ achieved the best results.

3.2 Shadowgraph imaging

The method of shadowgraph imaging is a simple form of optical system to observe density variations in light-transmissive media. The physical effect the working principle is based on is the fact that light travelling through a medium is refracted when hitting areas of differing densities. Projecting these light beams on a screen, the refraction can be noticed by sectors of different light intensities. Thus, to observe these fluctuations of light intensity, the system does not need any optical devices except a recording plane and a light source. The following paragraphs provide a deeper insight into the physics of shadowgraph imaging, the field of application and a possible laboratory installation.

3.2.1 Setup

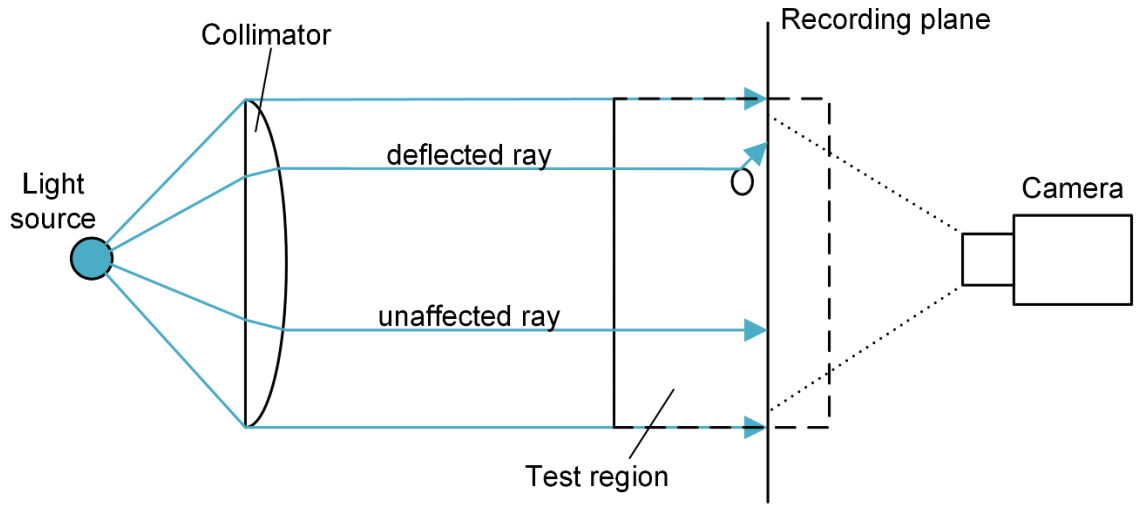

Figure 3-5: Working principle of a shadowgraph imaging setup

A source of light, often an expanded and collimated laser [34], is installed in such a way as to enable the beam to pass through the test region. The light rays that pass regions of homogeneous density are not affected by refraction and reflection. Those that pass density gradients are refractively deflected, and those that pass a boundary surface are partially or totally reflected. The consequence is a deviation of the light rays from their original path, which results in a change of intensity on the screen or recording plane of the camera compared to a reference sample. Shadowgraph imaging measures this intensity distribution.

3.2.2 Reflection and refraction of light

The *speed of light* c depends on the medium that transmits the light waves, *3.12* shows the dependence of the wavelength λ and the frequency f on c:

$$c = \lambda * f \qquad 3.12$$

The speed of light in vacuum c_0 is $299792458\ m/s$. In every medium, the transmitted light has another speed due to a differing λ. Hence, every medium is characterized by its refractive index n, that is defined as the ratio of the speed of light in vacuum to the medium's respective speed of light c_n [42]:

$$n = \frac{c_0}{c_n} \qquad 3.13$$

Furthermore, the speed of light and therefore also the refractive index can deviate within an individual medium, depending on the local density. This deviation is described by the *Gladstone-Dale-relationship* [16].
When a light ray hits a boundary of two different media, a part of the light is reflected and another part reaches the second medium. If the light ray does not hit the boundary surface perpendicular ($\theta_1 \neq 90°$), the emergent angle θ_2 of the transmitted ray is not identical to the angle of incidence: $\theta_1 \neq \theta_2$. This effect is called *refraction*, and is shown in Figure 3-6.

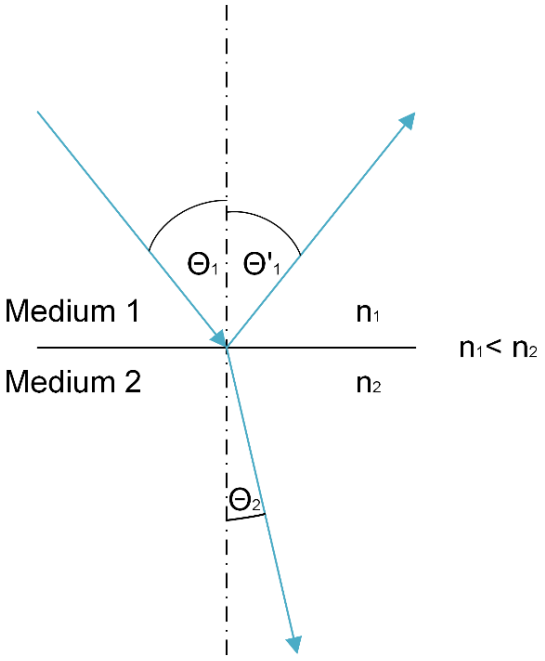

Figure 3-6: Light refraction

The exact relationship between the angle of incidence, the emergent angle and the refraction index n is described by *Snell's law [42]*:

$$\frac{\sin(\theta_2)}{\sin(\theta_1)} = \frac{n_1}{n_2} \qquad 3.14$$

By setting the emergent angle θ_2 zero, the critical angle θ_c can be calculated:

$$\theta_c = \arcsin\frac{n_2}{n_1} \qquad 3.15$$

In case of exceeding this angle, the incident light is not transmitted through the boundary surface, but completely reflected [42]. This phenomenon is called *total reflection,* and can only occur for rays that are traveling from a more to a less optically dense medium ($n_1 > n_2$).

3.2.3 Application of shadowgraph imaging for bubbly two-phase-flows

Due to the big ratio of the refractive indices of water $n_W = 1{,}33251$ to air $n_A = 1{,}00028$ [18], light rays that hit the boundary surface suffer a strong deflection due to refraction (for $\theta_1 \neq 90°$). Furthermore, the surface always reflects a part of the light. Exceeding the critical angle θ_c, total reflection occurs and all the light is reflected. *3.16* calculates θ_c for waves that travel through water and hit the water/air boundary:

$$\theta_c = \arcsin\frac{n_2}{n_1} = \arcsin\frac{n_A}{n_W} = 48{,}65° \qquad 3.16$$

Figure 3-7 illustrates three different cases for incident light rays:

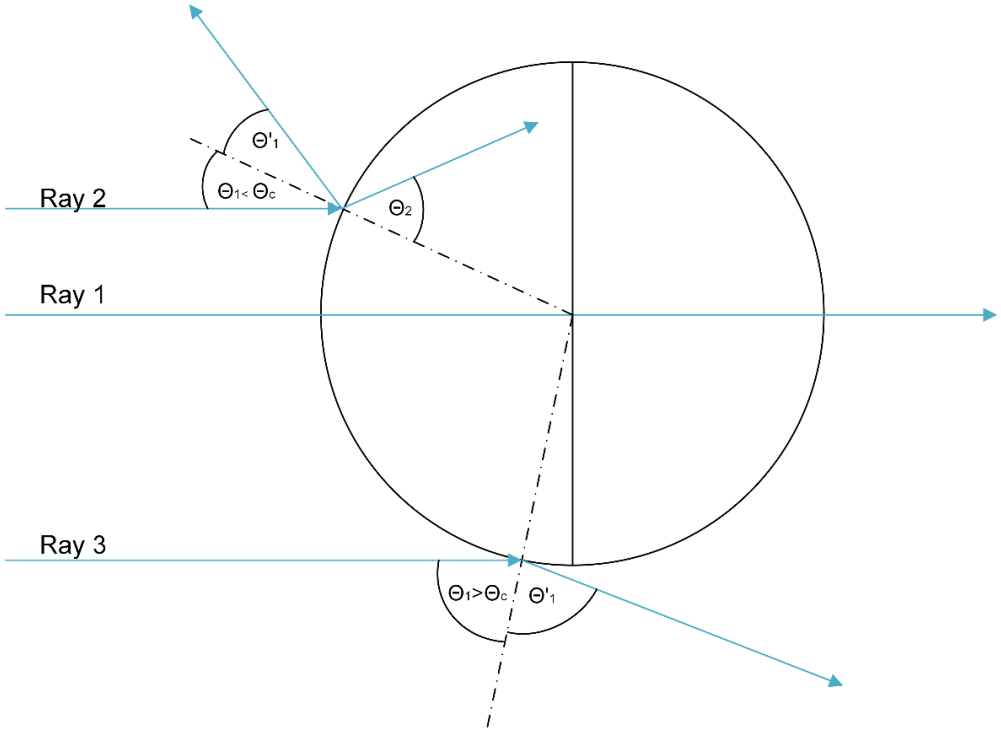

Figure 3-7: Incident light rays on a bubble

Light ray 1 hits the surface at an angle $\theta_1 = 90°$. The wave is partially reflected, the other part travels through the air bubble without deflection. *Light ray 2* hits the surface normal at an angle $\theta_1 \neq 90°$ and $\theta_1 < \theta_c$, so a part of the wave is reflected (θ'_1=θ_1), and the transmitted wave is refracted, facing away from the surface normal ($\theta_2 > \theta_1$). *Light ray 3* hits the air bubble at an angle that exceeds the critical angle of total reflection, $\theta_1 > \theta_c$. The wave is completely reflected, no light is transmitted through the surface.

A dark shadow marks the periphery of the bubble, as the incident light rays are largely reflected when hitting the bubble at a big angle to the surface normal. Intensity increases toward the center of the circle due to decreasing reflection and deflection. The recorded light intensities can be transferred into data that gives quantitative information about the density fluctuations inside the test area. Furthermore, the *Schlieren imaging* is a very similar, but more sensitive technique for receiving quantitative data [34]. The exact methods and governing equations that are used for this purpose are not part of this work, since only the detection and contour of the dispersed air bubbles are of interest for the flow analysis. Due to the fact that the setup, as it is shown in Figure 3-5, is sufficient for the investigations presented combined with the ease of instrumentation, shadowgraph imaging is well suited for detecting air bubbles, their position and contour inside a liquid flow field.

4 Experimental setup

Figure 4-1 shows a picture of the experimental setup that is mounted in the laboratory. The following paragraph describes the essential components. This includes the description of the construction to generate the jet as well as the measurement equipment to analyse the liquid and the gaseous phase of the flow field.

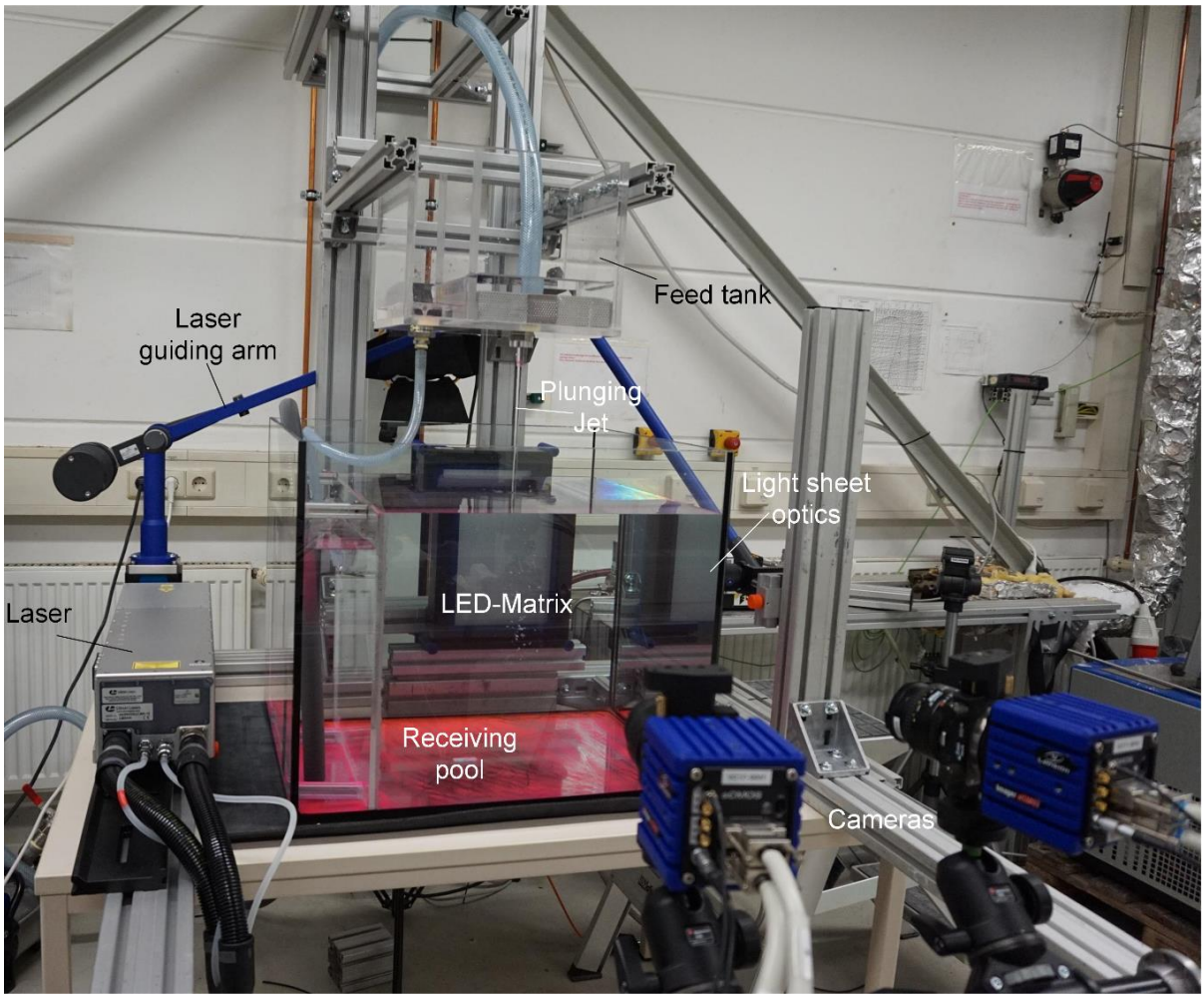

Figure 4-1: Picture of the laboratory with installed experimental apparatus

4.1 Experimental construction

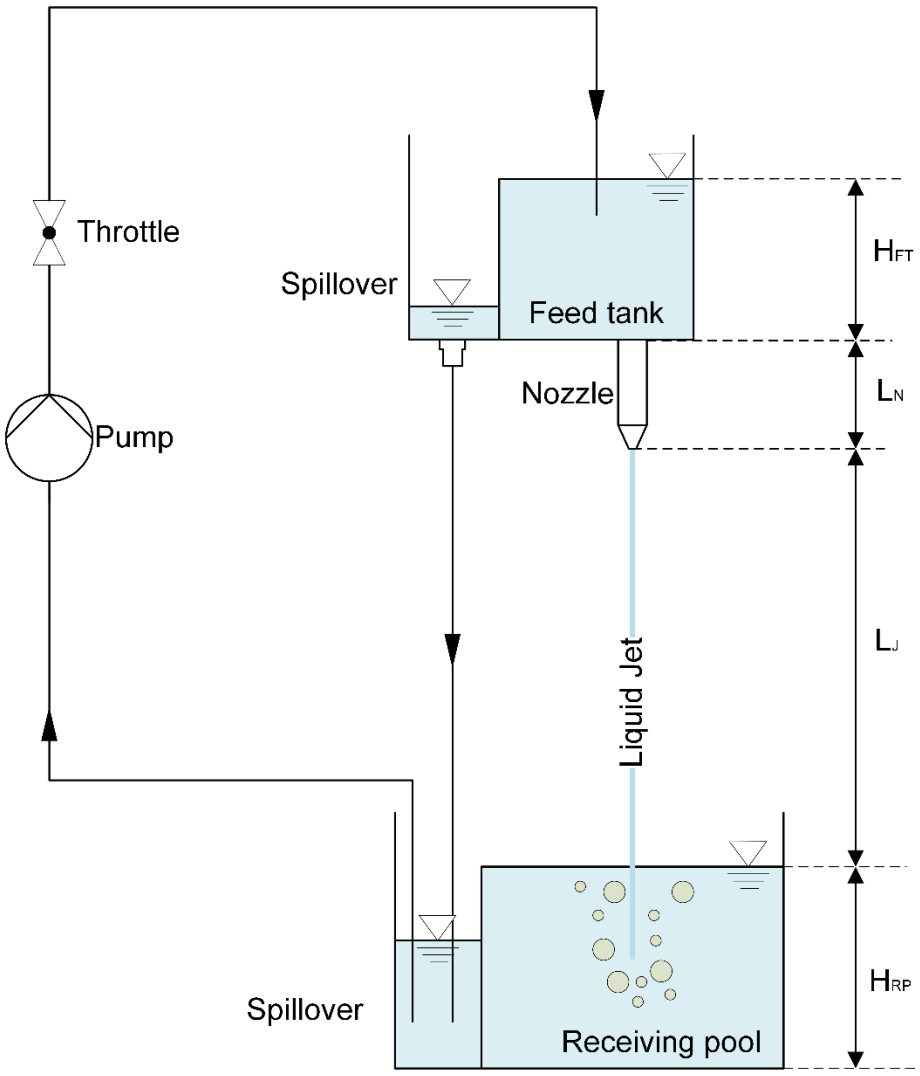

Figure 4-2: Schematic representation of experimental apparatus

Figure 4-2 exemplarily shows the assembly of the experimental setup. The investigation area is located inside the receiving pool, which is a transparent, square container filled with fully demineralised water. The liquid jet is generated by a nozzle and fed by the feed tank that sits above the receiving pool. The receiving pool as well as the feed tank is equipped with a spillover that guarantees a constant water level in both boxes. This leads to a constant length of the jet L_J and to a constant hydrostatic pressure inside the feed tank. The water that is conducted into the spillovers is led back into the feed tank by a pump. The volume flow is controlled by a throttle on the pump's discharge. It is adjusted in such a manner as to develop a minimal volume flow from the feed tank into its spillover.

Geometry receiving pool

The receiving pool has the dimensions $482\ mm, 492\ mm, 482\ mm\ (x, y, z)$. A drawing is attached in Appendix A. The water level in the pool H_{RP} is $409\ mm$. Hence, the total volume of water inside the receiving pool is $95{,}4\ l$.

Geometry feed tank

The feed tank has the dimensions $208\,mm, 235\,mm, 200\,mm\ (x, y, z)$. The water level in the tank H_{FT} is $63\,mm$. Hence, the total volume of water inside the feed tank is $2{,}62\,l$. Furthermore, the feed tank is equipped with a perforated plate that straightens the flow that is transported into the tank by the pump.

Geometry and position nozzle

The nozzle is made of transparent polymethyl methacrylate (PMMA). The nozzle has a diameter d_N of $6\,mm$ and a length L_N of $50\,mm$. The distance of the nozzle outlet to the free surface of the receiving pool and thus the length of the liquid jet L_J is $197\,mm$. The distance of the vertical axis of symmetry to the vertical walls of the receiving pool is $241{,}5\,mm, 241{,}5\,mm\ (x, z)$. A drawing of the feed tank and the installed nozzle is attached in Appendix A.

Dimensions and position field of view

The area inside the receiving pool that is investigated has the dimensions $185{,}17\,mm, 225,67\,mm\ (x, y)$. The field of view is located on a plane that intersects the axis of symmetry of the nozzle. The plane is parallel to the receiving pool's walls. The coordinate system origin is in x-direction defined by the axis of symmetry of the liquid jet and in y-direction by the water surface. Figure 4-3 shows the exact position of the camera's field of view:

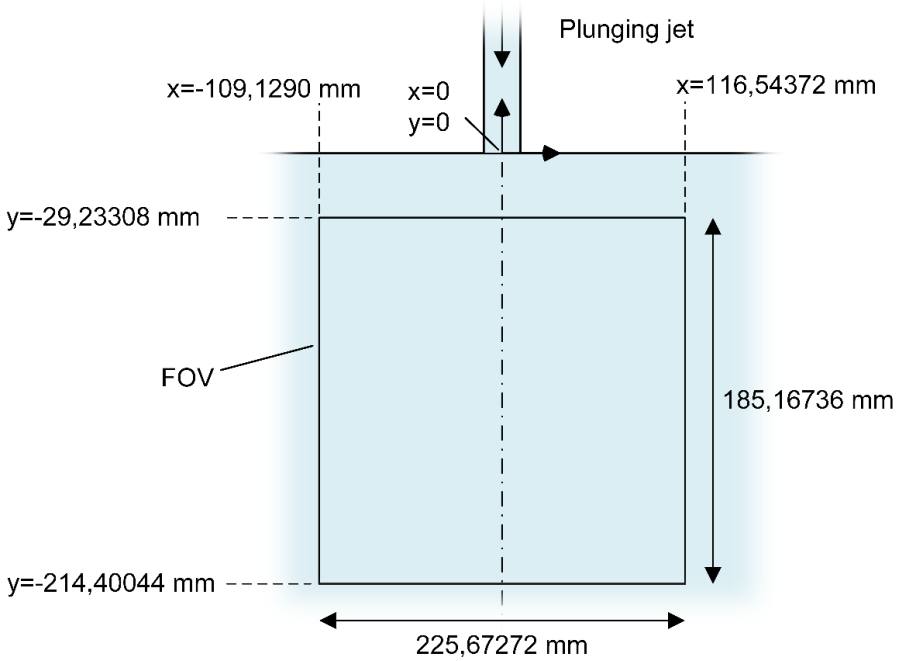

Figure 4-3: Location of field of view inside receiving pool

4.2 Particle Image Velocimetry

4.2.1 Components of the PIV setup

The components that are used for the experiment are listed.

4.2.1.1 Tracer particles

The diameter d_P of the particles that are used ranges between $40\ \mu m$ and $70\ \mu m$. Their density ρ_P is $1188\ kg/m^3$. With this data, the terminal settling velocity v_{TS} and the Stokes-number can be estimated as introduced in chapter 3.1.1.1.
As d_P is not constant but randomly varying, a minimum and a maximum value for v_{TS} exists. Additionally, fluctuations of the temperature and hence fluctuations of the liquid's viscosity inside the receiving pool contribute to a variation of the particle's terminal settling velocity.
Applying equation *3.4* yields a terminal settling velocity that ranges between a minimum of $v_{TS} = 1{,}7 * 10^{-4}$ for $d_P = 40\ \mu m, T = 22{,}1\ °C$ and a maximum of $v_{TS} = 5{,}6 * 10^{-4}$ for $d_P = 70\ \mu m, T = 24{,}1\ °C$.
Calculating the Stokes number by using the maximum diameter of the tracer particles, $d_P = 70\ \mu m$ and a characteristic length of the liquid flow $l_c = 0.06\ m$ yields $St = 0{,}075$. Hence, the assumption that the particles follow the flow congruently can be made.
To avoid parasitic optical signals to be recorded by the camera, especially reflections of the emitted laser light on the boundary surface of air bubbles, red fluorescent particles are used. They absorb the laser's light and emit light whose wavelength differs from the wavelength of the laser. By mounting an optical filter on the camera, parasitic signals are suppressed and only the desired light that is irradiated by the particles is captured.

4.2.1.2 Illumination

To illuminate the particles, a double-pulsed Nd:YAG laser is used. It emits green light with a wavelength of $532\ nm$. The pulse width is smaller than $10\ ns$, the pulse energy is $200\ mJ$. The maximum repetition rate of two consecutive pulses is $15\ Hz$. To create the required light sheet, the laser beams are guided through a light guiding arm and expanded by light sheet optics.

4.2.1.3 Camera

The used camera is based on the scientific CMOS (sCMOS) working principle. Although the architecture of the chip is the same as it is using a conventional CMOS camera, sCMOS chips offer improvements regarding a low level of noise and high frame rates. The camera is able to capture 50 double-frames per second with a resolution of $2560x2160\ pixels^2$. The dynamic range of the conversion from the analogue to the digital signal is $16\ bit$, the exposure time ranges from $0{,}015$ to $100\ ms$.
The camera is equipped with a lens that has a focal length of $50\ mm$. In addition, an optical low pass filter is mounted that has a cut-off wavelength of $540\ nm$.

4.2.2 Procedure

4.2.2.1 Calibration

To calibrate the setup, a calibration plate of the size $204x204\ mm^2$ is put into the field of view in such a manner that the plate's surface is located exactly in the light sheet. It is equipped with dots with a diameter of $3{,}2\ mm$ that have a distance of $15\ mm$ to each other. The exact dimensions are stored in the computer, so that an estimate for the third order mapping function $\widehat{\boldsymbol{F}}(\boldsymbol{x})$ is calculated. The computed function relates the coordinates on the image plane to those on the object plane with an average deviation of $0{,}337376\ pixels$.

4.2.2.2 Recording

The acquisition of the images is done by capturing the field of view in two consecutive frames. Hence, the technique of double frame/single exposure is applied. The adjustment of the time interval dt between a double frame and of the frequency of recording is discussed in chapter 4.4, as it is equally dependent on the investigation of the liquid phase as well as on the investigation of the gaseous phase.

4.2.2.3 Image evaluation

The recordings are evaluated by using the commercial software *DaVis*. The recordings are subdivided into interrogation areas of $2{,}89324\ mm,\ 2{,}89324\ mm\ (x, y)$ on the object plane. To determine the displacement of the particles that takes place between a double frame, the cross-correlation interrogation scheme is applied. Figure 4-4 shows an instantaneous vector field that is recorded by the described setup:

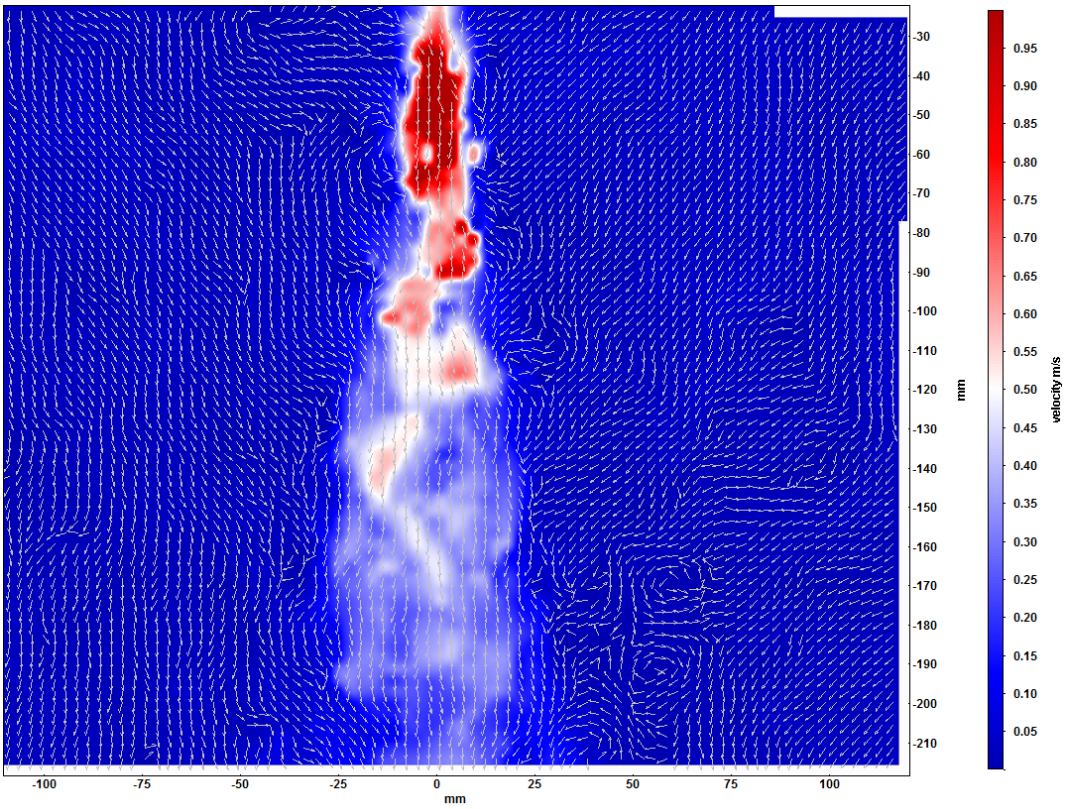

Figure 4-4: PIV measurement instantaneous velocity field

4.3 Shadowgraph imaging

4.3.1 Components of the shadowgraph imaging setup

4.3.1.1 Illumination

The illumination is realised by means of an LED-matrix that emits blue light. The wavelength is $451\,nm$, the pulse width is set to $40\,\mu s$. The matrix has dimensions that are smaller than the camera's field of view. Figure 4-5 shows the size and the location of the field that is investigated by shadowgraph imaging:

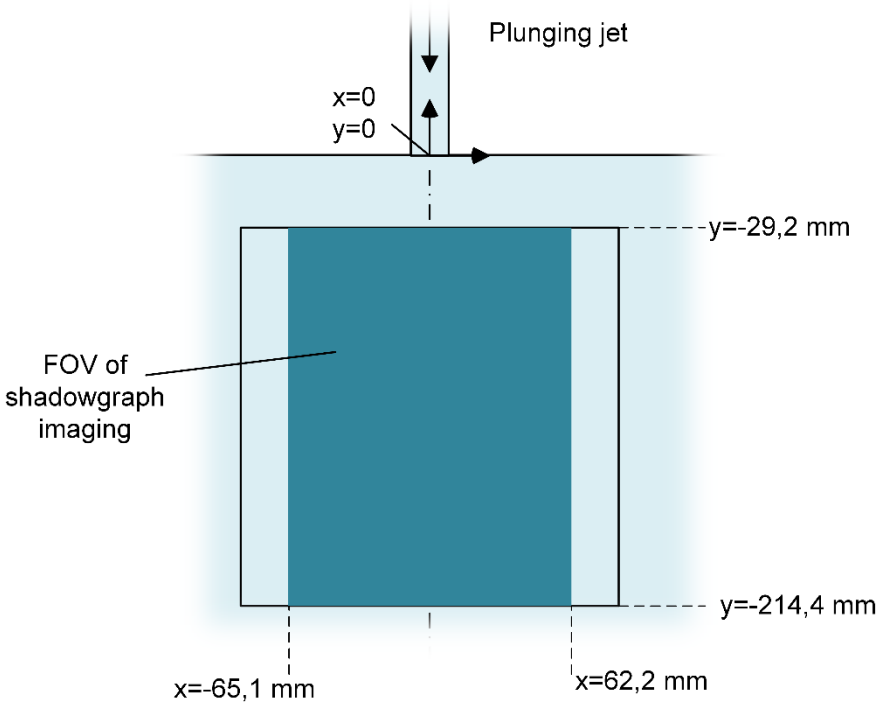

Figure 4-5: Field of view of shadowgraph imaging

4.3.1.2 Camera

The used camera is the same model as is applied for the PIV recordings. The mounted lens has a focal length of $50\,mm$. As shadowgraph imaging operates with backlight that shines throughout the whole volume of the receiving pool, the camera does record bubbles that are located outside of the plane of interest. For this reason, the lens aperture is set to the maximum value of $1/1{,}8$ to achieve a shallow depth of field for being able to focus on the laser light sheet. Bubbles that are situated behind or in front of the plane appear blurred.

On the lens, a band-pass filter is mounted that transmits light of wavelengths between $40\,nm$ and $450\,nm$. Thus, only the light of the blue LED is captured by the camera, the laser light as well as the light that is emitted by the fluorescent tracer particles is blocked by the filter.

4.3.2 Procedure

4.3.2.1 Calibration

The calibration is carried out together with the calibration of the PIV setup. As the cameras are installed in different positions relative to the calibration plate, an individual mapping function is calculated for each camera. The computed function of the shadowgraph setup relates the coordinates on the image plane to those on the object plane with an average deviation of 0,350123 pixels.

4.3.2.2 Recording

Since the recording of both measurement systems is conducted simultaneously, the principle is the same as the one of the PIV technique (double frame/single exposure).

4.3.2.3 Image evaluation

In contrast to the image evaluation algorithm of the PIV, the used software does not evaluate discrete interrogation areas but detects single bubbles by recognizing light intensities that deviate from the background intensity of the field of view. These intensity fluctuations are caused by the reflection and refraction of light rays at the boundary surface, as explained in chapter 3.2. To avoid a spurious bubble detection that is in fact an intensity deviation caused by noise, a threshold value for a minimum relative intensity difference is set. After having detected a bubble, its size is calculated by counting the number of pixels that exceed the intensity threshold.
To identify the same particle in the second double frame, the algorithm checks the plausibility of the match by reviewing the shift that takes places and the consistency of the diameter. The velocity is calculated, analogous to the PIV algorithm, by dividing the displacement by the time interval dt. The result of the shadowgraph imaging evaluation is a data sheet that lists every detected bubble, its position, diameter and velocity. Figure 4-6 shows a shadowgraph image including detected and marked bubbles:

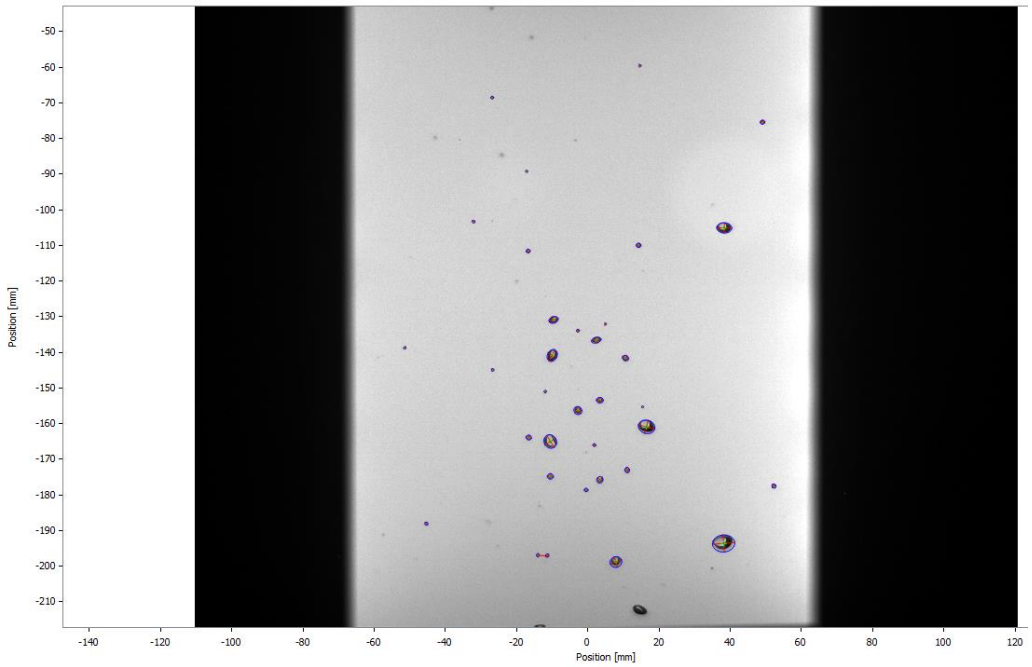

Figure 4-6: Shadowgraph image with detected and marked bubbles

4.4 Simultaneous application of PIV and shadowgraph imaging

For being able to record the gaseous phase as well as the liquid phase simultaneously, the recording parameters have to be adjusted in such a way as to guarantee the operational reliability of both measurement techniques. The main antagonism exists in the choice of the sampling frequency f and the adjustment of the time interval dt between a double frame.

In order to record an amount of data that is sufficient to form a statistically significant average, a high recording frequency is favourable in order to reduce the necessary test time. Thereby, the deviation of the external influencing variables, e.g. the ambient temperature and pressure, can be minimized. Contrariwise, a high frequency leads to a repetitive detection of a large quantity of air bubbles, as their hydraulic residence time inside the liquid pool is longer than the shortest time difference between two double frames. After having conducted numerous test recordings, the defined frequency that represents a suitable compromise is $1\ Hz$.

The algorithm for the velocity calculation of PIV and shadowgraph imaging is based on the measurement of a displacement during the known time interval dt. Indeed, the significant differences between both techniques are the size and the shape of the objects whose displacement is recorded. The used particles for the PIV have a consistent profile and a maximum diameter of $70\ \mu m$, whereas the air bubbles exhibit diameters up to several millimetres in combination with a partially deformed shape. These different structural conditions lead to different ranges of displacements that are feasible to be utilized by the respective algorithms. For the present experiment, a time interval dt of $1000\ \mu s$ yields reasonable results for both measurement techniques. Both illustrations in chapter 4.2 and chapter 4.3 are recorded with these settings.

5 Measurement program

The aim of this work is to analyse the phenomena of a liquid plunging jet. Therefore, not only the characteristics of the flow itself, but also all the variables that have an influence on the fluid's behaviour are examined. This paragraph introduces the design of experiments. It is divided in three parts: The first one deals with the recording of all conditions that have an influence on the experiment. The second one describes the approach to investigate the temporal flow behaviour. The third part is the actual, spatial investigation of the flow field.

5.1 Boundary conditions

Temperature water
The temperature of the water is recorded by means of a thermocouple. As the regulation of the inflow into the tank is realized by a throttle at the pump's discharge, the water is heated.

Density water
The density of the liquid water in dependency of temperature and pressure is provided by literature [22]. The presence of the dispersed tracer particles is neglected, as the volumetric ratio of particles to water is $0{,}038\ ‰$.

Temperature ambient air
The temperature of the ambient air is measured with a thermocouple.

Pressure ambient air
A measuring mast on the research facility provides data about the ambient pressure at a height of two meters above the ground.

Volumetric flow rate water
The volumetric flow rate is measured by collecting the water that exits the nozzle in a container for 90 seconds. Weighing the mass of the water and dividing it by its density and the time yields the volumetric flow rate of the installed setup. To minimize the uncertainty of the measurement, the procedure is conducted four times and an average is formed.

Turbulence level of liquid jet
Due to the round and uneven surface of the liquid jet and the refraction and reflection of the laser light sheet at the water/air boundary, an investigation by means of PIV does not provide results that represent the real state of flow.
But having a significant influence on the behaviour of the liquid jet and hence on the air entrainment mechanisms, the turbulence level of the liquid jet is a value of major interest. For that reason, an investigation of the flow inside the tank is planned that gives information about the inflow into the nozzle. The measurements are conducted with the same PIV setup that is used for the investigation of the flow field inside the pool.

Figure 5-1 shows the position of the area the inflow is investigated:

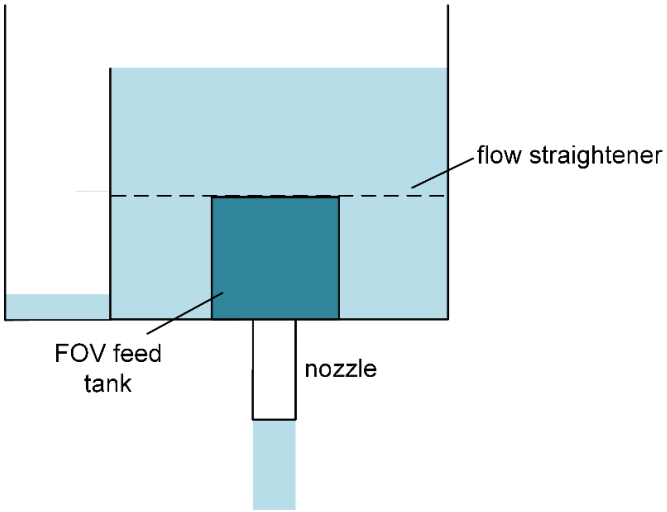

Figure 5-1: Field of view for PIV recordings inside feed tank

Surface tension water
The surface tension of the liquid water in dependency of temperature and pressure is provided by literature [44].

Viscosity water
The viscosity of the liquid water in dependency of temperature and pressure is provided by literature *[23].*

Electrical conductivity water
As pure water is not conductive, identifying the conductivity of the water gives a possibility to characterise the level of contamination.

5.2 Temporal flow behaviour

As the observed flow regime is a turbulent one, the objective is to guarantee that the measuring results do not only picture instantaneous phenomena but represent an average flow that is statistically significant. In addition, the experiment is conducted a second time. By maintaining all the influencing variables, a comparative measurement is thereby created that serves as possibility to ensure the reproducibility of the experiment.

5.2.1 Qualitative observations

Time-lapse
To make a first statement about the general characteristics of the dispersed bubbles and the order of the time scale of present flow states, a video with a framerate of 24 frames per second is generated out of pictures that are recorded with a frequency of $0{,}5\ Hz$. Hence, the 3 minute video shows the behaviour of the system that equals a time span of 2,5 hours in reality.

High speed imaging
By means of a high speed camera, the sector of the impingement of the jet into the water pool is examined. Thereby, information about the jet's structure as well as information about the dominant air entrainment mechanisms can be gained.

5.2.2 Liquid phase

The liquid flow is investigated by PIV to identify the measurement time that is necessary to collect an amount of data that represents the experiment in its time average. To comply with this requirement, test series are conducted. The series consist of particular sequences. Every sequence again is composed of a quantity of PIV measurements. Figure 5-2 shows the principle. For the purpose of clarity, the following illustrations are limited to one interrogation area exclusively.

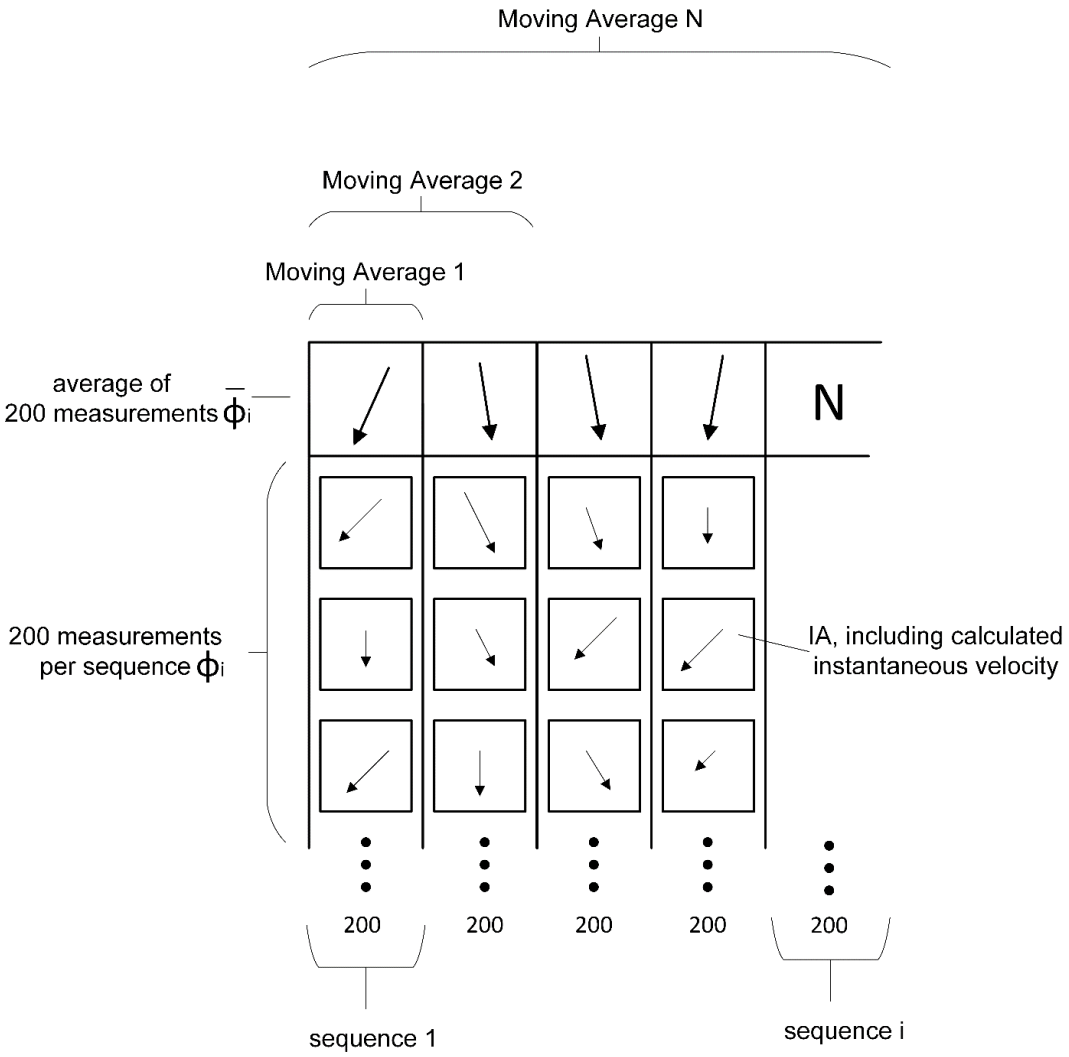

Figure 5-2: Moving average of measurement sequences

Every sequence of measurements consists of 200 separate PIV measurements. These 200 measurements are averaged. By repeating this procedure N times, a moving average MA_N can be calculated by applying the following formula:

$$MA_N = \frac{1}{N}\sum_{i=1}^{N}\overline{\phi_i} \qquad 5.1$$

where $\overline{\phi_i}$ is the average of the measured variable. Figure 5-3 demonstrates the principle of this statistical evaluation:

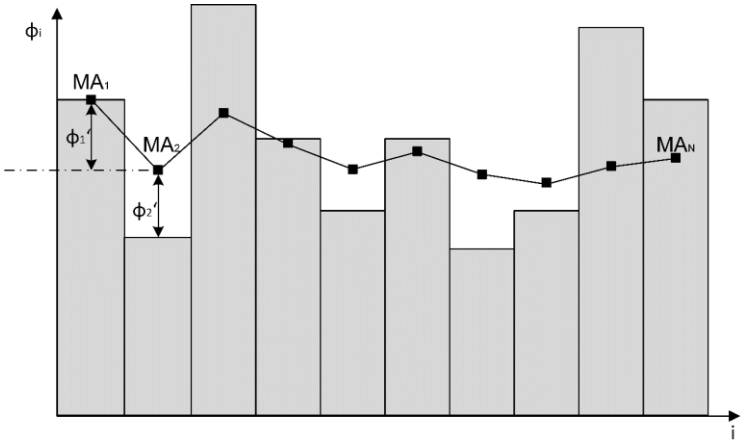

Figure 5-3: Scheme of moving average and standard deviation of measurement sequences

The grey columns represent the averaged magnitude of a particular measurement sequence. Although these values represent an *average* of a statistical population – of 200 instantaneous values of the flow – they are handled as individual magnitudes ϕ_i that are part of a new statistical population, which is the entirety of measurement sequences.
In addition to the moving average MA_N, the standard deviation s_N is formed in order to quantify the mean spreading of the instantaneous values ϕ_i around the moving average MA_N:

$$s_N = \sqrt{\frac{\sum_{i=1}^{N}(\phi_i - MA_N)^2}{(N-1)}} = \sqrt{\frac{\sum_{i=1}^{N}(\phi_i')^2}{(N-1)}}$$

By examining s_N and MA_N, steady-state conditions for the liquid flow can be formulated that serve as indicators for the amount and the time span of recordings that are necessary to ensure statistical significance as well as reproducibility of the measurements. The variable of the flow that is used to perform the analysis of the temporal behaviour is the absolute value of the velocity vector $|\overline{\boldsymbol{u}}| = \sqrt{\bar{u}_x{}^2 + \bar{u}_y{}^2}$. The claimed requirements are:

- Converging character of moving average and standard deviation. Magnitude of relative change of absolute velocity $|\overline{\boldsymbol{u}}|$ from MA_{N-1} to MA_N not greater than 1 % to ensure statistical significance
- Relative change of measured absolute velocity $|\overline{\boldsymbol{u}}|$ not greater than 10 % when repeating the experiment under the same conditions to ensure reproducibility

Two vertical axes are chosen to perform the evaluation. One of them is situated close to the symmetry axis of the nozzle to investigate areas of high velocities, the other one is situated outside the symmetry axis where lower velocities are expected. The evaluation of the statistical significance is made for six interrogation areas that are located on the axes. To evaluate the reproducibility of the experiment, the trend of the absolute velocity $|\overline{\boldsymbol{u}}|$ in dependency of the y-coordinates is analysed and compared to the trends of the corresponding comparative measurement. Figure 5-4 shows a sketch of the locations:

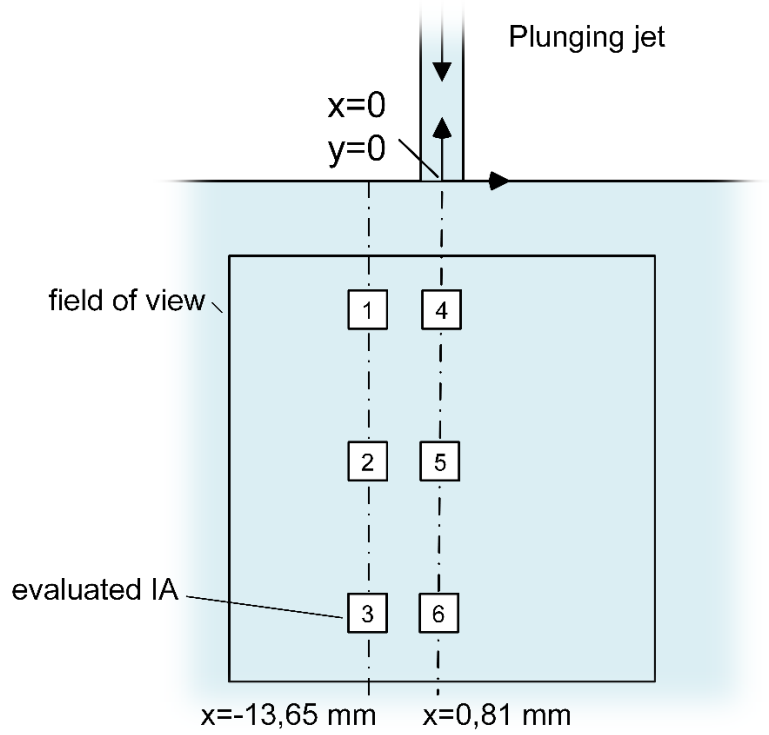

Figure 5-4: Location of interrogation areas to analyse temporal behaviour of liquid flow

IA	x [mm]	y [mm]
1	-13,65208	-40,80604
2	-13,65208	-92,88436
3	-13,65208	-194,14776
4	0,81412	-40,80604
5	0,81412	-92,88436
6	0,81412	-194,14776

Table 1: Location of interrogation areas to analyse temporal behaviour of liquid flow

As the chosen time interval $dt = 1000\ \mu s$ is not an ideal value for the PIV measurements but rather a reasonable compromise for being able to record the movement of the liquid and the gaseous phase at the same time, the time interval of the comparative measurement is shortened. Since the comparative measurement serves as a validation of the liquid flow field, there is no need to compute the movement of the gaseous phase. Hence, the time interval is set to $dt = 350\ \mu s$, which is a suitable value to investigate the liquid flow field properly.

5.2.3 Gaseous phase

Analogous to the analysis of the liquid phase, the measurements of the gaseous phase are separated into sequences that consist of 200 instantaneous recordings. For every sequence, a separate histogram of the bubble size distribution is created to compare the amount and the characteristics of the dispersed air bubbles. To define a criterion for the statistical significance, the count of detected air bubbles cnt within one sequence is used. Again, a moving average is formed. The claimed requirement is:

- Converging character of moving average. Magnitude of relative change of count of bubbles cnt from MA_{N-1} to MA_N not greater than 1 %

Additionally, the bubble size distribution is compared to the one of the comparative measurement.

5.3 Spatial behaviour of the averaged flow field

After having ascertained the statistically significant character of the entirety of measurements, the whole field of view of the PIV and shadowgraph recordings is examined and analysed.

5.3.1 Liquid phase

Mean velocity
The trend of the mean velocities $\bar{u}_x$, $\bar{u}_y$ and $|\overline{\boldsymbol{u}}|$ in dependency of their position relative to the water surface and the centerline of the plunging jet are illustrated. Furthermore, the gradient of the mean velocity $\bar{u}_y$ in y-direction is plotted.

Root-mean-square of velocity fluctuations
The *rms*-values $u_{x,rms}$, $u_{y,rms}$ and $|\overline{\boldsymbol{u}}|_{rms}$ are presented. In combination with the mean velocities, Reynolds-stresses and turbulence levels of the flow can be calculated.

Reynolds stresses
The density-specific Reynolds stresses ${\tau_{xy}}^R$, ${\tau_{xx}}^R$ and ${\tau_{yy}}^R$ are plotted. They are calculated by using the *rms*-values of the correspondent directions.

Turbulent kinetic energy
As the investigation of the liquid flow is limited to two dimensions, the component in z-direction must be estimated.

5.3.2 Gaseous phase

Velocity and diameter of bubbles in dependency of their location

Unlike the PIV recordings, the shadowgraph pictures are not divided into discrete interrogation areas. Hence, the field of view is vertically divided into sections of $5\,mm$ width for being able to visualize the characteristics of the bubble velocities and diameter in dependency of their vertical and horizontal position in two-dimensional diagrams. The trend of bubble diameter and velocity is examined. Figure 5-5 illustrates the fragmentation:

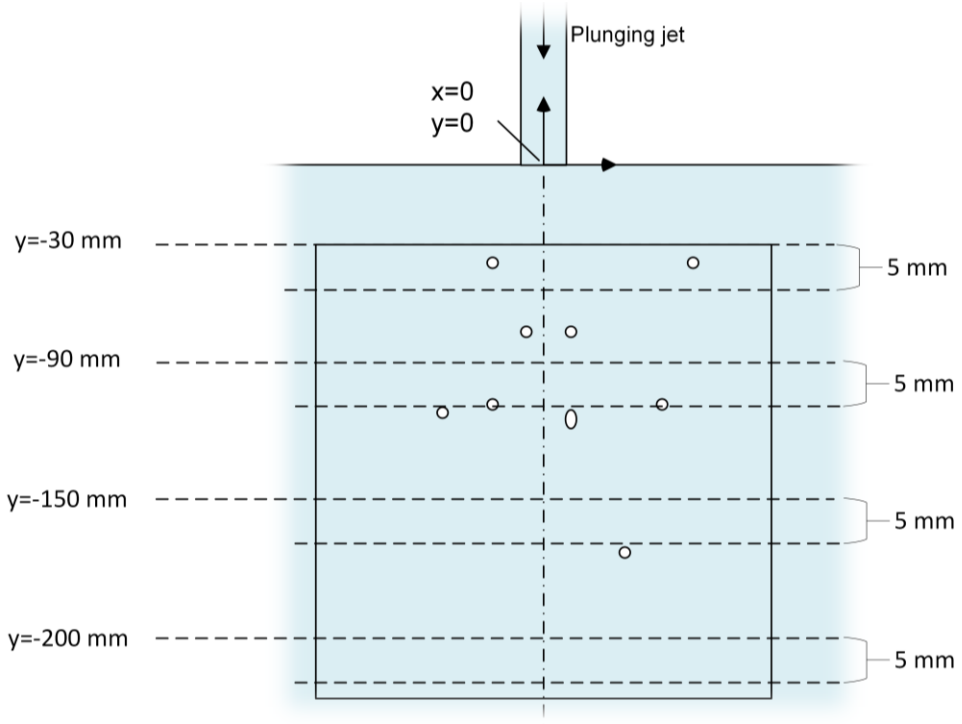

Figure 5-5: Fragmentation of field of view to analyse bubble velocity in dependency of y-position

6 Experimental results

6.1 Boundary conditions

Temperature water
Figure 6-1 shows the increase of the temperature inside the receiving pool in dependency of the time the system is running:

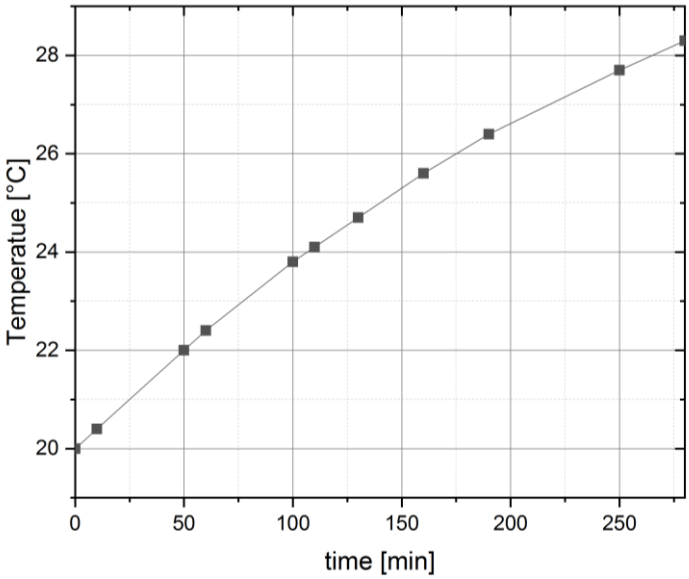

Figure 6-1: Trend of temperature inside receiving pool

The experiment is started after a 50 minute running-in time of the pump. The measurements are taken during a time span of 60 minutes. Hence, the temperature increases from $22\,°C$ to $24{,}1\,°C$.

Density water
According to [22], the density of the water ranges from $997{,}295\ kg/m^3$ at $22\,°C$ to $997{,}2748\ kg/m^3$ at $24{,}1\,°C$.

Temperature ambient air
The measured temperature of the ambient air is $21{,}9$ °C.

Pressure ambient air
The measured pressure of the ambient air is $1007\ hPa$.

Volumetric flow rate water

The results of the measurements are presented in Figure 6-2. The averaged volumetric flow rate is $0{,}049804\ l/s$.

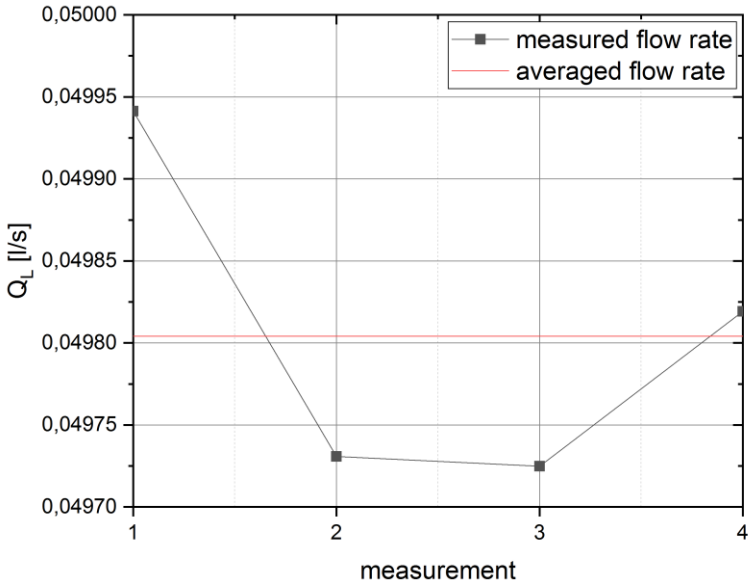

Figure 6-2: Volumetric water flow rate

Flow velocity at nozzle inlet

Figure 6-3 shows a vector plot of the present liquid flow field before the water enters the nozzle inlet:

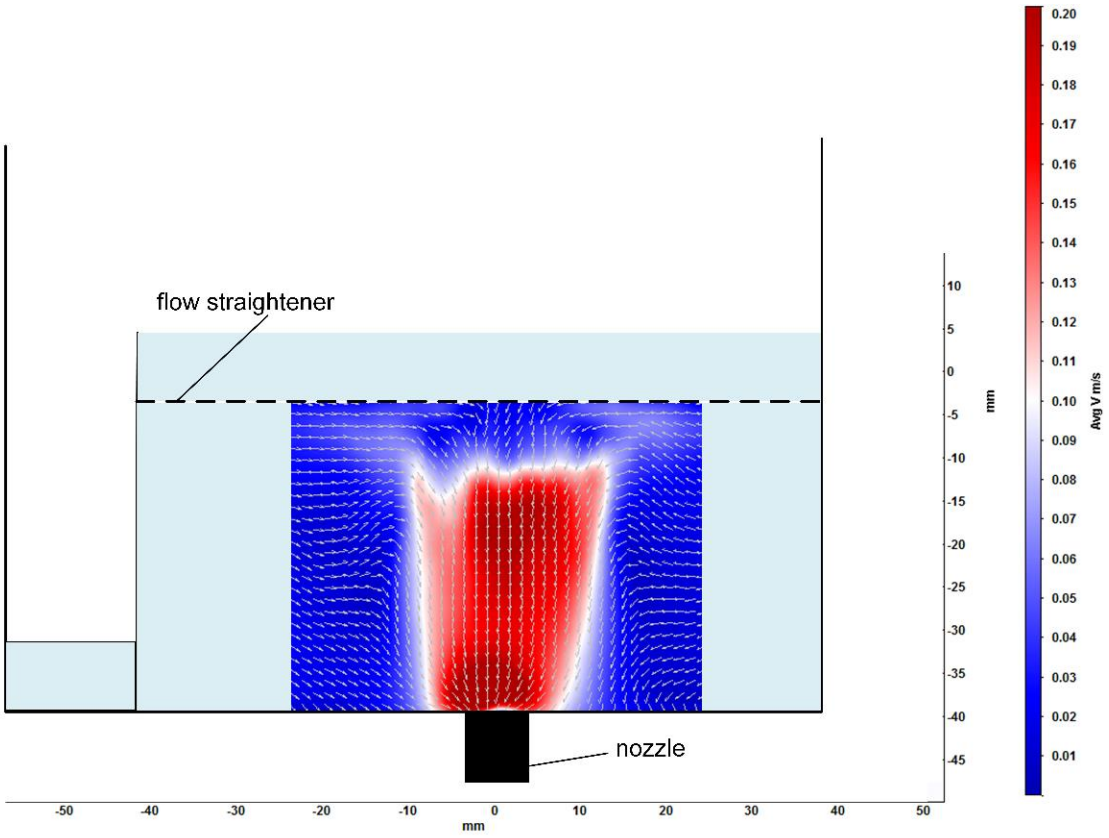

Figure 6-3: Flow field at inside feed tank

Figure 6-3 represents the absolute fluid velocity $|\overline{\boldsymbol{u}}|$. The length and the colour of the vector arrows do not carry information, they only represent the direction of the moving fluid. The colour of the background illustrates the velocity of the fluid.
To make a rough estimate of the level of turbulence at the nozzle inlet, Figure 6-4 shows the velocity $\bar{u}_x$ and its *rms*-value in x direction, as well as the vertical component $\bar{u}_y$ and $u_{y,rms}$:

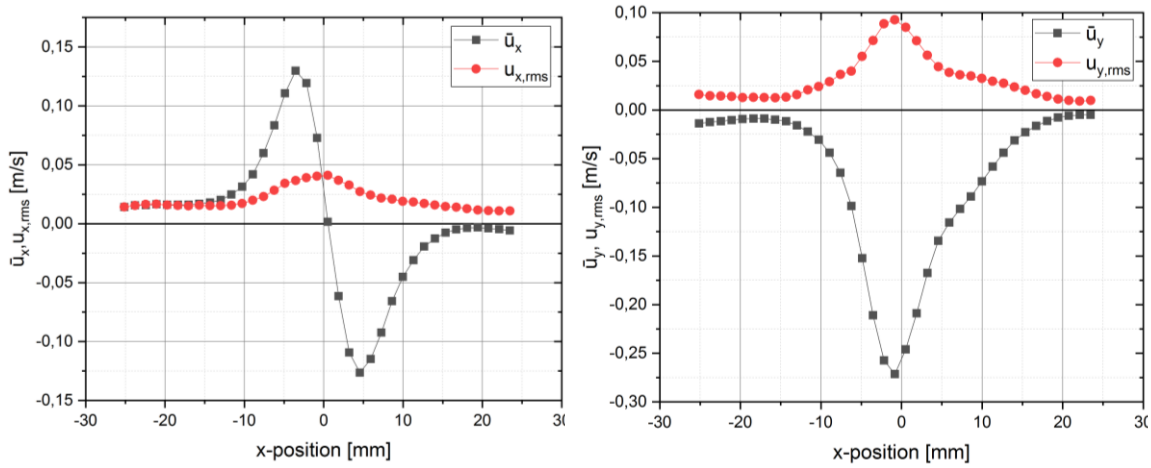

Figure 6-4: Diagrams of fluid velocity in x and y direction directly before nozzle inlet, y=-37 mm

Although the maximum *rms*-value of u_x has its maximum on the symmetry axis of the nozzle, the averaged velocity in x-direction vanishes at the same position. Adjacent to the axis, the flow is sucked towards the nozzle and has therefore a velocity in x-direction. Simultaneously, $u_{x,rms}$ decreases while moving away from the axis of symmetry. The maximum magnitude of $\bar{u}_y$ is found on the symmetry axis, as well as the maximum magnitude of $u_{y,rms}$.
Looking at these trends and at the maximum velocities of the fluid, it has to be emphasized that the measurement is not conducted directly at the nozzle inlet but some millimetres away from it. As the particles that enter the nozzle disappear from the camera's field of view, it is not possible to record its displacement by the algorithm.

Surface tension water
According to [44], the surface tension γ_W of the water ranges from $72{,}44 * 10^{-3}\ N/m$ at $22\ °C$ to $72{,}11 * 10^{-3}\ N/m$ at $24{,}1\ °C$.

Viscosity water
According to [23], the dynamic viscosity μ_W of the water ranges from $953{,}2 * 10^{-6}\ Pa * s$ at $22\ °C$ to $907{,}5 * 10^{-6}\ Pa * s$ at $24{,}1\ °C$.

Electrical conductivity water
The measured conductivity of the water is $1{,}76 * 10^{-4}\ S/m$.

6.2 Temporal flow behaviour

6.2.1 Qualitative observations

Time-lapse

Analysing the time-lapse video, a fluctuation of the maximum entrainment depth of the entrained air bubbles is observed. The lower limit of the bubble swarm oscillates in a time scale that has a magnitude of several minutes. The total amount of dispersed bubbles and the density of the bubble plume varies as well. Figure 6-5 shows three samples that are extracted from the time-lapse video:

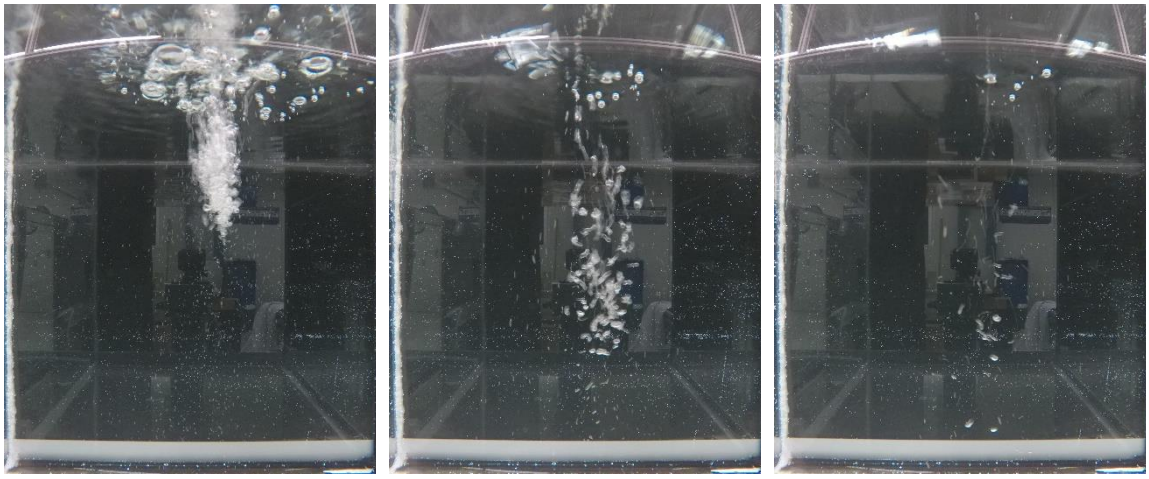

Figure 6-5: Variation of density and penetration depth of air bubble plume

The picture on the left indicates a dense bubble plume combined with a shallow penetration depth. On the free surface, concentric waves around the impingement point can be observed. The bubble plume that is shown in the central picture is less dense and entrains deeper into the receiving pool. Still, a rough character of the free surface is visible. The right sample presents a situation that does not exhibit a plume of bubbles, but rather a small amount of entrained air that is dispersed in the whole bath. On the surface, no waves are detectable.

Based on this first qualitative observation of the flow characteristics, the estimation is made that a measurement time of approximately 60 minutes is necessary to capture the intermitting behaviour of the system.

High speed imaging

The following picture shows a frame that is extracted of the high speed video. The shown scale serves as an estimation of the physical dimensions.

Figure 6-6: Frame of high speed video

The surface of the jet is not smooth, but rather rippled. Contractions of the diameter are visible as well as bulges. The transport of the irregularities downstream causes in some cases an air entrainment into the liquid pool. The shown picture captures such an event: On the right side of the jet, directly after impinging on the free surface, the formation of a bubble is observed. The structure of the jet surface and the absence of a clearly identifiable meniscus on the water surface leads to the conclusion that the jet can be assigned to be part of the group that is described as *transitional (type 2,* see chapter 2.9). Hence, the air is entrained due to the transport inside the boundary layer of the jet, as well as due to the downstream transported disturbances.

6.2.2 Liquid phase

Statistical significance

As the qualitative observations show an intermitting behaviour of the flow with a time scale of several minutes, the recording time is set to 60 min. This equals 18 measurement sequences, each consisting of 200 calculations of the instantaneous velocity field. The interrogation areas that are shown in Figure 5-4 are evaluated to check if the claimed requirements for statistical significance are fulfilled. As the trend of the analysis of all six investigated interrogation areas is similar, this paragraph presents the evaluation of IA 1 only. The entire extent of measurements can be reviewed in Appendix (Temporal behaviour IA 2-6)

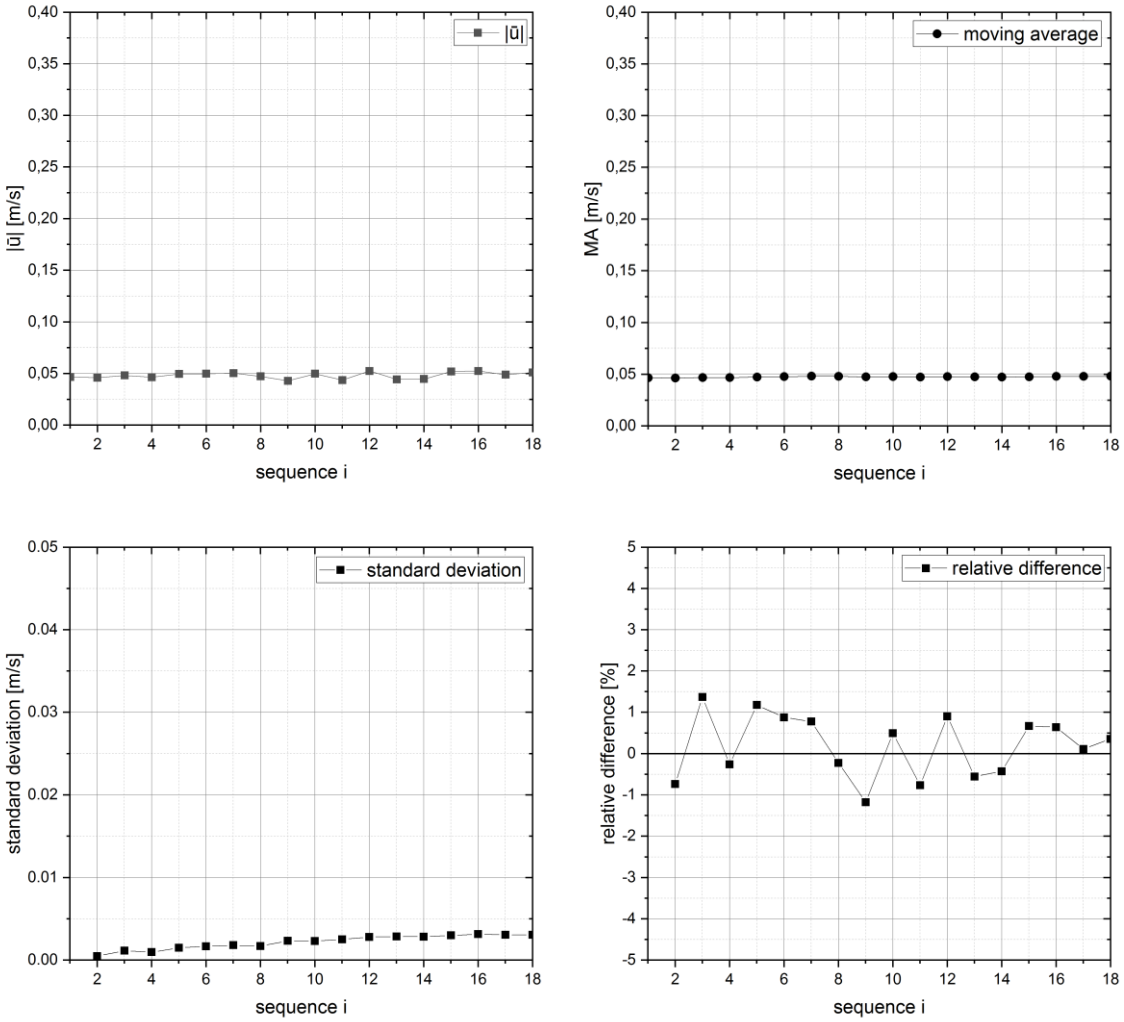

Figure 6-7: Temporal evaluation of interrogation area 1

The trends of the moving average of the absolute fluid velocity $|\overline{\boldsymbol{u}}|$ as well as the trend of the standard deviation are converging. After 18 measurement sequences, the magnitude of the relative velocity difference from MA_{17} to MA_{18} is smaller than $0{,}5\ \%$ in each area that is investigated. Hence, the averaged flow field that is formed out of 3600 instantaneous recordings over a timeperiod of 60 minutes can be stated as statistically significant. This applies to areas of low velocities in the same way as for areas of high velocities.

Reproducibility

As the statistical significance of the experimental analysis is proved, the results of the comparative measurement are expected to be congruent with those of the actual measurement. Figure 6-8 shows the result of the evaluation of the absolute fluid velocity $|\overline{\boldsymbol{u}}|$ along the vertical axis with the position $x = -13{,}65\ mm$. The black dots mark the values of the actual measurement, the red ones represent the values of the comparative measurement.

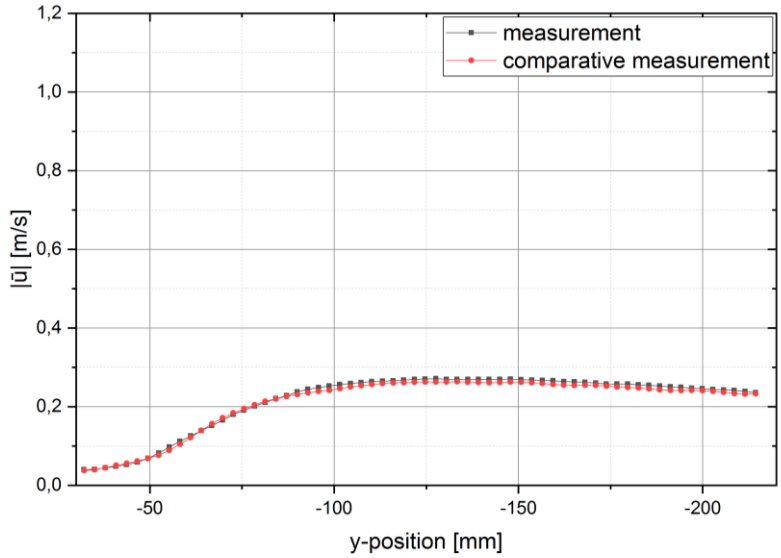

Figure 6-8: Evaluation of reproducibility of PIV measurements, x-position=-13,65 mm

The measurements of the low velocity region show a good congruence. The averaged magnitude of relative differences is $3{,}21\ \%$, the maximum relative difference is $8{,}6\ \%$.

Figure 6-9 shows the result of the evaluation of the absolute fluid velocity $|\overline{\boldsymbol{u}}|$ along the vertical axis with the position $x = 0{,}81\ mm$.

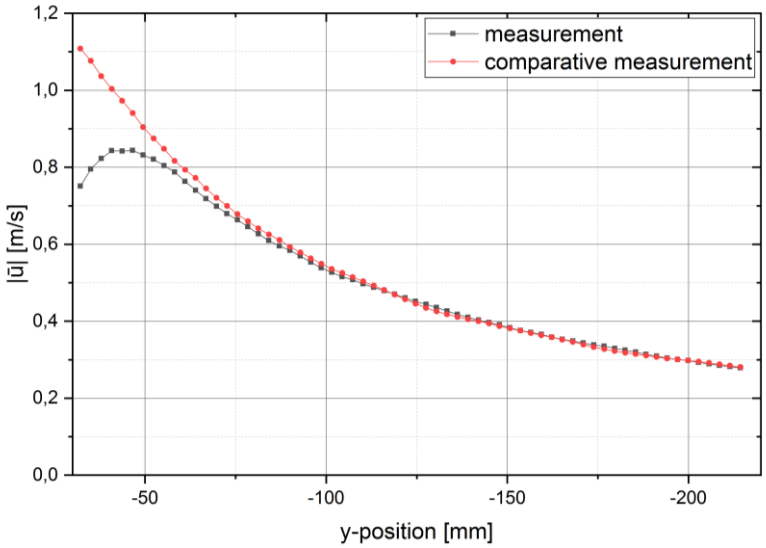

Figure 6-9: Evaluation of reproducibility of PIV measurements, x-position=0,81 mm

At low velocities, both trends agree with each other. Evidently, the higher the velocity, the more the trends deviate. The explanatory statement is that the PIV setup is not able to estimate the velocity correctly. The velocity is computed by calculating an average displacement of local groups of particles for every interrogation area. In regions of high velocities and high levels of turbulence, the chosen time difference $dt = 1000\ \mu s$ causes the illuminated particles to cover a distance that exceeds the range that is detectable by the algorithm. Furthermore, high velocities in z-direction lead to the particle's escape out of the illuminated light sheet. These fast particles yield a miscalculation of the local fluid velocity, since only the slower particles are observable in both associated double frames the calculation is based on. The higher the fluid's velocity, the more the measurement error increases. In contrast, the comparative measurement that is conducted with a time interval of $350\ \mu s$ between two PIV double-frames shows a trend of the velocity that conforms to the common behaviour of plunging liquid jets (see [20, 30, 37, 47]).
The proof of the statistically significant character of the averaged flow field enables the feasibility of replacing the defective velocity calculations by the correspondent values of the comparative measurement. For this reason, the spatial investigation of the liquid flow is based on a composite matrix of vectors. Figure 6-10 illustrates the composition: The red framed zone represents the area inside the field of view in which the values are replaced by those of the comparative measurement.

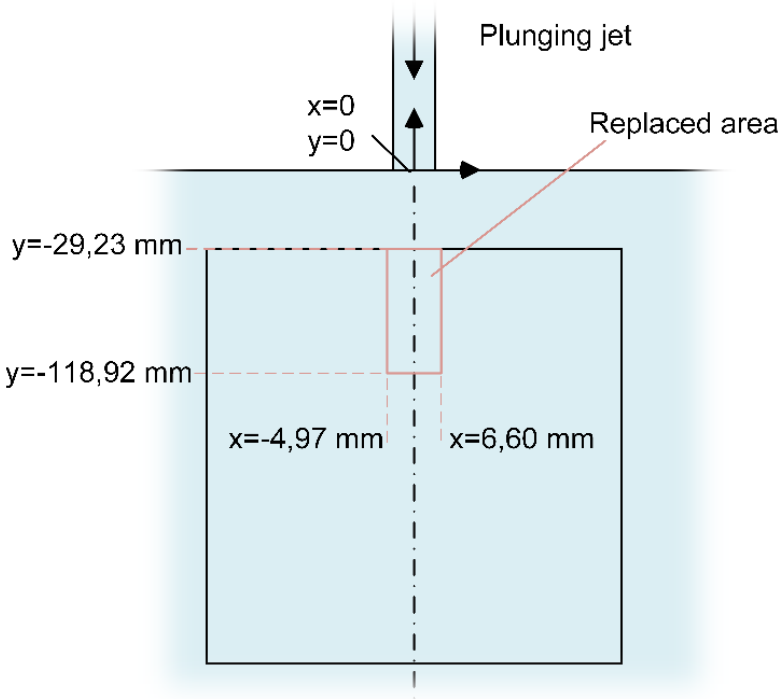

Figure 6-10: Composition of field of view with area that is replaced by measurements made with dt=350 µs

6.2.3 Gaseous phase

Statistical significance

The measurement of the gaseous phase by shadowgraph imaging confirms the strong fluctuations of bubble counts. Figure 6-11 shows a graph that presents the counts of bubbles per image. As the imaging frequency $f = 1\ Hz$, the image number equals the recording time.

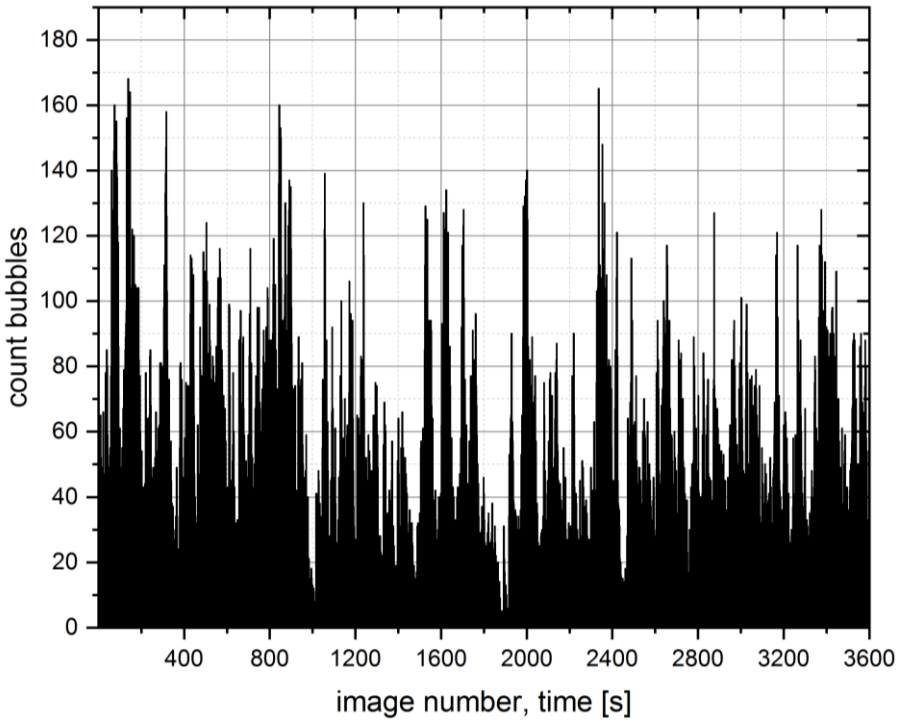

Figure 6-11: Bubble counts per image

It is evident that - similar to the turbulent character of the liquid flow – a measurement time of several minutes has to be chosen. Figure 6-12 shows the analysis of the temporal behaviour of bubble counts that is divided into 18 sequences, identically to the evaluation of the temporal behaviour of the liquid flow field.

The maximum count of detected bubbles per sequence is 14789 in sequence 1, the minimum is 5921 in sequence 10. Forming an average over all 18 sequences yields a mean bubble count of 9626 with a standard deviation of 2163 bubbles. The temporal behaviour of the averaging exhibits a convergent character, both regarding the moving average and the standard deviation. The relative difference of detected bubbles from MA_{17} to MA_{18} is 0,48 % and accordingly smaller than the required threshold magnitude of 1 %. Consequently, the chosen measurement time of 60 minutes is adequately long for representing a statistically significant average, both concerning the liquid and the gaseous flow field.

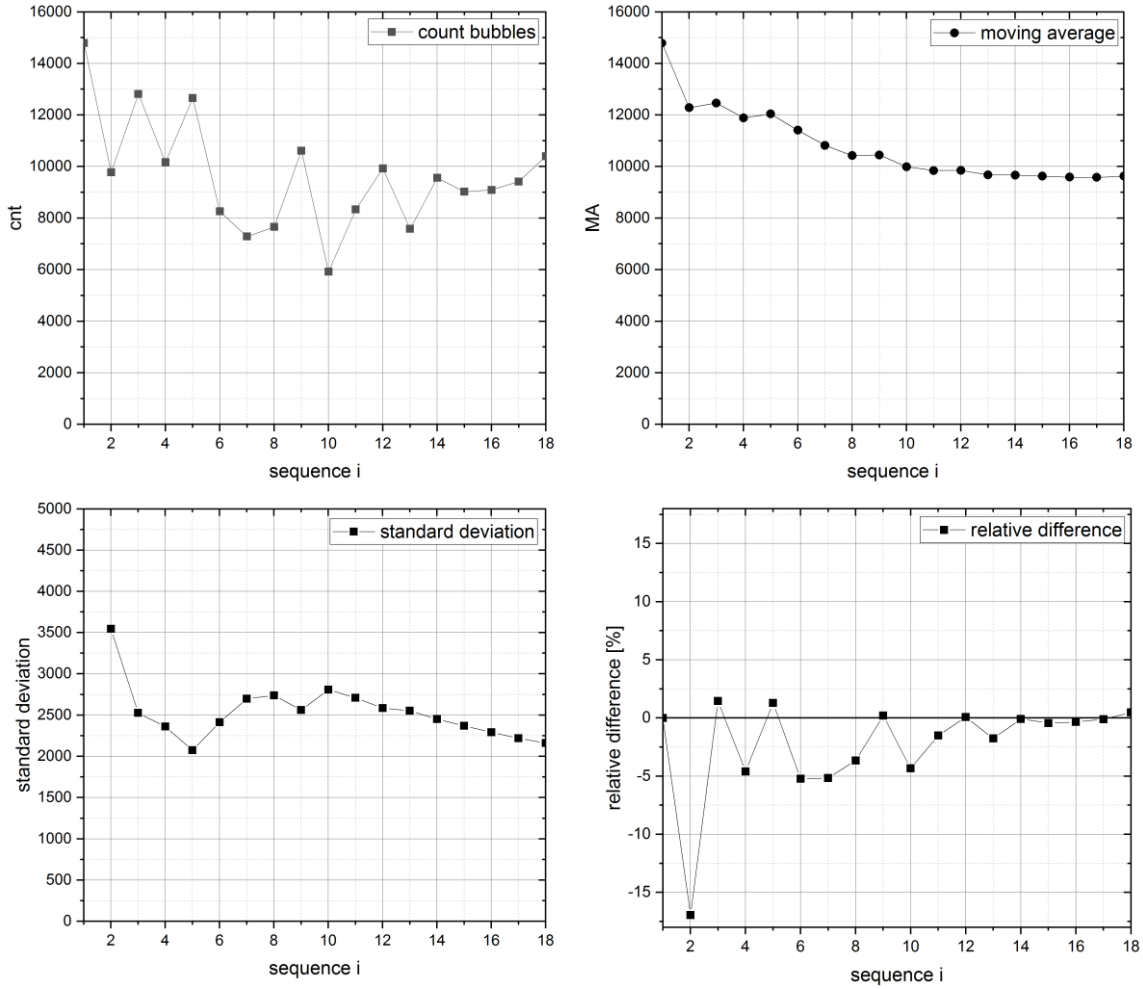

Figure 6-12: Temporal evaluation of bubble counts

Beyond the study of the bubble counts per sequence, Figure 6-13 shows the normalized distribution of bubble sizes for every single sequence:

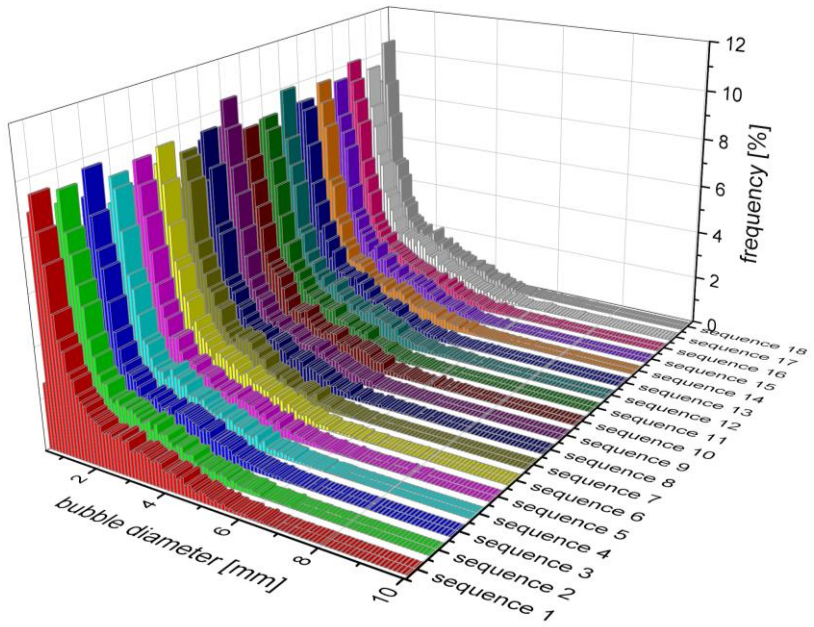

Figure 6-13: Normalized histograms of bubble size for particular sequences

Although the character of air entrainment is highly alternating concerning the count of dispersed bubbles and their position inside the receiving pool, the graphic shows a strong conformity of the normalized bubble size throughout the individual recording sequences. Despite the total counts of bubbles, the most frequent detected bubble size is $0{,}7\ mm$, in each of the sequences.

Reproducibility

Figure 6-14 shows a comparison between the histograms of the complete measurement and the comparative measurement:

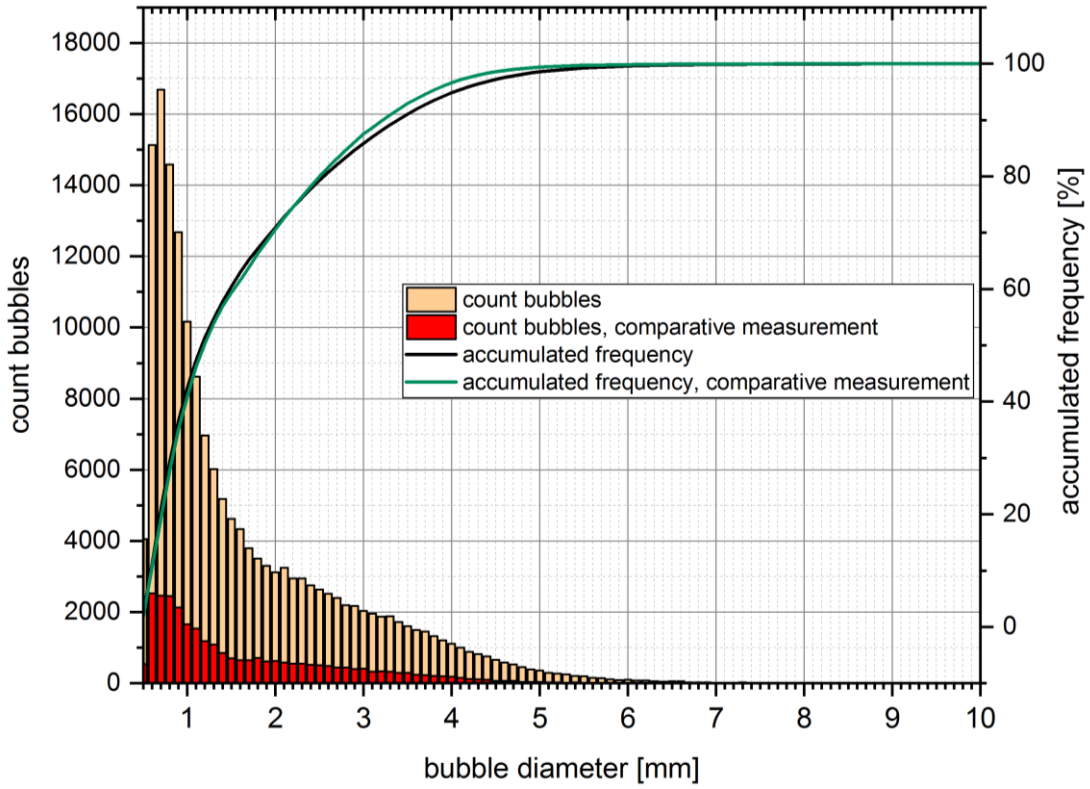

Figure 6-14: Histogram and accumulated frequency of measurement and comparative measurement

In contrast to the analysis of the liquid flow field that showed coincident trends of the fluid velocities, the comparative measurement exhibits completely different characteristics. The count of total detected bubbles deviates by a factor of 6 (173125 counts in measurement, 28890 counts in comparative measurement). Hence, a guarantee for the reproducibility of the total amount of dispersed air bubbles is not given by repeating the experiment under identical conditions. However, the accumulated frequency of the bubble diameter shows a coinciding tendency in both experiments, which proves a similar character of the normalized bubble distribution not only comparing particular sequences within one test series, but an accordance regarding two independently conducted measurements that have the same boundary conditions.

6.3 Spatial behaviour of the averaged flow field

6.3.1 Liquid phase

Mean velocities $\bar{u}_x$, $\bar{u}_y$ and $|\overline{\boldsymbol{u}}|$

Figure 6-15 shows a vector plot of $|\overline{\boldsymbol{u}}|$:

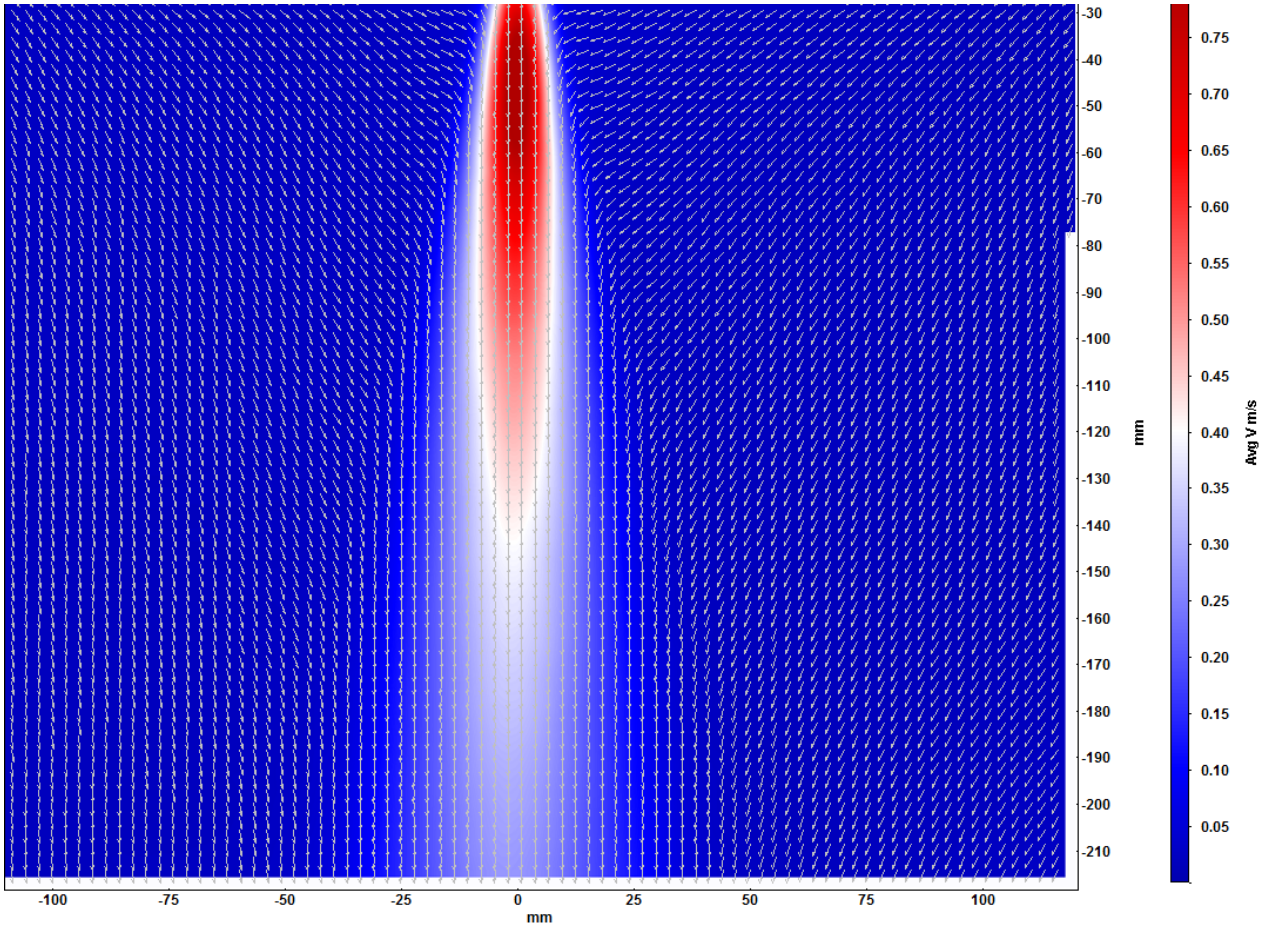

Figure 6-15: Vector plot of averaged absolute velocity field

The arrows describe only the direction of the flow and not the magnitude of the velocity, as they all have a fixed length. Information about the flow velocity can be extracted out of the colour of the background.

In contrast to the asymmetrical vector plot of the instantaneous velocity field (Figure 4-4), the averaged velocity field exhibits a uniformly distributed and symmetric behaviour. The symmetry axis of the jet represents the symmetry axis of the evolved flow field inside the receiving pool. The maximum velocities are lower than those that are observed in the instantaneous flow field.

Due to the running-in time of 50 minutes and the measurement time of 60 minutes, the liquid inside the whole receiving pool is in motion. As the water volume constantly remains the same, the liquid that is transported downstream must rise again towards the free surface in order to be transported towards the bottom of the pool. In this way, a recirculation zone adjacent to the jet develops.

Figure 6-16 illustrates the spatial velocity differences with a finer resolution:

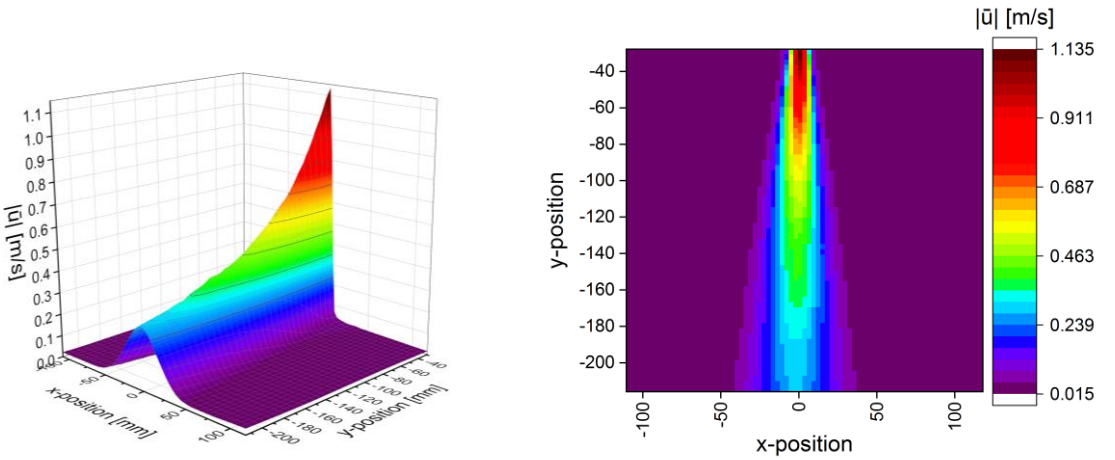

Figure 6-16: Scalar plot of averaged absolute velocity field

The three-dimensional visualization highlights the high velocity close to the free surface. According to the presented theory in chapter 2.7, the velocity decreases with descending y-position. Due to shear stresses, the initially thin jet entrains water from the initially quiescent ambient fluid. The jet accelerates an increasing mass of water the further it impinges into the pool. Consequently, according to the conservation of momentum, the magnitude of the velocity profiles decreases in flow direction.

The following figures show the averaged velocities in x- and y-direction:

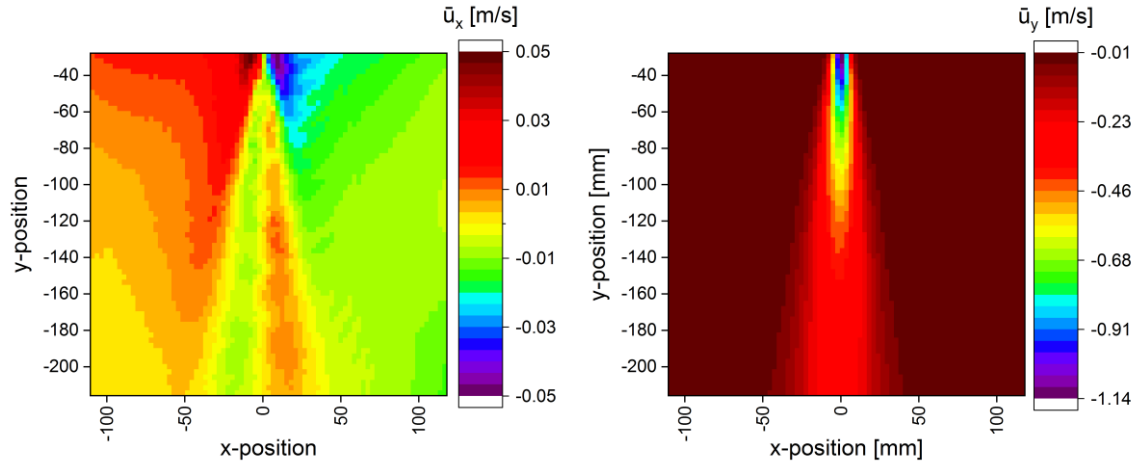

Figure 6-17: Left: Averaged velocity field in x-direction. Right: Averaged velocity field in y-direction

On the symmetry axis, $\bar{u}_x$ vanishes in the whole field of view, the jet has only an axial velocity component. Besides the axis, $\bar{u}_x$ increases, the fluid moves away from the centre of the jet. This movement leads to the widening of the jet, which causes its typical cone shape that is described in chapter 2.7. At a certain radial position, the direction of the movement inverts. The shift of the motion away from the axis of symmetry to the motion towards the axis represents the boundary between the jet and the recirculation area. The ratio to the maximum magnitude of $\bar{u}_x$ to $\bar{u}_y$ is approximately $3{,}7\ \%$. Hence, in regions of high velocities, the horizontal velocity component of the flow field is almost negligible compared to the vertical component.

Looking at the right illustration of Figure 6-17, the cone shape is clearly identifiable. The angle of the definite, linear contour can be estimated by calculating the inverse tangent of the ratio of the opposite leg to the adjacent leg. Doing so yields a value of $11{,}59°$ for the cone on angle left-hand side, and a value of $10{,}63°$ for that on the right hand-side of the two-dimensional figure. Hence, a slight asymmetry exists, and both angles are smaller than the value that is provided by literature ($11{,}8°$, see chapter 2.7). The reason for the deviation from the theoretical value is the recirculation zone. While the literature assumes an ambient fluid that is quiescent, the liquid flow adjacent to the jet has a velocity and the same orientation as the jet. This is a result of the finite size of the receiving pool, running-in time and the long measurement time. However, this movement of the ambient fluid leads to a diminishing relative velocity between the jet and the ambient water, and hence to decreasing shear stresses. The result of the lower shear stresses at the boundary of the jet is a smaller opening angle of the typical cone shape.

rms-values $u_{x,rms}$, $u_{y,rms}$ and $|\boldsymbol{u}|_{rms}$

The *rms*-values of the absolute velocity are presented in figure Figure 6-18:

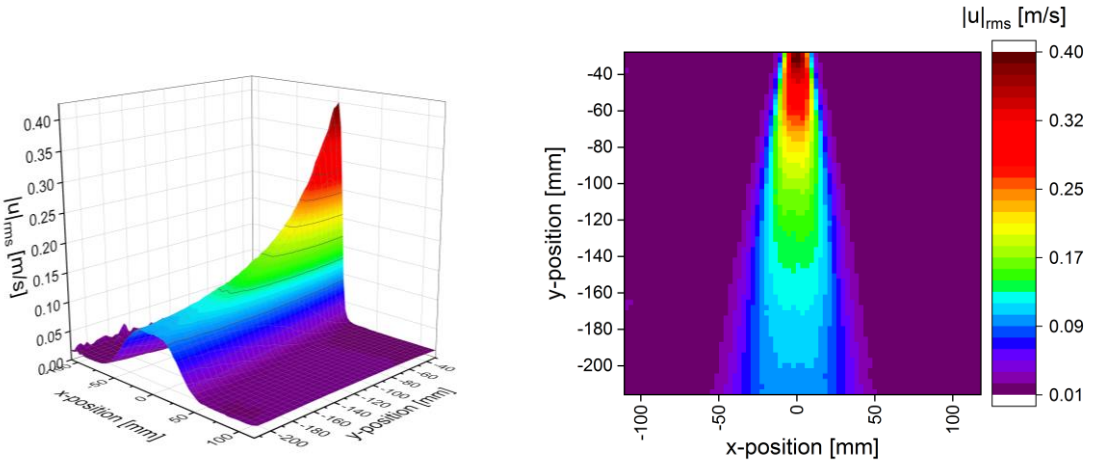

Figure 6-18: Scalar plot of rms-values of absolute velocity fluctuations

Close to the free surface and on the symmetry axis, the ratio of $|\boldsymbol{u}|_{rms}$ to the averaged absolute velocity and therefore the turbulence level of the flow is in the order of $35\,\%$. Equivalent to the characteristics of $|\overline{\boldsymbol{u}}|$, the magnitude of the fluctuations decreases with increasing distance to the impingement point of the jet at the free surface increases. At the same time, the area of velocity fluctuations expands in radial direction. Outside the conical shape of the jet, the velocity fluctuations as well as the mean velocity are uniformly close to zero.

Figure 6-19 shows the turbulence level on the symmetry axis of the jet:

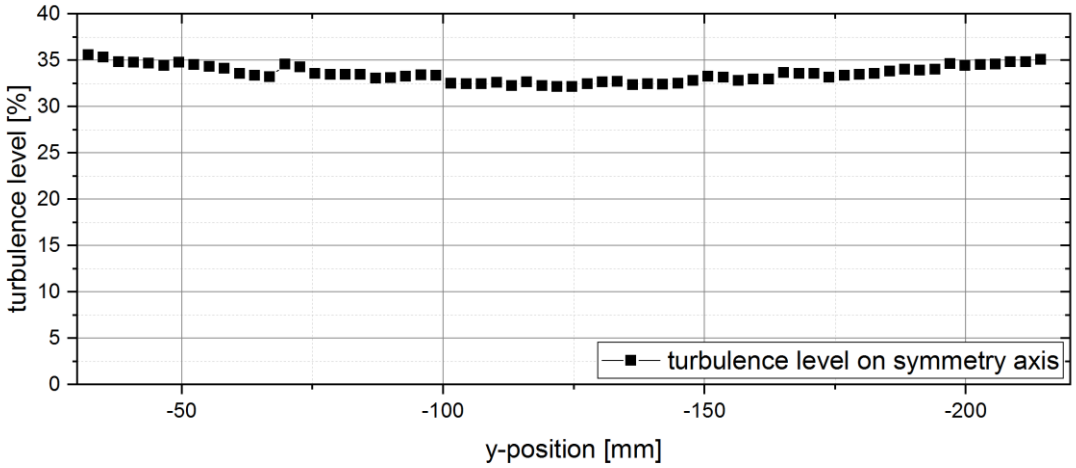

Figure 6-19: Turbulence level on symmetry axis of jet

The turbulence level on the symmetry axis of the jet is quite constant, it ranges from a maximum value of $35{,}6\ \%$ close to the free surface ($y = -32\ mm$) to a minimum value of $32{,}1\ \%$ ($y = -125\ mm$). Approaching the bottom of the receiving pool, the turbulence increases again to a magnitude of $35{,}1\ \%$ ($y = -214\ mm$).

Looking at the particular components $|\boldsymbol{u}|_{rms}$ consists of (Figure 6-20), the maximum magnitude of $u_{x,rms}$ is quite interesting:

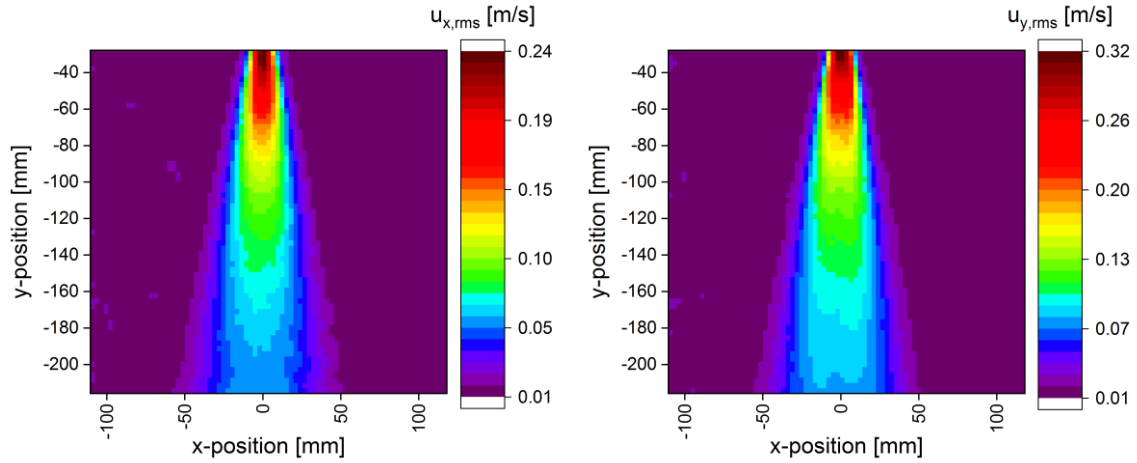

Figure 6-20: Left: rms-values of velocity field in x-direction. Right: rms-values of velocity field in y-direction

Although the mean velocity in x-direction does not exceed $0{,}0495\ m/s$, the maximum *rms*-value of the fluctuations in the same direction is approximately $0{,}24\ m/s$, which is a ratio of almost $500\ \%$. These high velocity fluctuations are found close to the free surface. A reasonable explanation for these high fluctuations combined with a low mean velocity of the flow is the air entrainment mechanism explained in chapter 2.9. At the impingement point of the jet, an inverse meniscus develops that oscillates. These oscillations can lead to fluid velocities in x-direction. The mean velocity in x direction vanishes if the amplitudes of the oscillations are identical in negative and positive x-direction.
The *rms*-values of the velocity fluctuations in y-direction show characteristics that are very similar to those in x-direction. The highest magnitude is found on the jet axis and close to

the surface. The fluctuations are diminishing both in axial and radial direction. Outside of the characteristic cone-shape, values in the range of $0{,}007$ to $0{,}03\ m/s$ are present. Although the distributions of $u_{x,rms}$ and $u_{y,rms}$ look very similar, the magnitudes are higher in y-direction. Hence, the present turbulence is anisotropic.

With these measurements of mean velocities and the corresponding *rms*-values of velocity fluctuations, numerous parameters that describe the turbulent flow field (e.g. Reynolds-stresses and turbulent kinetic energy) can be derived. As they are arithmetic combinations of the presented measurement quantities, they are shown in Appendix C.

6.3.2 Gaseous phase

The field of investigation is divided into four areas of different y-positions, as described in chapter 5.3.2. Each area has a width of $5\ mm.$ Figure 6-21 shows the trend of the vertical velocity component v_y of the bubbles that are detected:

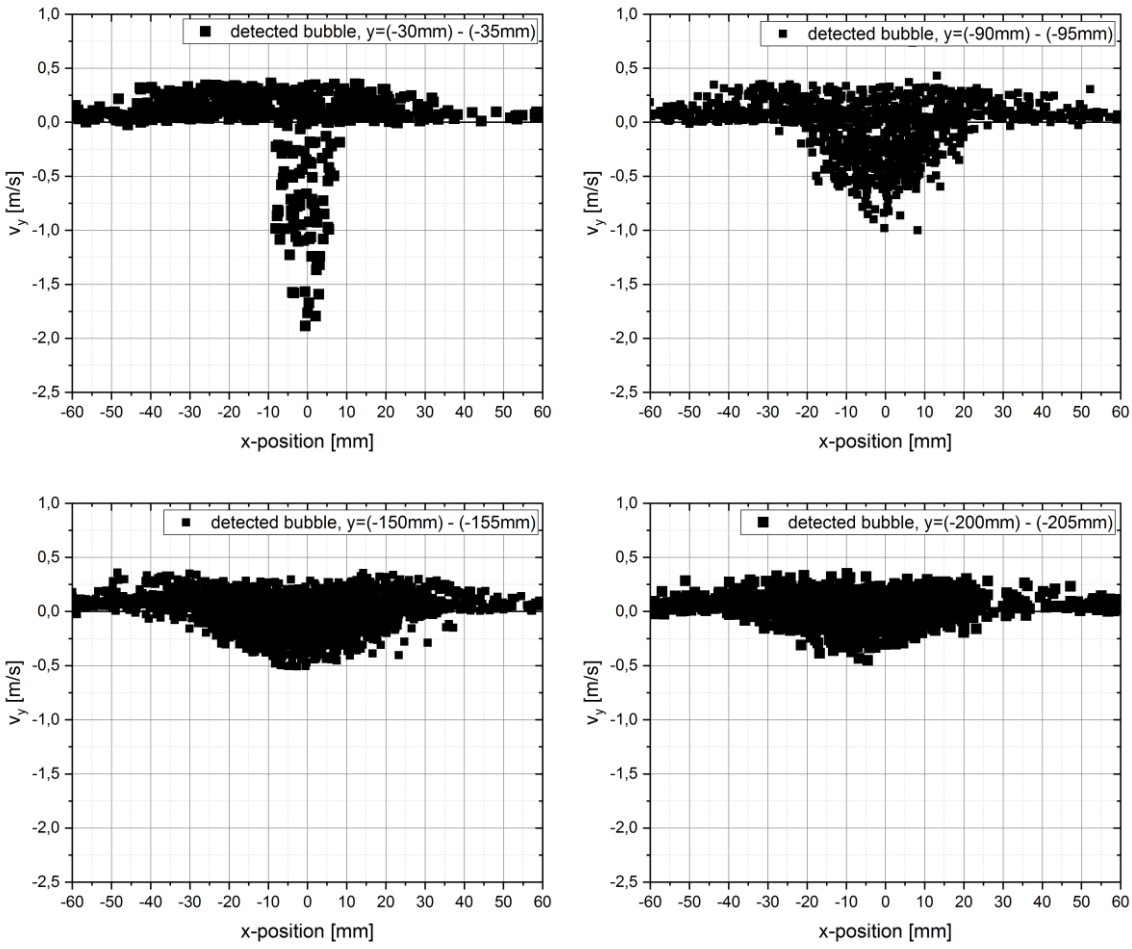

Figure 6-21: Vertical bubble velocity in dependency of x- and y-position

The first diagram presents the bubbles that are detected close to the free surface. The bubbles that perform a motion that accords with the flow direction of the plunging jet are concentrated on an area that ranges from $x = -10\ mm$ to $x = 10\ mm$. The maximum magnitude of the vertical velocity is marginally lower than $2\ m/s$, the fastest bubbles are located directly on the symmetry axis of the jet. These high velocities seem paradox, keeping in

mind that the maximum vertical velocity magnitude of the averaged liquid flow field is in the order of $1{,}1\ m/s$ (see Figure 6-17). Having analysed the particular recording of the fastest bubbles and having compared it to the corresponding instantaneous PIV measurements revealed velocities of the liquid phase close to the surface that exceed magnitudes of $2{,}4\ m/s$. Hence, the mean velocity field of the continuous phase is only limited usable to predict maximum magnitudes of bubble velocities.

Beside this zone of $x = \pm 10\ mm$, only rising bubbles are observed. The maximum magnitude of v_y in positive y-direction is in the order of $0{,}4\ m/s$, the distribution over the horizontal position remains quite constant over a wide range. At a radial position of $45\ mm$, the maximum velocity decreases to approximately $0{,}25\ m/s$.

The second vertical position ($y = (-90\ mm)$ to $(-95\ mm)$) exhibits smaller bubble velocities. The magnitudes of the rising bubbles remain constant. The zone of downward transported bubbles is expanding in radial direction, the rough x-coordinates beyond which no descending bubbles are observed are $\pm 30\ mm$. Furthermore, the magnitude of v_y decreases to half the value of the previously analysed position.

The maximum velocities recorded in the third investigated vertical position again show a reduction of 50%, the maximum magnitude is approximately $0{,}5\ m/s$. The zone of descending bubbles scales up to a horizontal expansion of $45\ mm$ in radial direction. The velocity of rising bubbles shows a reduction on the symmetry axis. Adjacent to the axis, the maximum rising velocity remains in the order of $0{,}4\ m/s$.

The fourth investigated area that is close to the lower end of the field of view does not indicate an exact distinction between zones of rising bubbles and zones of descending bubbles. The maximum amplitude of downward transported bubbles is still marginally greater than that of rising bubbles. The fastest bubbles are found besides the symmetry axis of the jet.

Figure 6-22 presents the spatial boundary of rising and descending bubbles:

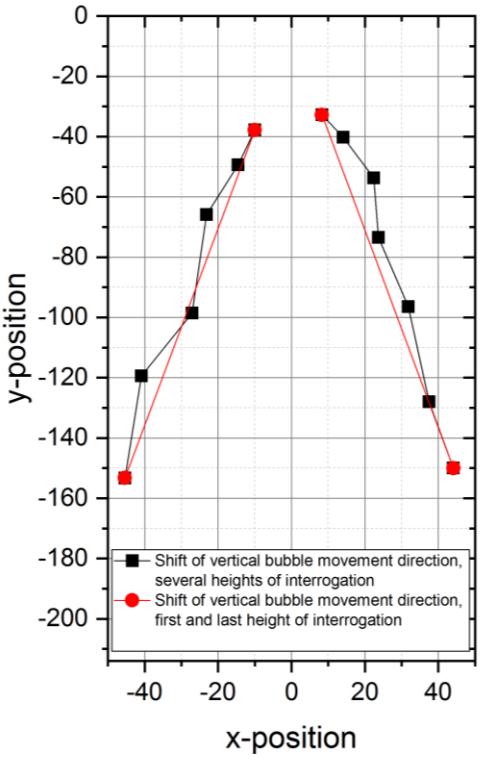

Figure 6-22: Spatial boundary of rising and descending bubbles

The diagram is based on the observations that are made in Figure 6-21, including the evaluation of further areas inside the field of view that are not listed in this chapter. As the dispersed air is not a continuous phase but appears randomly inside the receiving pool, the boundaries shown in Figure 6-22 are predicted on very sporadic data. The fact that no rising bubbles are detected outside the drawn boundaries does not imply unequivocally that it is not possible for bubbles to perform a movement in positive vertical direction; it is rather possible that no bubble is detected inside this area during the measurement period. Therefore, the boundaries that are given by Figure 6-22 are mere tendencies. However, describing these tendencies leads to the conclusion that the bubbles descend in a conical shape. Deriving a linear connection between the first and the last height of interrogation as shown Figure 6-22, an angle of $17°$ results for the straight line on the left-hand side and an angle of $16{,}9°$ on the right-hand side.

Figure 6-23 shows the diameter of the detected bubbles. The zones of evaluation are separated identically those in Figure 6-21.

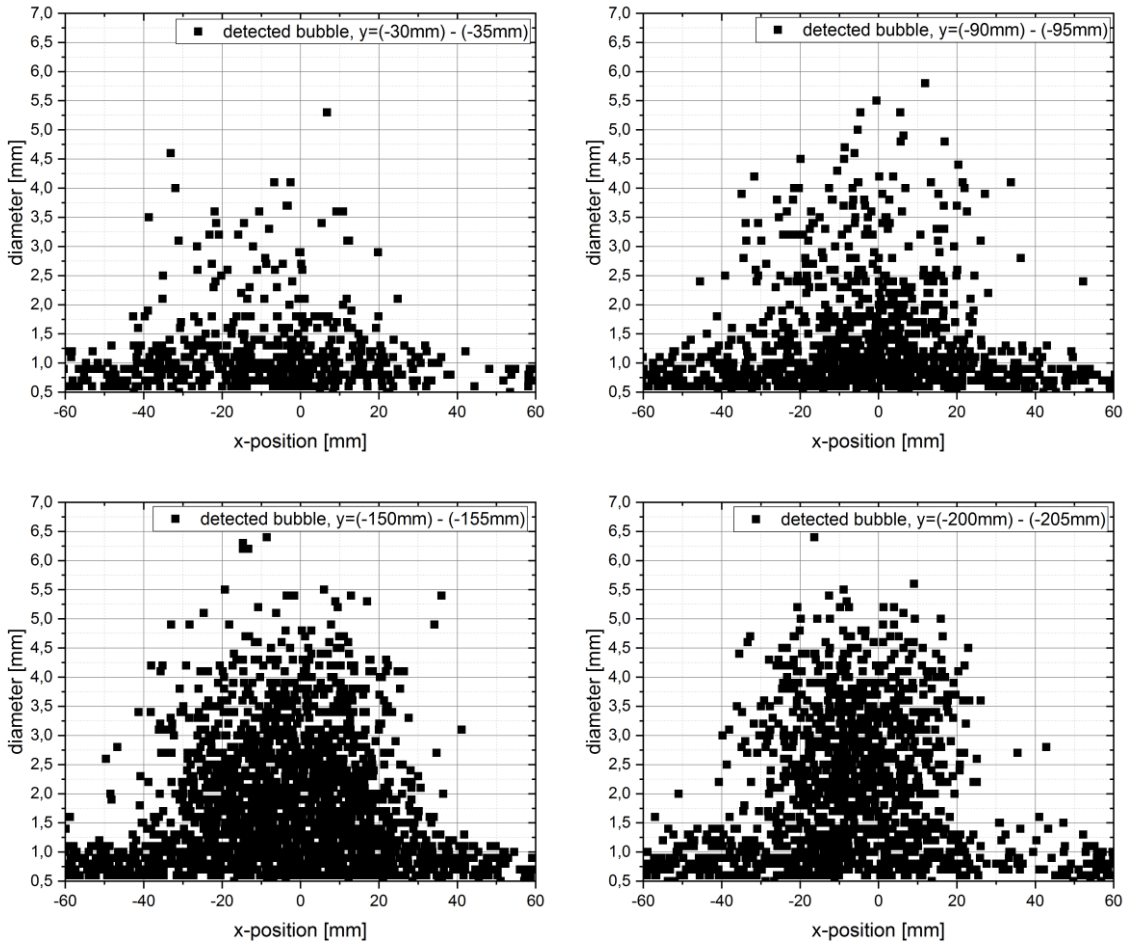

Figure 6-23: Bubble diameter in dependency of x- and y-position

Most of the bubbles are that detected close to the free surface of the receiving pool have a diameter that is smaller than $2\ mm$. Especially at the border of the field of view, no bubble greater than $1{,}5\ mm$ is detected that has a radial distance to the axis exceeding $42\ mm$. Furthermore, the distribution of bubbles exhibits an asymmetric character, since the right hand-side of the axis has a bubble density that is sparser.

The second vertical position ($y = (-90\,mm)$ to $(-95\,mm)$) shows more bubble counts than in the first position. The reason is the diminishing bubble velocity: The total number of bubbles does not increase (except the augmentation of bubbles due to their breakup), but some of them are detected several times as their hydraulic residence time is longer than the inverse of the recording frequency. However, the maximum size of the detected bubbles increases, which can be explained by the mechanism of bubble coalescence (see chapter 2.6). Both trends increase looking at the third position: The amount of detected bubbles increases further, as well as the maximum diameter, especially inside the in the zone drawn in Figure 6-22.
The last horizontal position that is investigated resembles the previous one inside a radial range of up to $30\,mm$ relative to the jet axis. The maximum diameter as well as the total amount of bubbles close to the jet axis seems very similar. Those that are located at a radial position that exceeds $40\,mm$ to the axis rise to the surface, as the buoyancy force is dominant since the vertical velocity of the surrounding water in negative y-direction is very low.
Figure 6-24 makes a connection between Figure 6-21 and Figure 6-23. Here, the vertical velocity component is shown on the y-axis, the bubble diameter is represent by the size of the marks inside the diagram. Again, the coordinates of the four evaluated areas are the same.

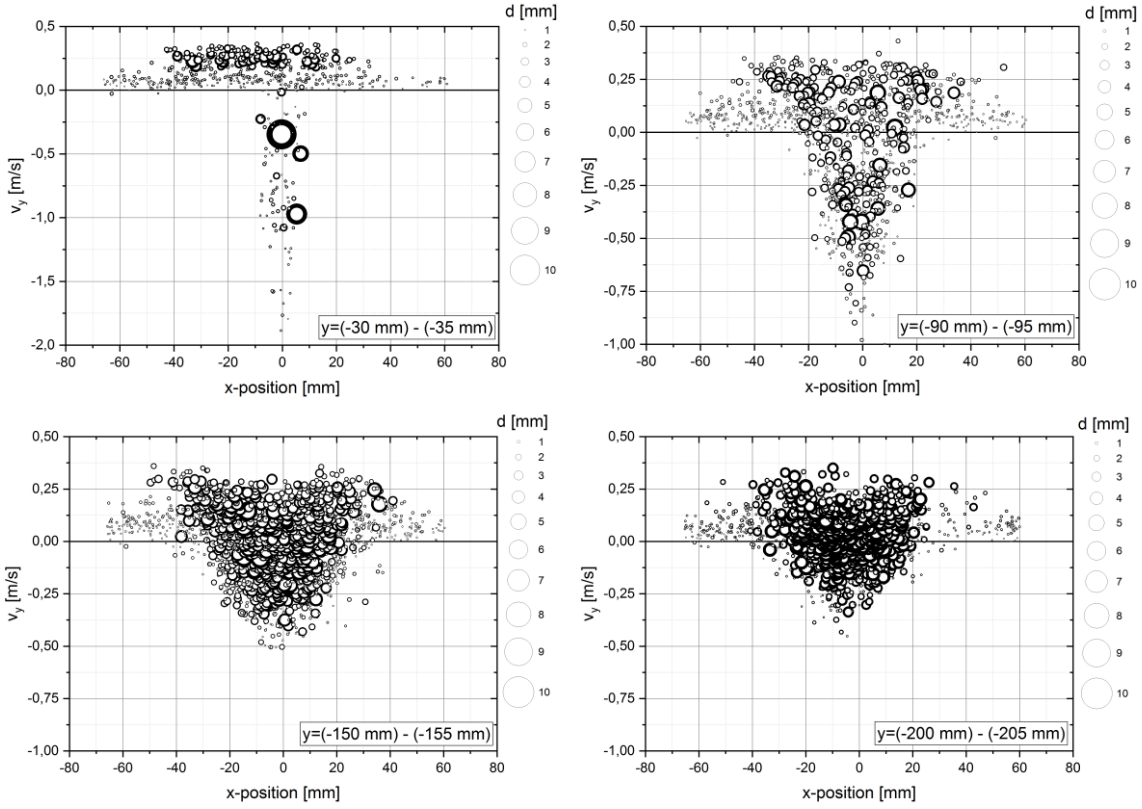

Figure 6-24: Bubble diameter and vertical velocity in dependency of x- and y-position

The first position reveals the different rising velocities of small and larger bubbles. Two distinct areas are seen. Small bubbles have a maximum rise velocity of approximately $0{,}25\,m/s$, whereas larger ones reach up to $0{,}4\,m/s$. The small bubbles are distributed over a wide range, the larger ones are concentrated within a radial range of $45\,mm$ away from

the axis. This explains the decrease of the rising velocity that can be observed in Figure 6-21 approaching the border of the field of view.
The further downstream the field is observed, more bubbles are counted. The graphic proves that the reason is not bubble-breakup, but the fact that some bubbles are detected several times due to their long hydraulic residence time. Observing the three other horizontal positions, it is evident that the slower the large bubbles, the more often they are recorded. The result is a dense plume of bubble detections around the symmetry axis, which leads to the conclusion that these large bubbles perform oscillating motions in y-direction and remain under water for a long time. Depending on the instantaneous vertical velocity component of the jet, which turned out to be highly intermitting (see chapter 6.3.1), the dominating force that determines the direction of the bubble's motion is either buoyancy that gives rise to the bubbles or the momentum of the jet that transports the bubbles downstream. Contrarily, small bubbles that are located at high radial distances to the axis are not affected. They rise with a constant velocity straight to the surface.

7 Summary

Subject of the present work is the experimental investigation of air entrainment by a plunging liquid jet. For this purpose, a construction was installed that generates a water jet which impinges on a receiving pool of the same liquid. The aim was to characterize the appearing phenomena and to provide quantitative data about the liquid flow field inside the pool, as well as about the gaseous flow that is existent in the form of dispersed air bubbles. The applied measurement techniques were Particle Image Velocimetry (PIV) to analyse the continuous liquid phase and shadowgraph imaging to observe the dispersed air bubbles. In addition, all the relevant boundary conditions that have an influence on the experiment were recorded. Thereby, a set of data was obtained that poses a basis for model validation of CFD-Codes.

The investigation area was located inside the receiving pool, which is a transparent, square container filled with fully demineralised water. The liquid jet was generated by a nozzle and fed by a feed tank that was installed above the receiving pool. The receiving pool as well as the feed tank were equipped with a spillover that enabled the possibility to maintain a constant water level in both boxes. This led to a constant jet length of $197\ mm$ and to a constant hydrostatic pressure inside the feed tank, and hence to a constant volume flow.

For the two-dimensional PIV recordings, a double-pulsed Nd:YAG laser was used to illuminate the investigation area. The camera was equipped with an optical filter to avoid parasitic optical signals to be recorded. Thus, only light that was emitted by the fluorescent tracer particles was captured by the camera. The light source that was applied for the shadowgraph imaging setup was a LED-matrix. The camera was equipped with an optical filter as well in order to block the light that was not emitted by the blue LED-matrix.
The measurements of PIV and shadowgraph imaging were synchronized, regarding their field of view as well as their recording timing. For that reason, both systems operated with the same frequency of recording and the same time interval between a double frame. Since the two techniques are different concerning the objects the cameras observe and the algorithm that evaluates the pictures, an accordant adjustment had to be found with which both systems are able to operate. Measurement results show that this time interval was too long to yield reliable PIV results in areas of high velocities and high turbulence. Therefore, the experiment was conducted a second time with identical boundary conditions and with a shorter time interval to ensure the correct mode of operation. At the same time, the second execution of the experiment served as a comparative measurement to ensure reproducibility. The comparison between the two data sets shows a good congruence in areas of low velocities. The defective PIV results were replaced by those of the comparative measurement.

A qualitative observation of the temporal flow behaviour by means of a time-lapse video and high-speed imaging was done. The time-lapse video reveals a highly fluctuating maximum penetration depth of the entrained air bubbles into the pool. Furthermore, the formation of the bubbles varies randomly from a dense bubble plume close to the surface to a small amount of air that is dispersed in the whole bath. Based on these observations, the estimation was made that a measurement time of approximately 60 minutes is necessary to form an average flow field that reflects the intermitting behaviour of the system.

The high-speed imaging indicated the jet surface instabilities close to the impingement point and the present mechanisms that lead to air entrainment into the water.

To analyse the temporal flow behaviour, both the PIV and shadowgraph recordings were divided into 18 sequences. Each sequence consists of 200 averaged instantaneous recordings of the flow field. For the PIV-measurements, the absolute velocity of the flow was observed; for the shadowgraph images, the amount of detected bubbles was counted. To ensure statistical significance, a moving average as well as the standard deviation over the particular sequences was formed. In this manner, the trend of the moving average and of the standard deviation was analysed. It was found that both trends are converging, for both the PIV measurements and the shadowgraph images. From sequence 17 to sequence 18, the relative change of the moving average was smaller than $0{,}5\ \%$. Thus, an averaged flow field that is formed of 3600 recordings of the instantaneous flow field is judged to be statistical significant. Since the frequency of the recording was set to $1\ Hz$, the absolute measurement time was 60 minutes. The comparison of the actual measurement and the comparative measurement exhibits an amount of detected bubbles that deviates by a factor in the order of 6. Hence, a guarantee for the reproducibility of the total amount of dispersed air bubbles is not given by repeating the experiment under identical conditions. However, the accumulated frequency of the bubble diameter shows a coinciding tendency for both experiments.

The spatial investigation of the averaged liquid flow field concerned the mean velocities and the Root-Mean-Square (*rms*) values of the velocity fluctuations. It was found that the mean velocities as well as the fluctuations show a symmetry around the jet axis with radially decreasing values. The turbulence intensity on the axis remains approximately constant, independent of the axial position of the jet. The opening angle of the jet inside the water pool is slightly smaller than literature allocates, which is explainable by the recirculation area that develops inside the pool. The liquid adjacent to the jet is not quiescent but in motion, which leads to diminishing relative velocities and hence to decreasing shear stresses at the boundary of the jet.

The spatial investigation of the dispersed air bubbles shows an area around the jet besides which no descending bubble is seen, only rising bubbles. The rising bubbles have different rising velocities, they are capable of being differentiated between small bubbles that have a rising velocity of approximately $0{,}25\ m/s$, and bigger ones that rise with $0{,}4\ m/s$. The fastest descending bubbles are located on the jet axis. The fastest bubble is about twice as fast as the maximum magnitude of the mean jet velocity, which is explainable by the high turbulence of liquid flow field. Although the maximum magnitude of the averaged flow field is in the order of $1{,}1\ m/s$, instantaneous PIV measurements reveal velocities of the liquid phase that exceed magnitudes of $2{,}4\ m/s$. Hence, the mean velocity field of the continuous phase is only limited usable to predict maximum magnitudes of bubble velocities.

8 References

[1] Adrian, R. J. 1986. Multi-point optical measurements of simultaneous vectors in unsteady flow—a review. *International Journal of Heat and Fluid Flow* 7, 2, 127–145.

[2] Amira, B. B., Driss, Z., and Salah Abid, M. 2015. PIV Study of the Interrogation Area Size Effect on the Hydrodynamic Results of a Stirred Vessel Equipped by an Eight Flat Blades Turbine. *International Journal of Fluid Mechanics & Thermal Sciences*, 42–48.

[3] Bińi, A. K. 1993. Gas entrainment by plunging liquid jets. *Chemical Engineering Science* 48, 21, 3585–3630.

[4] Boiko, V. M., Pivovarov, A. A., and Poplavski, S. V. 2013. Measurement of gas velocity in a high-gradient flow, based on velocity of tracer particles. *Combust Explos Shock Waves* 49, 5, 548–554.

[5] Bonhoeffer, B., Kwade, A., and Juhnke, M. 2017. Impact of Formulation Properties and Process Parameters on the Dispensing and Depositioning of Drug Nanosuspensions Using Micro-Valve Technology. *Journal of pharmaceutical sciences* 106, 4, 1102–1110.

[6] Böswirth, L. and Bschorer, S. 2007. *Technische Strömungslehre*. Vieweg+Teubner, Wiesbaden.

[7] Corrsin, S. 1961. Turbulent Flow. *American Scientist* Vol. 49, 3, 300–325.

[8] Crowe, C. T. 2012. *Multiphase flows with droplets and particles*. CRC Press, Boca Raton.

[9] Crowe, C. T., Gore, R. A., and Troutt, T. R. 1985. Particle Dispersion by coherent structures in free shear flows. Particle Dispersion by coherent structures in free shear flows. *Particulate Science and Technology* 3, 3-4, 149–158.

[10] Cushman-Roisin, B. *Environmental Transport and Fate*. *Turbulent Jets*, Dartmouth.

[11] Dadi, M., Stanislas, M., Rodriguez, O., and Dyment, A. 1991. A study by holographic velocimetry of the behaviour of free small particles in a flow. *Experiments in Fluids,* 10.

[12] Davidson, P. A. 2015. *Turbulence*. *An introduction for scientists and engineers*. Oxford Univ. Press, Oxford.

[13] Davies, R. M. and Taylor, G. 1950. The Mechanics of Large Bubbles Rising through Extended Liquids and through Liquids in Tubes. *Proceedings of the Royal Society A: Mathematical, Physical and Engineering Sciences* 200, 1062, 375–390.

[14] Dietrich, W. E. 1982. Settling velocity of natural particles. *Water Resour. Res.* 18, 6, 1615–1626.

[15] Fessler, J. R., Kulick, J. D., and Eaton, J. K. 1994. Preferential concentration of heavy particles in a turbulent channel flow. *Physics of Fluids* 6, 11, 3742–3749.

[16] Gladstone, J. H. and Dale, T. P. 1863. Researches on the refraction, dispersion, and sensitiveness of liquids. *Philosophical Transactions of the Royal Society of London* 153, 317–343.

[17] Hadad, T. and Gurka, R. 2013. Effects of particle size, concentration and surface coating on turbulent flow properties obtained using PIV/PTV. *Experimental Thermal and Fluid Science* 45, 203–212.

[18] Haynes, W. M. 2016. *CRC Handbook of Chemistry and Physics, 93rd Edition*. 100 Key Points. CRC Press, London.

[19] Hinds, W. C. 2012. *Aerosol Technology*. *Properties, Behavior, and Measurement of Airborne Particles*. Wiley-Interscience, s.l.

[20] Iguchi, M., Okita, K., and Yamamoto, F. 1998. Mean velocity and turbulence characteristics of water flow in the bubble dispersion region induced by plunging water jet. *International Journal of Multiphase Flow* 24, 4, 523–537.
[21] Keane, R. D. and Adrian, R. J. 1992. Theory of cross-correlation analysis of PIV images. *Applied Scientific Research* 49, 3, 191–215.
[22] Kell, G. S. 1975. Density, thermal expansivity, and compressibility of liquid water from 0 °C to 150 °C. . Correlations and Tables for Atmospheric Pressure and Saturation Reviewed and Expressed on 1968 Temperature Scale. *J. Chem. Eng. Data* 20, 1, 97–105.
[23] Kestin, J., Sokolov, M., and Wakeham, W. A. 1978. Viscosity of liquid water in the range −8 °C to 150 °C. *Journal of Physical and Chemical Reference Data* 7, 3, 941–948.
[24] Kümmel, W. 2007. *Technische Strömungsmechanik*. *Theorie und Praxis*. B.G. Teubner Verlag / GWV Fachverlage GmbH Wiesbaden, Wiesbaden.
[25] Lautrup, B. 2011. *Physics of Continuous Matter, Second Edition*. *Exotic and Everyday Phenomena in the Macroscopic World*. CRC Press, Hoboken.
[26] Lin, S. P. and LIAN, Z. W. 1990. Mechanisms of the breakup of liquid jets. *AIAA Journal* 28, 1, 120–126.
[27] Lin, S. P. and Reitz, R. D. 1998. Drop and Spray Formation from a liquid Jet. *Annu. Rev. Fluid Mech.* 30, 1, 85–105.
[28] Lin, T. J. and Donnelly, H. G. 1966. Gas bubble entrainment by plunging laminar liquid jets. *AIChE J.* 12, 3, 563–571.
[29] Litwiller, D. 2005. *CMOS vs. CCD*. *Maturing Technologies, Maturing Markets*.
[30] McKeogh, E. J. and Ervine, D. A. 1981. Air entrainment rate and diffusion pattern of plunging liquid jets. *Chemical Engineering Science* 36, 7, 1161–1172.
[31] Melling, A. 1997. Tracer particles and seeding for particle image velocimetry. *Measurement Science and Technology* 8, 12, 1406–1416.
[32] Nieuwstadt, F. T.M., Westerweel, J., and Boersma, B. J. 2016. *Turbulence*. Springer International Publishing, Cham.
[33] Oertel, H., Böhle, M., and Reviol, T. 2015. *Strömungsmechanik*. Springer Fachmedien Wiesbaden, Wiesbaden.
[34] Panigrahi, P. K. and Muralidhar, K. 2012. Laser Schlieren and Shadowgraph. In *Schlieren and Shadowgraph Methods in Heat and Mass Transfer*, P. K. Panigrahi and K. Muralidhar, Eds. SpringerBriefs in Applied Sciences and Technology. Springer New York, New York, NY, 23–46. DOI=10.1007/978-1-4614-4535-7_2.
[35] Prandtl, L. 1904. Über Flüssigkeitsbewegung bei sehr kleiner Reibung. *Verhandlungen des dritten internationalen Mathematiker-Kongresses*, 484–491.
[36] Prince, M. J. and Blanch, H. W. 1990. Bubble coalescence and break-up in air-sparged bubble columns. *AIChE J.* 36, 10, 1485–1499.
[37] Qu, X. L., Khezzar, L., Danciu, D., Labois, M., and Lakehal, D. 2011. Characterization of plunging liquid jets. A combined experimental and numerical investigation. *International Journal of Multiphase Flow* 37, 7, 722–731.
[38] Raffel, M., Willert, C. E., and Kompenhans, J. 1998. *Particle image velocimetry*. *A practical guide ; with 24 tables*. Engineering online library. Springer, Berlin.
[39] Schlichting, H. and Gersten, K. 2017. *Boundary-Layer theory*. Springer Berlin Heidelberg, Berlin, Heidelberg.
[40] Soloff, S. M., Adrian, R. J., and Liu, Z.-C. 1997. Distortion compensation for generalized stereoscopic particle image velocimetry. *Meas. Sci. Technol.* 8, 12.

[41] Stokes, G. G. 1845. On the Theories of the Internal Friction of Fluids in Motion. *Transactions of the Cambridge Philosophical Society* 8.

[42] Tipler, P. A., Mosca, G., and Wagner, J. 2015. *Physik*. *Für Wissenschaftler und Ingenieure*. Springer Berlin Heidelberg, Berlin, Heidelberg.

[43] van de Sande, E. 1974. *Air entrainment by plunging water jets,* TU Delft.

[44] Vargaftik, N. B., Volkov, B. N., and Voljak, L. D. 1983. International Tables of the Surface Tension of Water. *Journal of Physical and Chemical Reference Data* 12, 3, 817–820.

[45] Weber, C. 1931. Zum Zerfall eines Flüssigkeitsstrahles. *Z. angew. Math. Mech.* 11, 2, 136–154.

[46] Yang, H. Q. 1992. Asymmetric instability of a liquid jet. *Physics of Fluids A: Fluid Dynamics* 4, 4, 681–689.

[47] Zidouni Kendil, F., Danciu, D. V., Schmidtke, M., Bousbia Salah, A., Lucas, D., Krepper, E., and Mataoui, A. 2012. Flow field assessment under a plunging liquid jet. *Progress in Nuclear Energy* 56, 100–110.

[48] Zierep, J. and Bühler, K. 2008. *Grundzüge der Strömungslehre*. Teubner, Wiesbaden.

Appendix A – Technical drawings

Feed tank

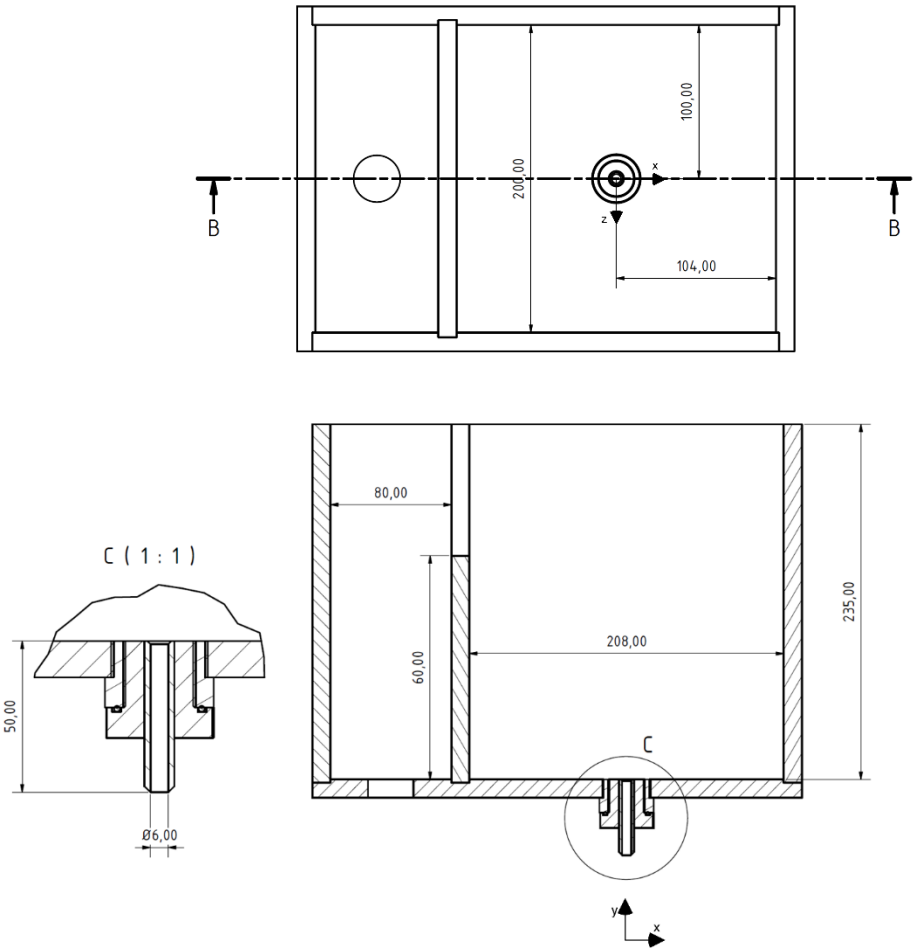

Receiving pool

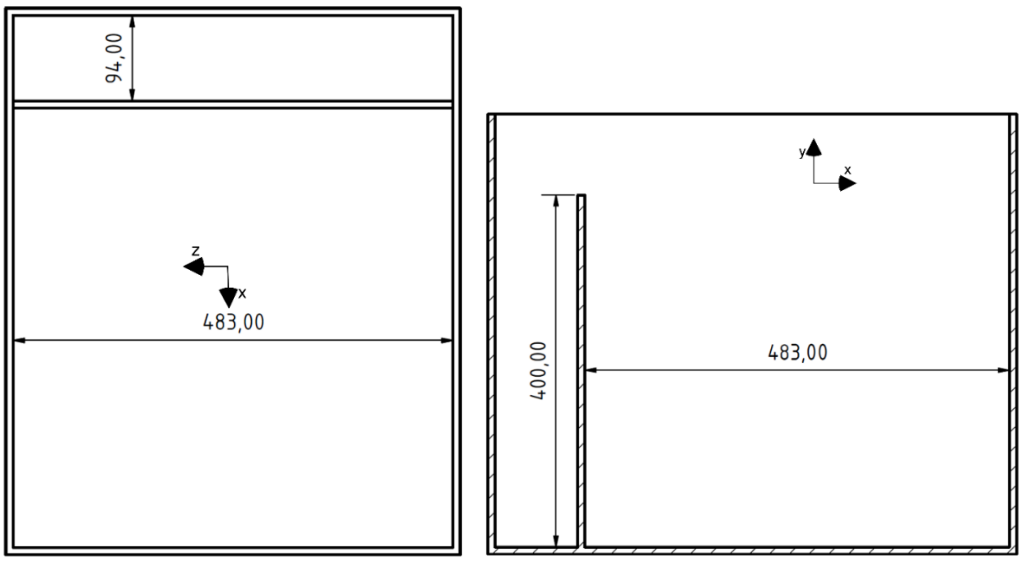

Appendix B – Tabular listing of measurement conditions

Parameter	***Value***	***Unit***
Length of liquid jet	197	mm
Diameter nozzle	6	mm
Length nozzle	50	mm
Running-in time of system	50	min
Measurement time	60	min
Recording frequency	1	$1/s$
Time interval dt between double frames	1000	μs
Range of temperature in receiving pool	22,0 – 24,1	$°C$
Range of density of water	997,295 – 997,2748	kg/m^3
Range of dynamic viscosity of water	$953{,}2 * 10^{-6}$ – $907{,}2 * 10^{-6}$	$Pa * s$
Range of surface tension	$72{,}44 * 10^{-3}$ – $72{,}11 * 10^{-3}$	N/m
Temperature of ambient air	21,9	$°C$
Pressure of ambient air	$1{,}007 * 10^{5}$	Pa
Volumetric flow rate of water	0,049804	l/s
Electrical conductivity of water	$1{,}76 * 10^{-4}$	S/m

Appendix C – Measurement results

Corresponding to chapter 6.2.2: Temporal behaviour of liquid flow

Interrogation area 1:

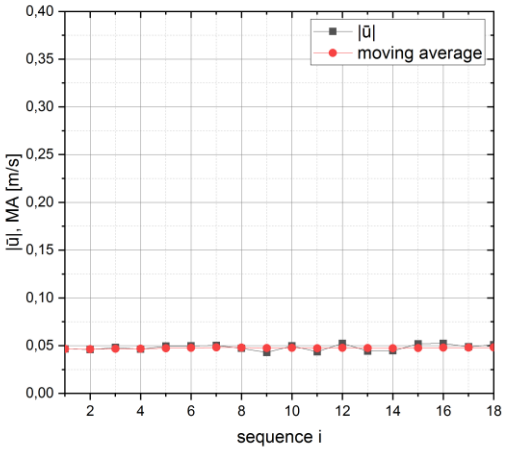

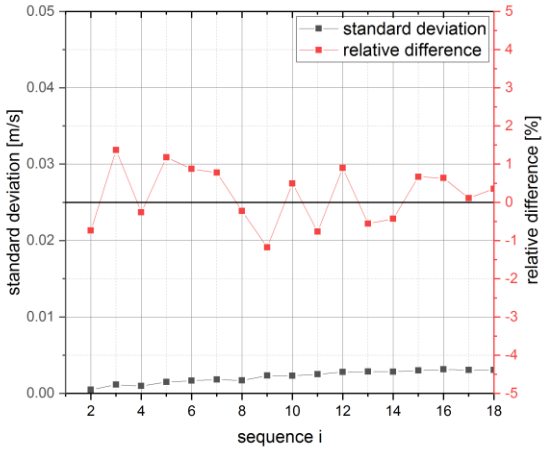

Interrogation area 2:

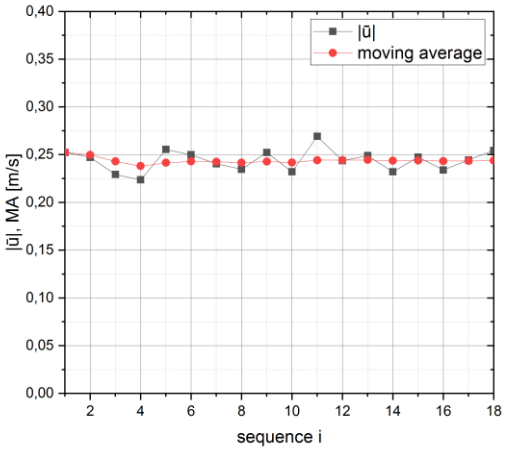

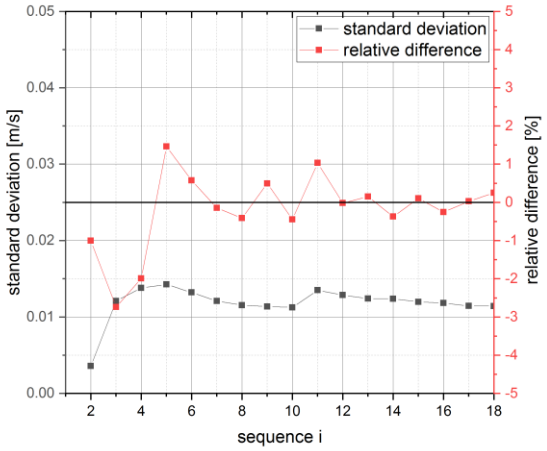

Interrogation area 3:

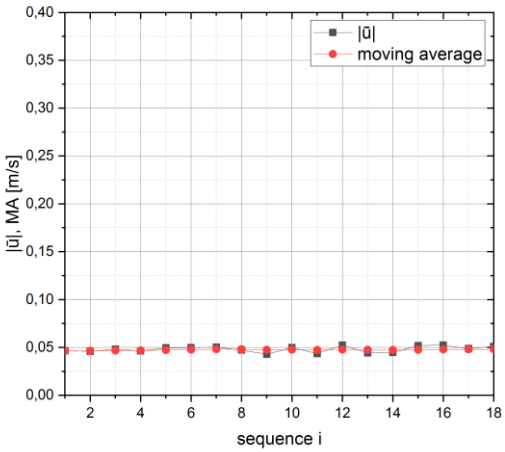

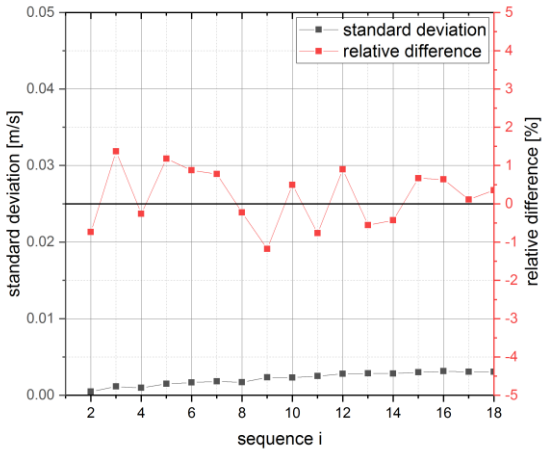

Interrogation area 4:

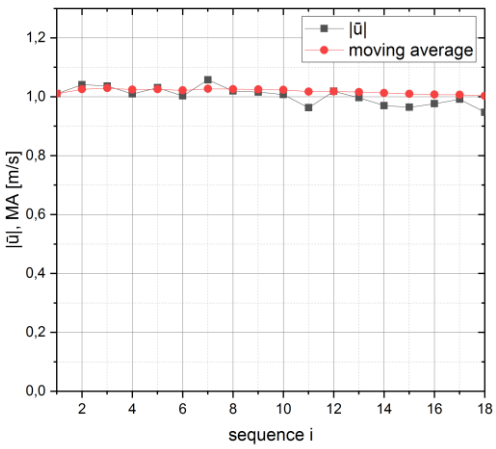

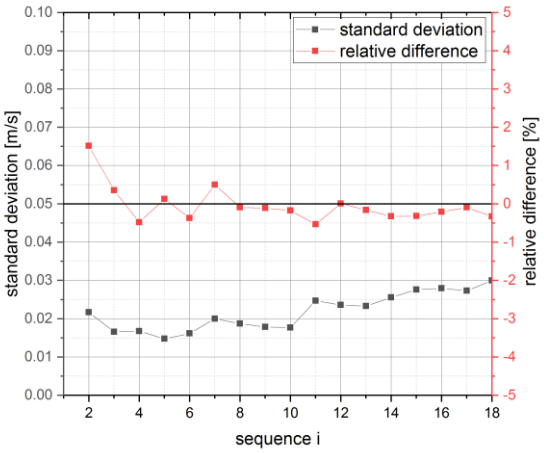

Interrogation area 5:

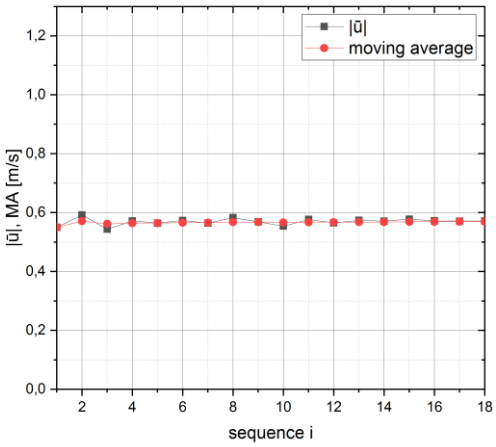

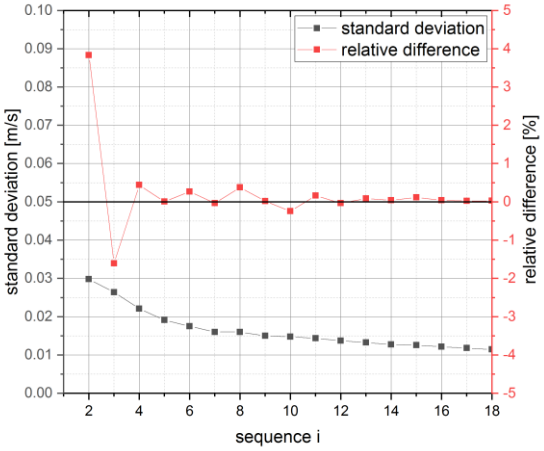

Interrogation area 6:

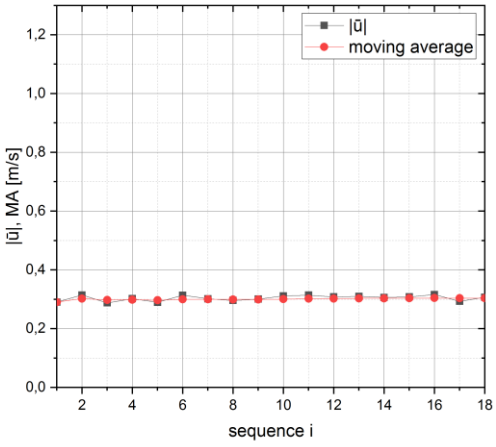

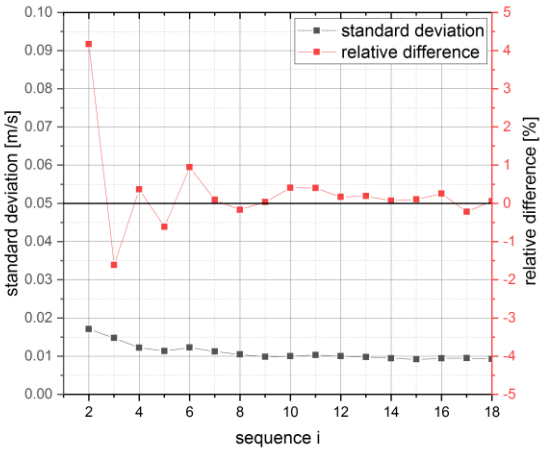

Corresponding to chapter 6.3.1: *Reynolds-stresses*

$\tau_{xx}{}^{R}$:

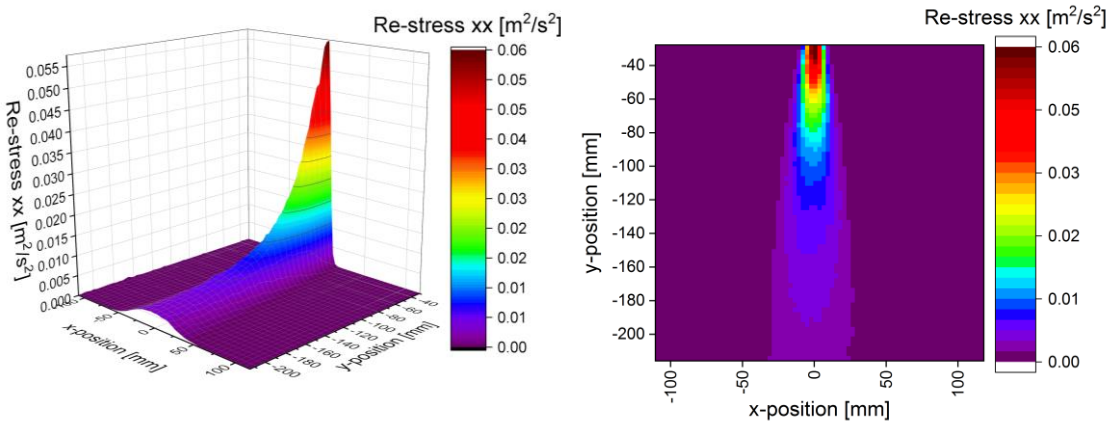

$\tau_{xy}{}^{R}$:

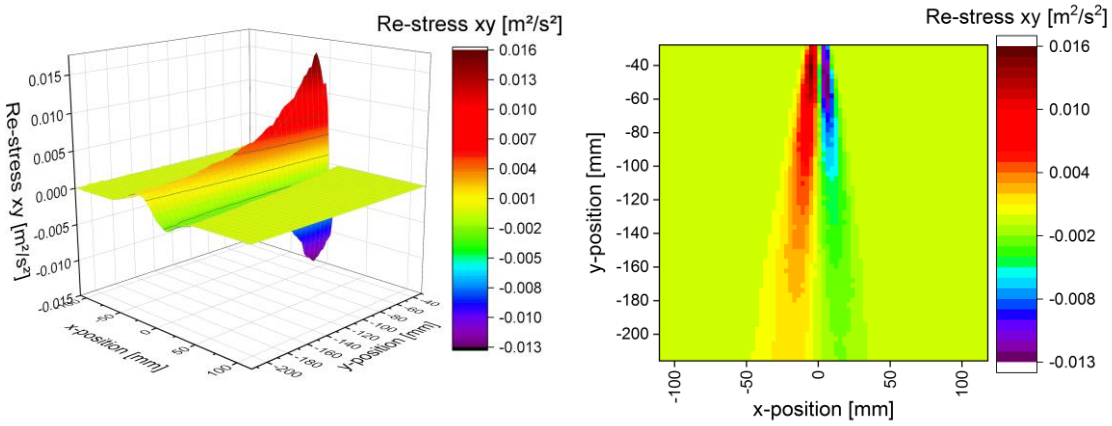

$\tau_{yy}{}^{R}$:

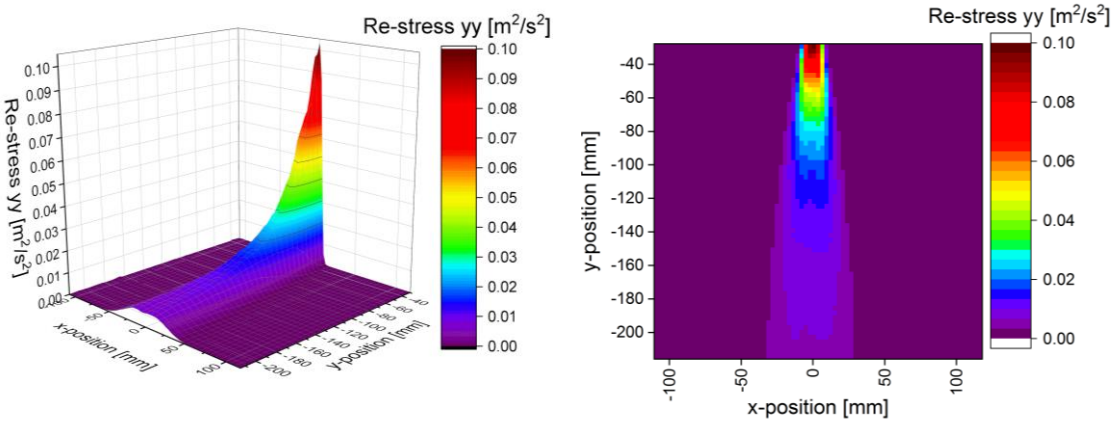

Corresponding to chapter 6.3.1: *Turbulent kinetic energy k*

As the investigation of the liquid flow is limited to two dimensions, the component in z-direction must be estimated. Since the jet exhibits a symmetry around its vertical axis, the *rms*-values of the fluctuations in z-direction are expected to equal those in x-direction. Accordingly, the turbulent kinetic energy is calculated using the following formula:

$$k = \frac{1}{2}(u_{y,rms}^2 + 2 * u_{x,rms}^2)$$